学位論文

Photoelectron coincidence spectroscopy of multi-photon double ionization of rare gas atoms by ultrashort high-order harmonics

(超短高次高調波による希ガス原子の

多光子二重イオン化過程の光電子コインシデンス分光)

平成 28 年 12 月博士（理学）申請

東京大学大学院理学系研究科

化学専攻

山田　佳奈

Contents

Chapter 3 Observation of Laser-Enabled Auger Decay Process by Coincidence Photoelectron Spectroscopy

Chapter 4 Development of Pump-Probe Experimental Setup for Observation of Ultrafast Phenomena with High-Temporal Resolution

Abstract

When atoms are irradiated with extreme ultra-violet light pulses, various types of ionization processes occur on the attosecond (1 as = 10^{-18} s) to femtosecond (1 fs = 10^{-15} s) timescales. In these ionization processes, electrons are emitted as a result of interactions with many electrons in the atom, and the investigation of these processes is important for the fundamental understanding of electron correlations and is also expected to give us valuable insights into the control of chemical reactions. In this thesis, (i) the population distribution of doubly charged atoms created through a two-photon double ionization process via an intermediate resonance was investigated by photoelectron coincidence spectroscopy using high-order harmonics, (ii) signals which might be assigned to the laser-enabled Auger decay (LEAD) process were observed in the pump-probe measurements using high-order harmonics and near-infrared (NIR) light pulses, and (iii) a new experimental setup for pump-probe measurements with high temporal resolution was designed and constructed.

In the first experimental study, coincidence photoelectron spectroscopy of Ar irradiated with high-order harmonics of NIR light pulses was performed. In this experiment, two-photon double ionization process via the $3s3p^6np$ ($n \sim 25$) intermediate resonances of Ar was observed, and this process showed a selective creation of Ar^{2+} in the $3s3p^5\ ^1P$ state. It has been known that the population distribution of Ar^{2+} deviates from the statistical weight when they are created through a one-photon threshold direct double ionization process or a three-photon sequential double ionization process. However, neither of these processes exclusively created the $3s3p^5\ ^1P$ state of Ar^{2+}. The observed selectivity indicates that the electron configuration of the intermediate resonance affects the electron configuration of the resultant doubly charged ion, and the simultaneously emitted two electrons tend to form the singlet state.

In the second experimental study, Ar was irradiated with high-order harmonics and NIR light pulses, and coincidence photoelectron spectroscopy was performed while changing the time delay of the NIR light pulses to the high-order harmonics. In the correlation map of the energies of the simultaneously emitted electrons, there were signals which appeared only when Ar was irradiated with the NIR light pulses after the high-order harmonics. Considering the energies of the signals, it is highly possible that the observed signals are from the LEAD process, in which the 23rd harmonic induces the 3*s* electron emission and the Auger decay process occurs with the assist of twelve NIR photons. The existence of the LEAD process has been suggested in 2011, but the signals purely assigned to the LEAD process has not been reported before.

In order to perform pump-probe measurements using high-order harmonics, which are generated

as attosecond pulse trains or single attosecond pulses, and NIR light pulses with high temporal resolution, a new experimental setup was designed and is now under construction. This setup will be used mainly for the observation of sub-femtosecond processes, which occur before the nuclear rearrangements, and the effects of the sub-femtosecond processes to the following chemical reactions will be investigated. The current performance of the setup was confirmed by using a flat-field type extreme ultra-violet spectrometer and a magnetic-bottle type photoelectron spectrometer.

Chapter 1

General Introduction

1.1. Introduction

Photoionization is a very fundamental process, which is followed by a variety of chemical reactions such as rearrangements of electron configuration and chemical bond breakings. During and after the photoionization process, the ejected electrons and the electrons remaining in the atoms and molecules interact with each other, and these electron correlations strongly affect the ionization process and the following chemical reactions. Investigation of the behaviors of these electrons helps us deepen the understanding of the photoionization process and its related processes, and also gives us important insights into the control of chemical reactions.

The investigations of ionization processes have been accelerated with the advent of intense light sources in the extreme ultraviolet region [1-3], which induces many kinds of ionization processes such as the emission of an electron from the inner shell. Free electron lasers are one of these light sources [3]. Because they can generate high energy photons in 10^3 electron-volt (keV) region, they are suitable for the investigation of core ionization processes. High-order harmonic [1,2] of ultrashort laser pulses is another one of those light sources, whose properties such as the intensity, the wavelength distribution, and the pulse duration can be changed at will by choosing a proper generation method. Because the high-order harmonics have the pulse durations of the attosecond (1 as = 10^{-18} second) to femtosecond (1 fs = 10^{-15} second) region, they are suitable for the investigation of the ultrafast electronic processes before and after the electron emission, which occur on these time scales [4,5].

In this thesis, photoionization processes of rare gas atoms induced by the irradiation of high-order harmonics were investigated by photoelectron coincidence spectroscopy. Although many experimental and theoretical studies have been carried out on the photoionization processes of rare gas atoms, such as double ionization processes [6,7], autoionization processes [8], and the Auger decay process [9], the effects of electronic behaviors in the processes are still not clarified. There are also processes whose existence is not experimentally confirmed yet [10,11]. In this thesis, we aimed at gaining insights into the effects of the interactions among the electrons in the ionization processes and also at observing processes which are still not explored in detail.

1.2. High-Order Harmonic Generation from Ultrashort Laser Pulses

High-order harmonics are generated through a non-linear optical effect induced by focusing intense laser pulses on a gaseous medium [2] or on a solid material [12]. The mechanism of the high-order harmonic generation was explained by a so-called three-step model [1,13] in 1993. The schematic of this model is shown in Fig. 1-1. According to this model, (i) the Coulomb potential of the atom is distorted by the applied electronic field, which allows an electron to be emitted to the continuum by a tunnel ionization, (ii) the electron in the continuum is accelerated away from and then back towards the parent ion by the oscillating laser field, and finally, (iii) the electron recombines with the parent ion emitting a photon having the energy E_{photon} written as

$$E_{\mathrm{photon}} = I_{\mathrm{p}} + E_{\mathrm{kin}}, \tag{1-1}$$

where I_{p} is the ionization potential of the atom and E_{kin} is the kinetic energy of the electron gained in the second step. Because I_{p} of the rare gas atoms increases as the atomic number decreases, the

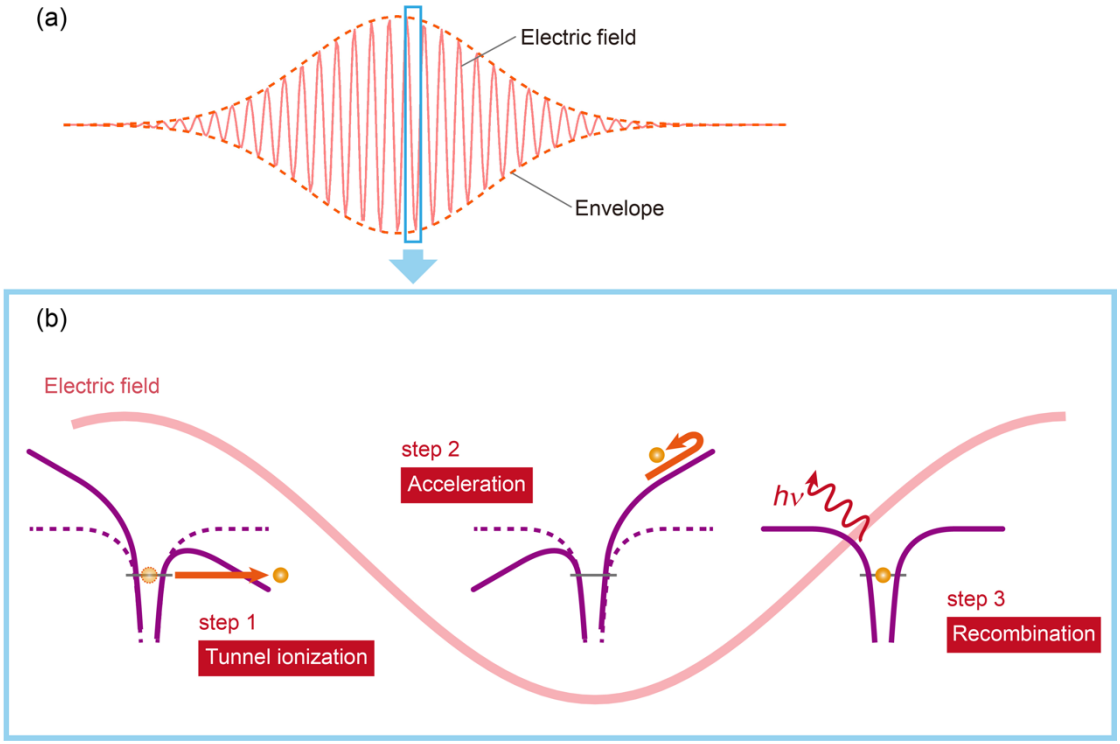

Figure 1-1 (a) Fundamental pulses used for the high-order harmonic generation and (b) the schematic of the high-order harmonics generation explained by the three-step mechanism. In the first step, the Coulomb potential (purple curve) is distorted by the strong laser field, and an electron (yellow sphere) is emitted by the tunnel ionization. In the second step, the emitted electron is accelerated away from and back towards the parent ion by the laser field. In the third step, the electron recombines with the parent ion, and a photon is emitted having the energy $h\nu = I_{\mathrm{p}} + E_{\mathrm{kin}}$, where I_{p} is the ionization potential of the atom and E_{kin} is the kinetic energy obtained during the second step. The emitted photons are called high-order harmonics.

harmonics generated from He have higher photon energies than the harmonics generated from Ar as shown in Fig. 1-2 [14].

The maximum value of E_{kin} is calculated to be $3.17U_p$ [1], where U_p is the ponderomotive energy. U_p is defined as U_p [eV] = $9.337 \times 10^{-5} \times I$ [PW/cm^2] $\times$ (λ [nm])^2, where I and λ are the laser intensity and the wavelength of the laser, respectively. This means that the maximum photon energy, or the cutoff energy of the generated harmonics $E_{photon,\ cutoff}$ is

$$E_{photon,\ cutoff}\ [\mathrm{eV}] = I_p\ [\mathrm{eV}] + 2.96 \times 10^{-4} \times I\ [\mathrm{PW/cm^2}] \times (\lambda\ [\mathrm{nm}])^2. \quad (1\text{-}2)$$

Eq. (1-2) suggests that the energy range of the generated harmonic photons varies when the intensity and the wavelength of the fundamental laser pulses are changed. Therefore, we can generate high-order harmonics in the intended energy region by choosing the appropriate gaseous medium, fundamental laser intensity, and fundamental laser wavelength.

The high-order harmonic generation technique has been developed dramatically in the last few decades and is still keeping on evolving. One direction of the development is the generation of the high-order harmonics with higher photon energies. Because the upper limit of the photon energy of the generated harmonics is written as Eq. (1-2), the high-order harmonics with higher photon energies are generated by increasing the intensity of the focused laser pulses. By using intense femtosecond

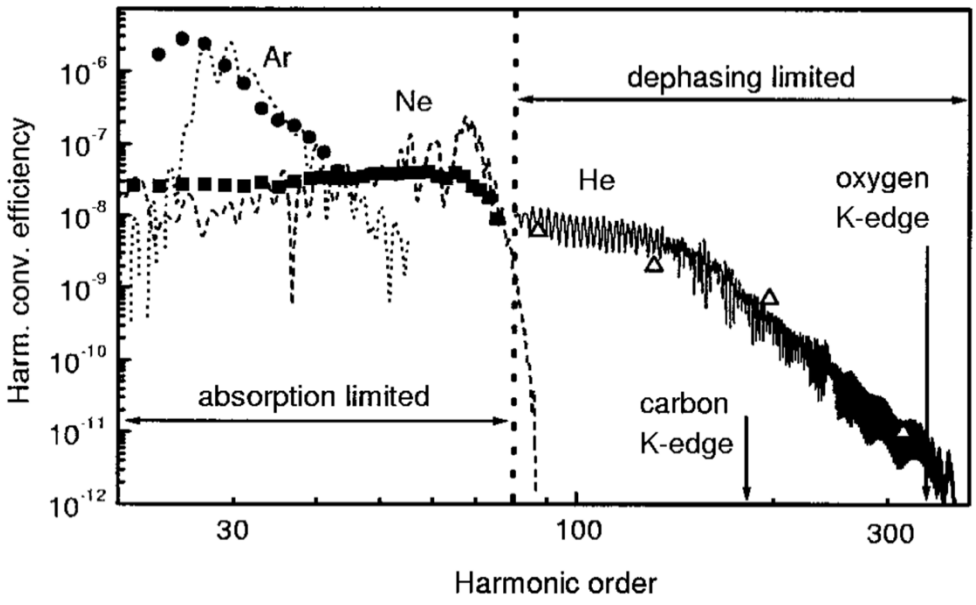

Figure 1-2 Conversion efficiency of high-order harmonics plotted as a function of harmonic order. Circles, squares, and triangles correspond to the measured conversion efficiency of harmonics from Ar, Ne, and He, respectively. Dotted curve, dashed curve, and solid curve correspond to the calculated conversion efficiency of harmonics from Ar, Ne, and He, respectively. The figure is adopted from ref. [14].

laser sources, high-order harmonics even in the water-window region can be generated these days [15,16]. The water-window region is defined as the energy range between the *K*-absorption edges of carbon (284 eV) and oxygen (543 eV), and they are absorbed by carbon while they are transparent to oxygen. This means that the harmonics in this region can be used for the imaging of the carbon density under the environment of water, therefore, they are ideal for the imaging of the inner structure of a living cell with a high contrast [17].

Another direction of the development is the generation of intense high-order harmonics [18-24]. Firstly, the conversion efficiency of the harmonics was improved to 10^{-5}~10^{-6} by achieving the phase matching condition in a long interaction region. This was realized by guiding the fundamental laser pulses through a gas-filled hollow core fiber [18-21] or a quasi-static gas cell [22,23]. Then, *Takahashi et al.* [24] proposed that the intensity of the harmonics can be further increased by using a loosely focusing configuration. With this configuration, the volume of the harmonic generation region is increased while meeting the phase matching condition, and they succeeded in generating harmonics as intense as 0.7 μJ. The generated harmonics are intense enough to induce even a non-linear process, such as the two-photon ionization of He [25].

1.3. Generation of High-Order Harmonics as Single Attosecond Pulses

High-order harmonics are generated every half-cycle of the laser field, and the harmonics are generated as pulse trains with the conventional generation methods introduced in section 1.2. In 2001, *Hentschel et al.* [26] restricted the number of harmonics generated from one fundamental laser pulse to only one, in other words, they generated high-order harmonics as single attosecond pulses instead of attosecond pulse trains. Since this first report, many methods to generate single attosecond pulses have been proposed [5,27-29] as summarized in Table 1-1. Most of these methods are classified into (i) amplitude gating method, (ii) polarization gating method, and (iii) ionization gating method.

In the conventional amplitude gating method [26,30-32], few femtosecond light pulses with a stabilized carrier-envelope phase (CEP), which is the offset of the peak of the electric field to the peak of the pulse envelope, are used as the fundamental pulses. In this way, the laser field has only few optical cycles, and the generation of the harmonics near the cut-off region is restricted to the central intense part of the laser field shown in Fig. 1-3(a). By extracting the harmonics in the cut-off region indicated in Fig. 1-3(b) using a multi-layered mirror or a filter, harmonics can be obtained as single

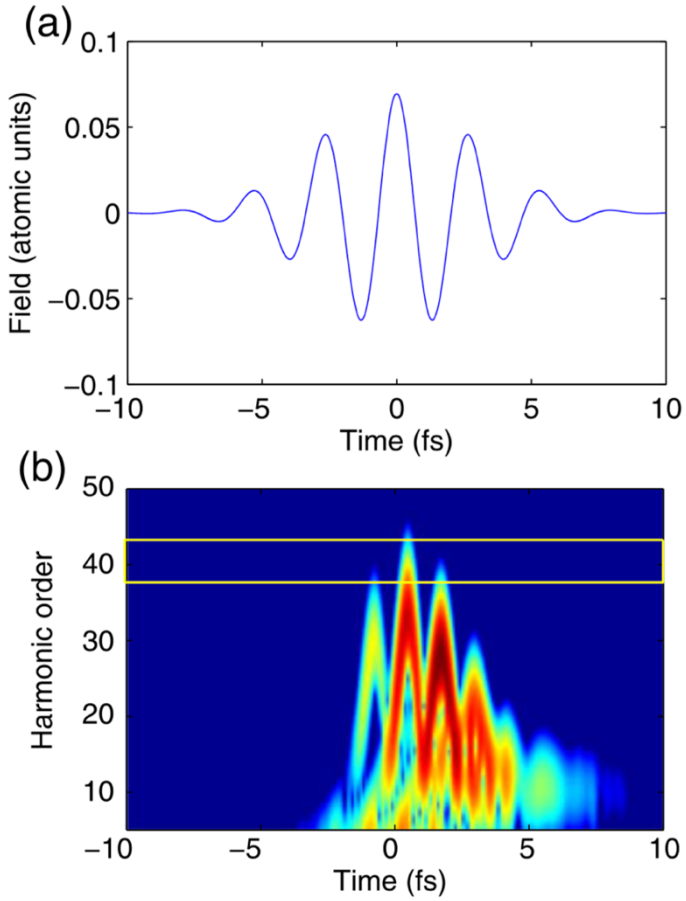

Figure 1-3 Harmonic generation as single attosecond pulses by the amplitude gating method. (a) Electric field of the fundamental light pulse with 5 fs pulse duration and (b) the spectrum of harmonics generated from the electric field shown in (a). By extracting the yellow square region in (b), single attosecond pulses are obtained. The figure is adopted from ref. [5].

attosecond pulses. With this method, single attosecond pulses with the pulse duration of as short as 80 attoseconds have been generated [32].

One of the difficult parts of using this method is that the fundamental pulses need to have the pulse duration of few femtoseconds. *Oishi et al.* [33] eased this restriction by using pulses synthesized with 400 and 800 nm light pulses. The square of the synthesized field has a maximum peak at the pulse center while the intensities of the nearest-neighbor peaks are suppressed, therefore, the generation of the harmonics in the cut-off region is restricted to the central part of the synthesized laser field, therefore, few-femtosecond pulses are no longer necessary. This method is called two-color gating method, and ~200 as pulses were generated from ~10 fs fundamental pulses. Later, *Takahashi et al.* [34] showed that high-order harmonics can be generated by a so-called IR two-color gating method, where 800 and 1300 nm pulses with ~30 fs pulse duration are used. With this long pulse duration, CEP is not important, and there is no need to stabilize CEP.

Table 1-1 Generation methods of single attosecond pulses.

Method	Fundamental pulse duration	CEP locking*	Shortest pulse duration among refs.	Refs.
Amplitude gating	~5 fs	N	80 ± 5 as [32]	[26,30-32]
Two-color gating	< 10 fs	N	~200 as	[33]
IR two-color gating	30 ~ 40 fs	UN	–	[34]
Polarization gating	~5 fs	N	85 as [35]	[35-39]
Double optical gating (DOG)	~8 fs	UN	67 as [40]	[41-46]
Generalized DOG	~25 fs	UN	148 as [47]	[47,48]
IRGDOG	~25 fs	UN	<500 as (calc.)	[49]
Generalized IRDOG	<60 fs	UN	<600 as (calc.)	[49]
Ionization gating (IG)	5~25 fs	UN	~120 as [50]	[50-52]
IG with short pulses	~5 fs	N	160 as	[53]

* N and UN mean CEP locking is necessary and unnecessary, respectively.

In the polarization gating method [35-39], the single-attosecond pulse is generated by focusing a laser pulse which is synthesized with a right-circularly polarized pulse and a delayed left-circularly polarized pulse. This laser pulse is linearly polarized in the middle of the pulse while it is circularly polarized in the sides of the pulse as shown in Fig. 1-4. Because the electron emitted in the first step of the three-step model cannot return to the parent ion in the circularly polarized field, the generation of the harmonics is restricted in the central part of the fundamental pulse, therefore the single-attosecond pulse is generated.

The important parameter in the polarization gating method is the gate width Δt_G defined as [37]

$$\Delta t_G \approx 0.3\varepsilon\tau^2/T_d, \tag{1-3}$$

where ε, τ, and T_d are the ellipticity, pulse duration, and the delay between the first and the second circularly polarized pulses. In the conventional polarization gating method, single attosecond pulses are generated when Δt_G is smaller than the half optical cycle, therefore, the pulse duration of the fundamental laser pulses need to be around 5 fs. In order to enable the single attosecond pulse generation using pulses with longer pulse durations, double optical gating method (DOG), where the fundamental pulses are synthesized with pulses with different colors, was invented [41-46]. In this method, the harmonics are generated only once in one optical cycle, and Δt_G can be twice as large as

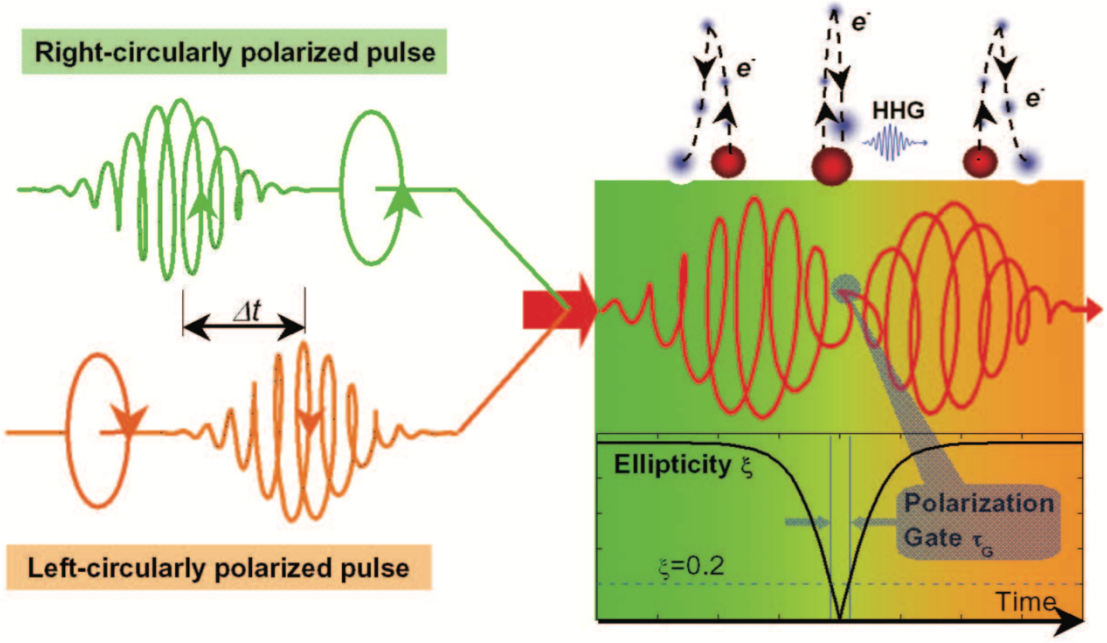

Figure 1-4 Polarization gating method for the generation of high-order harmonics as single attosecond pulses. A pulse which is linearly polarized at the center and circularly polarized in the sides is synthesized from a right-circularly polarized and a left-circularly polarized pulses. By using this pulse, harmonic generation is restricted in the linearly polarized part of the pulse, and single attosecond pulses are obtained. The figure is adopted from ref. [37].

that in the conventional polarization gating method. The limitation of the pulse duration was further eased by using ellipsoidally-polarized pulses (generalized DOG [47,48] or IR generalized DOG [49]), and it has been theoretically suggested that pulses as long as 60 fs can be used as the fundamental pulses when they are ellipsoidally-polarized and their wavelengths are in the infrared region (generalized IR double optical gating method [49]).

In the ionization gating method [50-52], fundamental light pulses are as intense as ~10^{14} W/cm^2, and most of the atoms for the harmonic generation are ionized in the first half of the intense pulse as shown in Fig. 1-5. Because high-order harmonics are generated only when there are neutral atoms, the generation of harmonics in the cut-off region is restricted in the limited part of the pulse. Similar to the amplitude gating method, single-attosecond pulses are obtained by extracting the harmonics in the cut-off region using a mirror or a filter. It is not necessary to use few-femtosecond pulses in this method, but by using few-femtosecond pulses, the extraction of the harmonics in the cut-off region is no longer necessary, and relatively intense single-attosecond pulses are obtained [53].

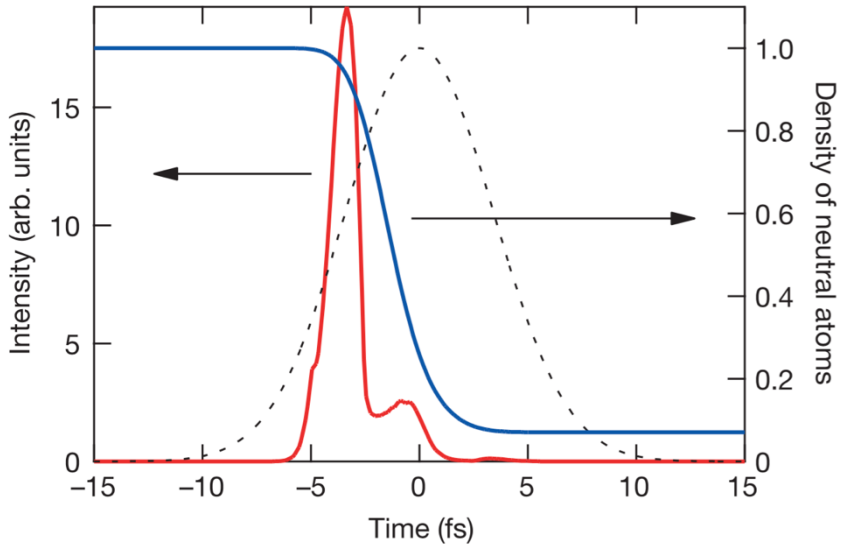

Figure 1-5 Generation of the high-order harmonics as single attosecond pulses by the ionization gating method. The dashed line is the envelope of the fundamental light pulse, the blue line is the density of the neutral atoms, and the red line is the intensity of the ninth harmonic. Almost all of the neutral atoms are depleted in the first half of the fundamental pulse, and harmonic generation is restricted. By extracting the cut-off harmonics in the similar manner as in the amplitude gating method, single attosecond pulses are obtained.

1.4. Photoionization Processes of Rare Gas Atoms

Photo-irradiation of atoms induces various types of ionization processes. When the absorbed photon energy $h\nu$ surpasses the first ionization potential of an atom A, an electron e^- is emitted gaining the excess photon energy, and an energetically allowed state of A^+ is created:

$$A + h\nu \rightarrow A^+ + e^-. \tag{1-4}$$

When the absorbed photon energy coincides with the resonance energy of A, an electron is also emitted from an electronically excited neutral atom A*:

$$A + h\nu \rightarrow A^* \rightarrow A^+ + e^-. \tag{1-5}$$

This process is called an autoionization process. When these two ionization processes, (1-4) and (1-5), having the common states of A and A^+ take place at the same time, these ionization pathways interfere with each other, and a characteristic asymmetric peak appears in an absorption spectrum. The cross section of the excitation to A* was derived by *Fano* [54], and the creation probability of A^+ was calculated based on Fano's theory [8]. As shown in Fig. 1-6, the peak of A^+ creation probability changes its shape from Lorentzian to an asymmetric one as the decay of the autoionizing resonance proceeds.

The lifetime of the autoionizing resonance is equal to the inverse of the peak width, and it is

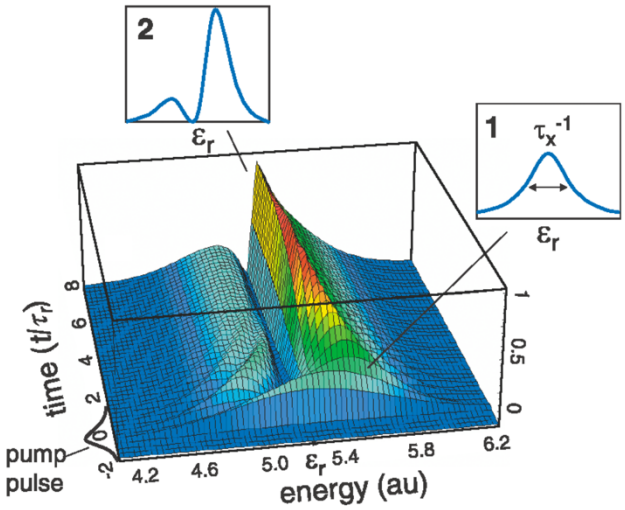

Figure 1-6 Calculated temporal evolution of the creation probability of the singly ionized atom through the autoionization process or the direct ionization process. t and τ_r are time after the irradiation of pump pulse and the lifetime of the autoionizing resonance, respectively. When $t < \tau_r$, the spectral distribution is in the Lorentzian shape as shown in the inset 1, and it transforms to a typical shape in Fano resonance as shown in the inset 2. The figure is adopted from ref. [8].

generally from few tens of attoseconds to few femtoseconds. This means that if the autoionizing resonances interact with a photon introduced before the ultrafast decay process on these time scales, the autoionization process is prevented. *Gilbertson et al.* [55] made use of this for realizing the real-time tracking of the autoionization process. They performed a pump-probe measurement using high-order harmonics and near-infrared (NIR) light pulses with less than 10 fs pulse duration, where the NIR light pulses ionize the atoms in the autoionizing resonance. Because the autoionization proceeds only before the depletion of the autoionizing states by the NIR light pulses, the signals from the autoionization process varies depending on the time delay of the NIR pulses *i.e.* the remaining autoionizing states, and they successfully tracked the autoionization process by measuring the time-delay dependence of the intensity of the signals assigned to the autoionization process.

When the photon energy exceeds the second ionization potential, two electrons, e_1^- and e_2^-, are emitted simultaneously sharing the excess photon energy:

$$A + h\nu \rightarrow A^{2+} + e_1^- + e_2^-. \qquad (1\text{-}6)$$

This process is called a direct double ionization process. The dominant mechanisms of the direct double ionization process are the knockout mechanism and the shake-off mechanism [6]. In the knockout mechanism, one electron gains energy from a photon, and the electron interacts with another electron while it is escaping from the atom. As a result, these electrons are emitted to the same side of the remaining ionic core as shown in Fig. 1-7. This mechanism is dominant when the photon energy

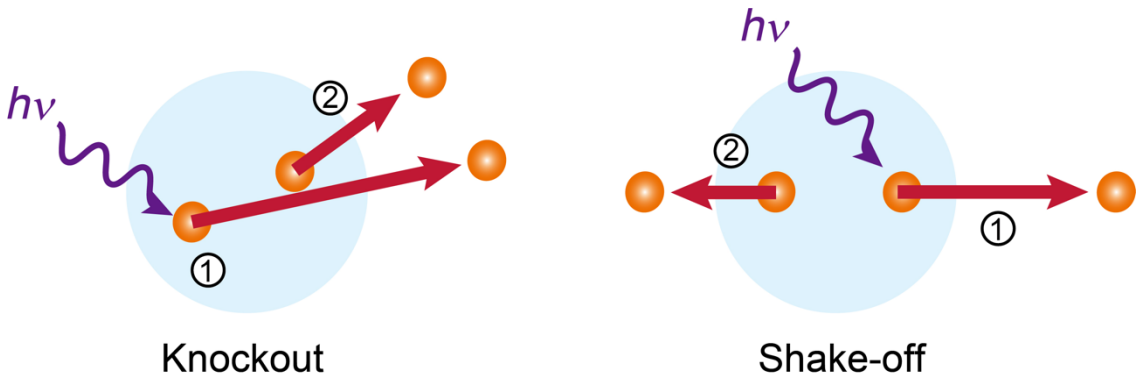

Figure 1-7 Knockout mechanism and shake-off mechanism of direct double ionization process. In the knockout mechanism, one electron absorbs a photon and escapes from the atom. On its way out, the electron collides with another electron, and this electron also escapes from the atom. In the shake-off mechanism, one electron is emitted gaining high kinetic energy, and the secondary electron emission is induced by the sudden change of its environment.

is relatively low because the firstly emitted electron can move slow enough to interact with the second electron [56,57]. In the shake-off mechanism, one electron is suddenly removed by gaining energy from a high-energy photon generally on the order of 100 eV or more [56,57], and the sudden change of the atomic field induces a second electron emission in the opposite direction to the first electron as shown in Fig. 1-7.

Månsson et al. [58] investigated the contribution of these mechanisms in the ionization of Xe irradiated with high-order harmonics and NIR light pulses by a pump-probe photoelectron coincidence measurement. When they changed the time delay between the harmonics and the NIR pulses, the intensity of the peak assigned to the direct double ionization induced by one harmonic photon and one NIR photon oscillated as shown in Fig. 1-8. Because the delay of the oscillation of the intensity of the peak assigned to the direct double ionization to the oscillation of the intensity of the peak assigned to the single ionization creating Xe^+ ($5p^5$) is closer to the one calculated for the shake-off mechanism rather than the one calculated for the knockout mechanism, their result indicated that the shake-off mechanism contributes more in this process although they emphasized the necessity of further theoretical investigations.

The spin state of the electron pair emitted in the direct double ionization process has also been investigated [56,57,59-63]. The electron correlation is indispensable in the direct double ionization process, and it has been theoretically suggested that this electron correlation affects the spin state of the emitted electron pair in the one-photon direct double ionization of atoms with one electron in the outermost orbital: excited He ($1s2s$) [56,57,59,60], ground-state Li ($1s^22s$) [61,62], and excited Be ($1s^22s2p$) [63]. All of these studies showed a preferred emission of two electrons forming the singlet

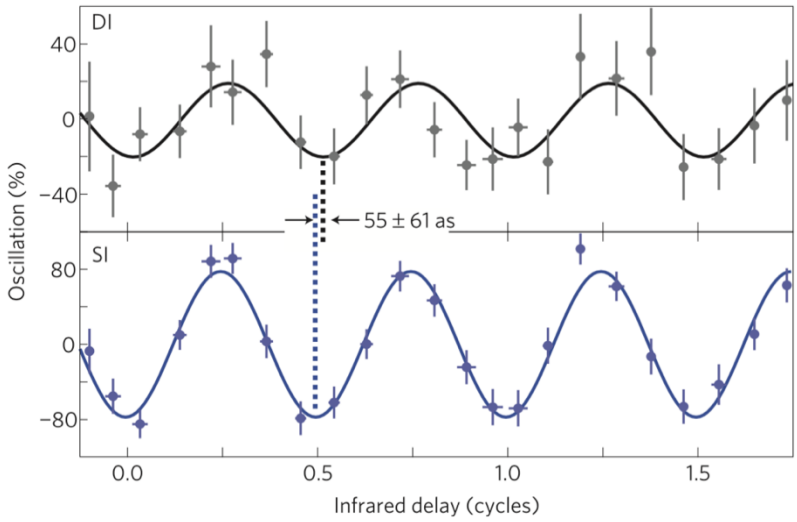

Figure 1-8 Oscillations of the intensity of the peak assigned to the direct double ionization induced by high-order harmonics and near-infrared pulses (black dots) and the intensity of the peak assigned to the single ionization induced by high-order harmonics and near-infrared pulses (blue dots). The oscillation of the peak assigned to the double ionization was shifted from the oscillation of the peak assigned to the single ionization by 55 ± 61 as. The figure is adopted from ref. [56].

state. More details of these theoretical studies will be described in Chapter 2.

Although the preference of the singlet electron pair emission has not been experimentally observed, the preference is expected to appear as the deviation of the population distribution of the resultant doubly charged states from the statistical weight. For example, when the ions are created in the ^3P state and in the ^1P state by a direct double ionization of an atom in the ground ^1S state, the population distribution is expected to be $^3P : {}^1P = 3 : 1$ according to the statistical weight [64]. However, if the singlet electron pair emission is preferred, the fraction of the ions in the ^1P state increases because of the conservation of the total spin angular momentum. In other words, the spin state of the emitted electron pair can be indirectly investigated by measuring the spin state of the created doubly charged ions as long as the spin state of the initial state is known.

Double ionization also proceeds in two steps by absorbing more than one photon:

$$\mathrm{A} + h\nu \rightarrow \mathrm{A}^+ + \mathrm{e}_1^-, \tag{1-7}$$

$$\mathrm{A}^+ + h\nu \rightarrow \mathrm{A}^{2+} + \mathrm{e}_2^-. \tag{1-8}$$

This process is called a sequential double ionization process. Different from the direct double ionization process, there is no correlation between the emitted electrons in the sequential double ionization process because they are emitted one-by-one. The emitted electrons in the sequential double ionization of atom A described in Eqs. (1-7) and (1-8) are expected to have the fixed energies, $E(\mathrm{e}_1^-)$

and $E(e_2^-)$, calculated as follows:

$$E(e_1^-) = h\nu - E(A^+), \tag{1-9}$$

$$E(e_2^-) = h\nu - [E(A^{2+}) - E(A^+)], \tag{1-10}$$

where $E(A^+)$ and $E(A^{2+})$ are the ionization potential of A^+ and A^{2+} from the neutral ground state, respectively. As a result, when a correlation map of the energies of the electrons emitted in this process is plotted taking the energy of one electron E_1 as the x-axis and taking the energy of the other electron E_2 as the y-axis, the correlation map is expected to show spots peaking at $(E_1, E_2) = (E(e_1^-), E(e_2^-))$ and $(E(e_2^-), E(e_1^-))$.

However, a theoretical study showed that this is not true when the ionization is induced by the light pulses with a several hundred attosecond pulse duration. Fig. 1-9 shows calculated correlation maps of the energies of the electrons emitted in the sequential double ionization process of He. In Fig. 1-9, there are signals between the two spots assigned to the normal sequential double ionization process, and their intensity increased as the pulse duration decreased from 450 as to 150 as [7]. This increase could not be explained by the Fourier broadening of the spectrum of the pulse, therefore, this

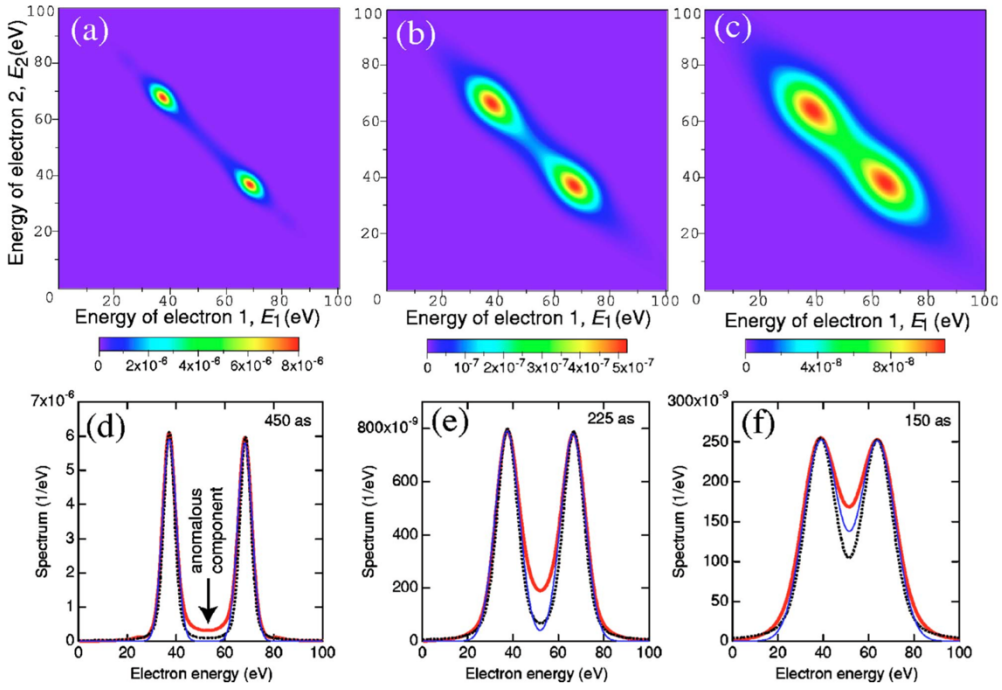

Figure 1-9 Calculated correlation maps of the energies of the electrons emitted in the sequential double ionization of He (a-c) and photoelectron spectra obtained by integrating the signals observed in (a-c) in the direction of E_1 axis (d-f). The duration of the pulses in ionization processes are 450 as (a,d), 225 as (b,e), and 150 as (c,f). The spots observed in (a-c) are assigned to the electron emission through 'normal' sequential double ionization process, where two electrons are not correlated. As the pulse duration decreased, the anomalous component indicated by the arrow in (d) increased. The figure is adopted from ref. [7].

theoretical result suggests that the supposedly independent electrons in the sequential double ionization are no longer independent when the pulse duration is on the order of several hundred attoseconds [7,65-67].

In order to explain the emergence of the additional signals in the correlation maps, three types of correlations in the sequential double ionization process were suggested [7,66]: (i) correlations induced by the Coulomb repulsion between the electrons in the initial state of the atom, (ii) correlations induced when the second electron is emitted while it is still influenced by the polarization of the ion induced by the first electron emission, and (iii) correlations between the electrons both in the continuum. Although *Ishikawa et al.* [7] concluded that the origin of the observed additional signal is mostly (ii) and secondly (iii), *Barna et al.* [65] suggested that the contribution from (i) is more important. Since high-order harmonics with several hundred attosecond pulse duration are now available, experimental studies of sequential double ionization processes induced by very short attosecond pulses may emerge sooner or later, and they are expected to provide useful information for understanding the mechanism of the breakdown of the independent particle model in the sequential double ionization process.

Emission of an inner-shell or core electron can induce the Auger decay process. In the basic type of Auger decay process, the created hole in the inner-shell or core orbital is filled by an electron relaxed from another orbital, and another electron is emitted at the same time (Fig. 1-10 (a)) thanks to the correlations among the electrons in the atom. The time evolution of the Auger decay process has been investigated by a pump-probe measurement using attosecond high-order harmonics and few femtosecond infrared light pulses. In the case of the Auger decay process of Kr, the lifetime of the hole created in the 3*d* orbital was measured to be $7.9^{+1.0}_{-0.9}$ fs [68].

In addition to this basic type of Auger decay process, there are three types of relatively minor Auger decay processes (Fig. 1-10) as reviewed in ref. [9]: (i) the double Auger decay process [69-71], where two electrons are emitted after the hole is filled, (ii) the triple Auger decay process [69], where three electrons are emitted after the hole is filled, and (iii) the collective Auger decay process [72], where two holes are created and one electron is emitted while these holes are filled. These processes are generally initiated by creating a hole in an atom by a high-energy photon from free electron lasers, and they are identified by performing a multi-electron coincidence measurement.

Many of the investigations of the Auger decay processes of rare gas atoms have been performed by using free electron lasers because the first electron needs to be emitted from a deep enough orbital to induce the Auger decay process. For example, the Auger decay process does not occur when an electron in the second outermost orbital of Ar is removed by the irradiation of a photon with the energy of ~30 eV, and a radiative relaxation of an electron from the outermost orbital proceeds instead. This

is because the energy released in the relaxation of the outermost electron is not enough to induce the secondary electron emission. However, it has been suggested in 2011 that the Auger decay can proceed when there is an additional laser field [10,11]. This process is called a laser-enabled Auger decay (LEAD) process. In the LEAD process, the additional laser field compensates the energy deficiency for the secondary electron emission. Because this process is sensitive to the position of the hole, it has been theoretically suggested that the LEAD process can be applied to the observation of the ultrafast charge migration process within a molecule [73]. However, the existence of the LEAD process has been only indicated as the increase of the doubly charged ion yield. With photoelectron coincidence spectroscopy, the existence of the LEAD process can be proven more directly, and more insights into the LEAD process can be obtained. More details will be introduced in Chapter 3.

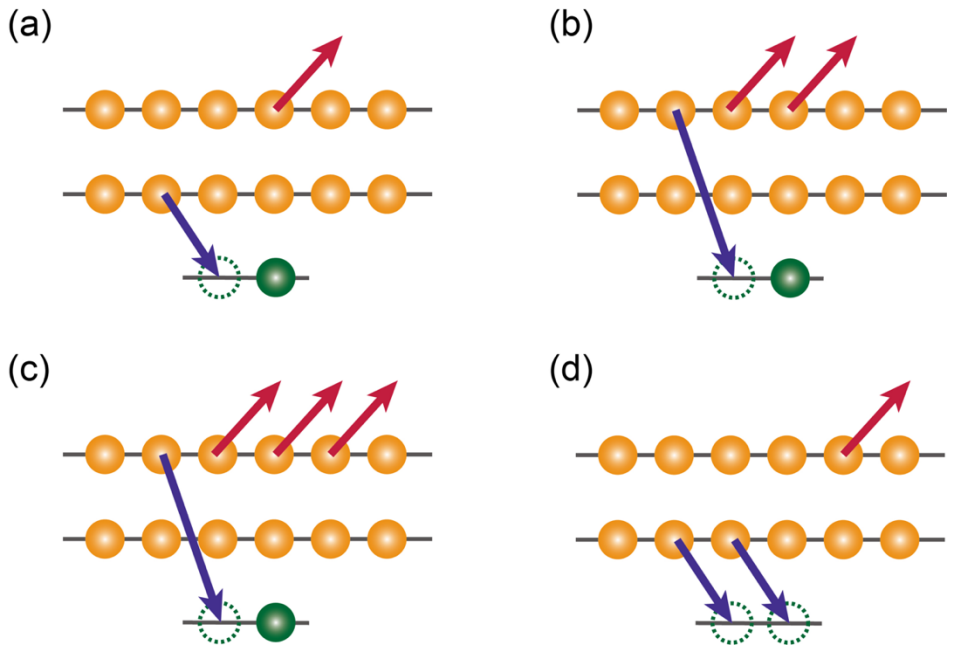

Figure 1-10 Schematic of Auger decay processes. (a) In the basic Auger decay process, one hole is created and one electron is emitted when the hole is filled with an electron. In the other minor Auger decay processes, (b) two electrons are emitted, (c) three electrons are emitted, and (d) one electron is emitted while two holes are filled.

1.5. Present Studies

As described in section 1.4, there are many types of photoionization processes, and high-order harmonics are very useful in the investigation of these processes. Although the photoionization processes have been investigated for a long time, there are still a number of phenomena related to the photoionization processes which remain to be clarified. For example, it has been theoretically suggested that the electron correlation induces a preferential emission of the singlet electron pair in the direct double ionization process of a few-electron atom having one electron in the outermost orbital [56,57,59-63], but the experimental observation of the preferential emission has not been realized neither in the ionization of a few-electron atom nor in the ionization of a many-electron atom. The preference of the singlet electron pair emission is expected to appear as the deviation of the population distribution of the resultant doubly charged ions from the statistical weight, therefore, the spin state of the emitted electron pair can be investigated by measuring the population distribution. Such a measurement might also reveal other causes which affect the population distribution.

Coincidence measurement of the electrons emitted in the recently suggested LEAD process [10,11] is expected to give us more information on the LEAD process. For example, the signals from the LEAD process can be distinguished from those of the other ionization processes, and the existence of this process can be proven more directly than from the ion yields. With this measurement, the contribution of the LEAD process to the double ionization can also be investigated. It is important to know the contribution of the LEAD process when we consider the application of this process to the observation of the ultrafast charge migration process [73].

In this thesis, we experimentally investigated the population distribution of the doubly charged ions created by the direct double ionization of excited rare gas atoms having one electron in the outermost orbital, and we also tried to experimentally observe the LEAD process. In both of the investigations, high-order harmonics generated by the loosely focusing configuration were used for the ionization, and we performed photoelectron coincidence measurements.

The single attosecond pulses described in section 1.3 are expected to be useful for the investigation of the breakdown of the independent particle model in the sequential double ionization process and also for the investigation of the effect of the electronic behaviors in the early stage of the chemical reactions, such as the ultrafast charge migration process, to the following reactions. In order to perform experiments using single attosecond pulses in addition to experiments using attosecond pulse trains, we are constructing an experimental setup for the pump-probe measurement with a high-temporal resolution.

The overviews of the works performed in this thesis are provided below.

State selective two-photon double ionization of rare gas atoms

In order to clarify the causes which induce the deviation of the population distribution from the statistical weights in direct double ionization processes, we prepared the excited rare gas atoms having one electron in the outermost orbital by the irradiation of high-order harmonics, and the direct double ionization of these atoms was induced by another harmonic photon. The excited rare gas atoms are prepared in the autoionizing states, but the double photoionization of these atoms proceeded instead of the autoionization process because the pulse duration of the harmonics was much shorter than the lifetime of the autoionizing resonances. Coincidence photoelectron spectroscopy revealed that this type of double ionization process selectively creates only one state of the doubly charged atom. Although the deviation of the population distribution has been reported in threshold direct double ionization processes of rare gas atoms in the neutral ground state [74] and in a sequential double ionization process of Ar atom via an intermediate state [75-78], none of these processes showed this kind of selectivity. We considered what are implied in the observed selectivity focusing on the electron configuration and the spin state in this process. This work is described in Chapter 2.

Observation of laser-enabled Auger decay process by coincidence photoelectron spectroscopy

A preliminary experiment of the observation of the LEAD process was performed by irradiating Ar atoms with high-order harmonics of near-infrared light pulses to remove an inner-valence electron and with a delayed infrared light pulses to induce the LEAD process. We tried to extract the signals only from the LEAD process in the correlation map of the energies of the coincidently detected electrons. This work is described in Chapter 3.

Development of pump-probe experimental setup for observation of ultrafast phenomena with high-temporal resolution

We are constructing a new experimental setup designed for the pump-probe measurement of ultrafast phenomena with attosecond temporal accuracy. The setup consists of a high-order harmonic generation part, optics for pump-probe measurements, a photoelectron spectrometer, and an extreme ultraviolet spectrometer. Because the pump-probe measurements with high temporal resolution are very sensitive to the unwanted mechanical vibrations introduced to the optics, chambers were designed to suppress the vibrations. The design and the current status of the setup are described in Chapter 4.

[1] P. B. Corkum, Phys. Rev. Lett. **71**, 1994 (1993).

[2] K. Midorikawa, Y. Nabekawa, and A. Suda, Prog. Quant. Electron. **32**, 43 (2008).

[3] T. Shintake, H. Tanaka, T. Hara, T. Tanaka, K. Togawa, M. Yabashi, Y. Otake, Y. Asano, T. Bizen, T. Fukui, S. Goto, A. Higashiya, T. Hirono, N. Hosoda, T. Inagaki, S. Inoue, M. Ishii, Y. Kim, H. Kimura, M. Kitamura, T. Kobayashi, H. Maesaka, T. Masuda, S. Matsui, T. Matsushita, X. Maréchal, M. Nagasono, H. Ohashi, T. Ohata, T. Ohshima, K. Onoe, K. Shirasawa, T. Takagi, S. Takahashi, M. Takeuchi, K. Tamasaku, R. Tanaka, Y. Tanaka, T. Tanikawa, T. Togashi, S. Wu, A. Yamashita, K. Yanagida, C. Zhang, H. Kitamura, and T. Ishikawa, Nat. Photonics **2**, 555 (2008).

[4] K. Midorikawa, Jpn. J. Appl. Phys. **50**, 090001 (2011).

[5] L. Plaja, R. Torres, and A. Zaïr, *Attosecond Physics: Attosecond Measurements and Control of Physical Systems* (Springer, Berlin, 2013).

[6] Z.-J. Teng and R. Shakeshaft, Phys. Rev. A **49**, 3597 (1994).

[7] K. L. Ishikawa and K. Midorikawa, Phys. Rev. A **72**, 013407 (2005).

[8] M. Wickenhauser, M. Wickenhauser, J. Burgdörfer, J. Burgdörfer, F. Krausz, F. Krausz, M. Drescher, and M. Drescher, Phys. Rev. Lett. **94**, 023002 (2005).

[9] P. Kolorenč, V. Averbukh, and R. Feifel, J. Phys. B **49**, 082001 (2016).

[10] P. Ranitovic, X. M. Tong, C. W. Hogle, X. Zhou, Y. Liu, N. Toshima, M. M. Murnane, and H. C. Kapteyn, Phys. Rev. Lett. **106**, 053002 (2011).

[11] X. M. Tong, P. Ranitovic, C. W. Hogle, M. M. Murnane, H. C. Kapteyn, and N. Toshima, Phys. Rev. A **84**, 013405 (2011).

[12] S. Ghimire, A. D. DiChiara, E. Sistrunk, P. Agostini, L. F. DiMauro, and D. A. Reis, Nat. Phys. **7**, 138 (2011).

[13] K. Schafer, B. Yang, L. DiMauro, and K. Kulander, Phys. Rev. Lett. **70**, 1599 (1993).

[14] T. Brabec and F. Krausz, Rev. Mod. Phys. **72**, 545 (2000).

[15] Z. Chang, A. Rundquist, H. Wang, M. M. Murnane, and H. C. Kapteyn, Phys. Rev. Lett. **79**, 2967 (1997).

[16] C. Spielmann, N. H. Burnett, S. Sartania, R. Koppitsch, M. Schnürer, C. Kan, M. Lenzner, P. Wobrauschek, and F. Krausz, Science **278**, 661 (1997).

[17] T. Gorniak, R. Heine, A. P. Mancuso, F. Staier, C. Christophis, M. E. Pettitt, A. Sakdinawat, R. Treusch, N. Guerassimova, J. Feldhaus, C. Gutt, G. Grübel, S. Eisebitt, A. Beyer, A. Gölzhäuser, E. Weckert, M. Grunze, I. A. Vartanyants, and A. Rosenhahn, Opt. Express **19**, 11059 (2011).

[18] A. Rundquist, C. G. Durfee, Z. Chang, C. Herne, S. Backus, M. M. Murnane, and H. C. Kapteyn,

Science **280**, 1412 (1998).

[19] E. Constant, D. Garzella, P. Breger, E. Mével, C. Dorrer, C. Le Blanc, F. Salin, and P. Agostini, Phys. Rev. Lett. **82**, 1668 (1999).

[20] Y. Tamaki, Y. Nagata, M. Obara, and K. Midorikawa, Phys. Rev. A **59**, 4041 (1999).

[21] Y. Tamaki, J. Itatani, Y. Nagata, M. Obara, and K. Midorikawa, Phys. Rev. Lett. **82**, 1422 (1999).

[22] Y. Tamaki, J. Itatani, M. Obara, and K. Midorikawa, Phys. Rev. A **62**, 063802 (2000).

[23] Y. Tamaki, J. Itatani, M. Obara, and K. Midorikawa, Jpn. J. Appl. Phys. **40**, L1154 (2001).

[24] E. Takahashi, Y. Nabekawa, M. Nurhuda, and K. Midorikawa, J. Opt. Soc. Am. B **20**, 158 (2003).

[25] H. Hasegawa, E. J. Takahashi, Y. Nabekawa, K. L. Ishikawa, and K. Midorikawa, Phys. Rev. A **71**, 023407 (2005).

[26] M. Hentschel, R. Kienberger, C. Spielmann, G. A. Reider, N. Milosevic, T. Brabec, P. Corkum, U. Heinzmann, M. Drescher, and F. Krausz, Nature **414**, 509 (2001).

[27] C. Altucci, J. W. G. Tisch, and R. Velotta, J. Mod. Opt. **58**, 1585 (2011).

[28] G. Sansone, L. Poletto, and M. Nisoli, Nat. Photonics **5**, 655 (2011).

[29] M. Chini, K. Zhao, and Z. Chang, Nat. Photonics **8**, 178 (2014).

[30] A. Baltuška, T. Udem, M. Uiberacker, M. Hentschel, E. Goulielmakis, C. Gohle, R. Holzwarth, V. S. Yakovlev, A. Scrinzi, T. W. Hänsch, and F. Krausz, Nature **421**, 611 (2003).

[31] R. Kienberger, E. Goulielmakis, M. Uiberacker, A. Baltuška, V. Yakovlev, F. Bammer, A. Scrinzi, T. Westerwalbesloh, U. Kleineberg, U. Heinzmann, M. Drescher, and F. Krausz, Nature **427**, 817 (2004).

[32] E. Goulielmakis, M. Schultze, M. Hofstetter, V. S. Yakovlev, J. Gagnon, M. Uiberacker, A. L. Aquila, E. M. Gullikson, D. T. Attwood, R. Kienberger, F. Krausz, and U. Kleineberg, Science **320**, 1614 (2008).

[33] Y. Oishi, M. Kaku, A. Suda, F. Kannari, and K. Midorikawa, Opt. Express **14**, 7230 (2006).

[34] E. J. Takahashi, P. Lan, O. D. Mücke, Y. Nabekawa, and K. Midorikawa, Phys. Rev. Lett. **104**, 233901 (2010).

[35] I. J. Sola, E. Mével, L. Elouga, E. Constant, V. Strelkov, L. Poletto, P. Villoresi, E. Benedetti, J. P. Caumes, S. Stagira, C. Vozzi, G. Sansone, and M. Nisoli, Nat. Phys. **2**, 319 (2006).

[36] Z. Chang, Phys. Rev. A **70**, 043802 (2004).

[37] B. Shan, B. Shan, S. Ghimire, Z. Chang, S. Ghimire, and Z. Chang, J. Mod. Opt. **52**, 277 (2005).

[38] G. Sansone, E. Benedetti, F. Calegari, C. Vozzi, L. Avaldi, R. Flammini, L. Poletto, P. Villoresi, C. Altucci, R. Velotta, S. Stagira, S. De Silvestri, and M. Nisoli, Science **314**, 443 (2006).

[39] C. Marceau, O. Society, G. Gingras, and B. Witzel, Opt. Express **19**, 3576 (2011).

[40] K. Zhao, Q. Zhang, M. Chini, Y. Wu, X. Wang, and Z. Chang, Opt. Lett. **37**, 3891 (2012).

[41] Z. Chang, Phys. Rev. A **76**, 051403 (2007).

[42] H. Mashiko, S. Gilbertson, C. Li, S. D. Khan, M. M. Shakya, E. Moon, and Z. Chang, Phys. Rev. Lett. **100**, 103906 (2008).

[43] H. Mashiko, S. Gilbertson, C. Li, E. Moon, and Z. Chang, Phys. Rev. A **77**, 063423 (2008).

[44] H. Mashiko, S. Gilbertson, M. Chini, X. Feng, C. Yun, H. Wang, S. D. Khan, S. Chen, and Z. Chang, Opt. Lett. **34**, 3337 (2009).

[45] H. Mashiko, M. J. Bell, A. R. Beck, M. J. Abel, P. M. Nagel, C. P. Steiner, J. Robinson, D. M. Neumark, and S. R. Leone, Opt. Express **18**, 25887 (2010).

[46] K. Zhao, Q. Zhang, M. Chini, Y. Wu, X. Wang, and Z. Chang, Opt. Lett. **37**, 3891 (2012).

[47] X. Feng, X. Feng, S. Gilbertson, S. Gilbertson, H. Mashiko, H. Mashiko, H. Wang, H. Wang, S. D. Khan, S. D. Khan, M. Chini, Y. Wu, K. Zhao, and Z. Chang, Phys. Rev. Lett. **103**, 183901 (2009).

[48] S. Gilbertson, S. D. Khan, Y. Wu, M. Chini, and Z. Chang, Phys. Rev. Lett. **105**, 093902 (2010).

[49] P. Lan, E. J. Takahashi, and K. Midorikawa, Phys. Rev. A **83**, 063839 (2011).

[50] T. Pfeifer, A. Jullien, M. J. Abel, P. M. Nagel, L. Gallmann, D. M. Neumark, and S. R. Leone, Opt. Express **15**, 17120 (2007).

[51] T. Sekikawa, A. Kosuge, T. Kanai, and S. Watanabe, Nature **432**, 605 (2004).

[52] M. J. Abel, M. J. Abel, T. Pfeifer, T. Pfeifer, P. M. Nagel, P. M. Nagel, W. Boutu, M. J. Bell, W. Boutu, M. J. Bell, C. P. Steiner, D. M. Neumark, and S. R. Leone, Chem. Phys. **366**, 9 (2009).

[53] F. Ferrari, F. Calegari, M. Lucchini, C. Vozzi, S. Stagira, G. Sansone, and M. Nisoli, Nat. Photonics **4**, 875 (2010).

[54] U. Fano, Phys. Rev. Lett. **124**, 1866 (1961).

[55] S. Gilbertson, M. Chini, X. Feng, S. Khan, Y. Wu, and Z. Chang, Phys. Rev. Lett. **105**, 263003 (2010).

[56] A. Emmanouilidou, T. Schneider, and J.-M. Rost, J. Phys. B **36**, 2717 (2003).

[57] A. S. Kheifets, A. Ipatov, M. Arifin, and I. Bray, Phys. Rev. A **62**, 052724 (2000).

[58] E. P. Månsson, D. Guénot, C. L. Arnold, D. Kroon, S. Kasper, J. M. Dahlström, E. Lindroth, A. S. Kheifets, A. L'Huillier, S. L. Sorensen, and M. Gisselbrecht, Nat. Phys. **10**, 207 (2014).

[59] H. W. van der Hart, K. W. Meyer, and C. H. Greene, Phys. Rev. A **57**, 3641 (1998).

[60] J. Colgan and M. S. Pindzola, Phys. Rev. A **67**, 012711 (2003).

[61] J. Colgan, D. C. Griffin, C. P. Ballance, and M. S. Pindzola, Phys. Rev. A **80**, 063414 (2009).

[62] A. S. Kheifets, D. V. Fursa, C. W. Hines, I. Bray, J. Colgan, and M. S. Pindzola, Phys. Rev. A

81, 023418 (2010).

[63] F. L. Yip, C. W. McCurdy, and T. N. Rescigno, Phys. Rev. A **81**, 063419 (2010).

[64] J. H. D. Eland, *Photoelectron Spectroscopy* (Butterworths, London, 1974).

[65] I. F. Barna, J. Wang, and J. Burgdörfer, Phys. Rev. A **73**, 023402 (2006).

[66] J. Feist, S. Nagele, R. Pazourek, E. Persson, B. I. Schneider, L. A. Collins, and J. Burgdörfer, Phys. Rev. Lett. **103**, 063002 (2009).

[67] G. Sansone, T. Pfeifer, K. Simeonidis, and A. I. Kuleff, Chem. Phys. Chem. **13**, 661 (2012).

[68] M. Drescher, M. Hentschel, R. Kienberger, M. Uiberacker, V. Yakovlev, A. Scrinzi, T. Westerwalbesloh, U. Kleineberg, U. Heinzmann, and F. Krausz, Nature **419**, 803 (2002).

[69] Y. Hikosaka, P. Lablanquie, F. Penent, T. Kaneyasu, E. Shigemasa, J. H. D. Eland, T. Aoto, and K. Ito, Phys. Rev. A **76**, 032708 (2007).

[70] E. Andersson, S. Fritzsche, P. Linusson, L. Hedin, J. H. D. Eland, J. E. Rubensson, L. Karlsson, and R. Feifel, Phys. Rev. A **82**, 043418 (2010).

[71] Y. Hikosaka, T. Kaneyasu, P. Lablanquie, and F. Penent, Phys. Rev. A **92**, 033413 (2015).

[72] J. H. D. Eland, R. J. Squibb, M. Mucke, S. Zagorodskikh, P. Linusson, and R. Feifel, New J. Phys. **17**, 122001 (2015).

[73] B. Cooper and V. Averbukh, Phys. Rev. Lett. **111**, 083004 (2013).

[74] A. Huetz, P. Selles, D. Waymel, and J. Mazeau, J. Phys. B **24**, 1917 (1991).

[75] Y. Hikosaka, M. Fushitani, A. Matsuda, C. M. Tseng, A. Hishikawa, E. Shigemasa, M. Nagasono, K. Tono, T. Togashi, H. Ohashi, H. Kimura, Y. Senba, M. Yabashi, and T. Ishikawa, Phys. Rev. Lett. **105**, 133001 (2010).

[76] N. Miyauchi, J. Adachi, A. Yagishita, T. Sako, F. Koike, T. Sato, A. Iwasaki, T. Okino, K. Yamanouchi, K. Midorikawa, K. Yamakawa, F. Kannari, H. Nakano, M. Nagasono, K. Tono, M. Yabashi, T. Ishikawa, T. Togashi, H. Ohashi, H. Kimura, and Y. Senba, J. Phys. B **44**, 071001 (2011).

[77] H. Fukuzawa, E. V. Gryzlova, K. Motomura, A. Yamada, K. Ueda, A. N. Grum-Grzhimailo, S. I. Strakhova, K. Nagaya, A. Sugishima, Y. Mizoguchi, H. Iwayama, M. Yao, N. Saito, P. Piseri, T. Mazza, M. Devetta, M. Coreno, M. Nagasono, K. Tono, M. Yabashi, T. Ishikawa, H. Ohashi, H. Kimura, T. Togashi, and Y. Senba, J. Phys. B **43**, 111001 (2010).

[78] E. V. Gryzlova, R. Ma, H. Fukuzawa, K. Motomura, A. Yamada, K. Ueda, A. N. Grum-Grzhimailo, N. M. Kabachnik, S. I. Strakhova, A. Rouzée, A. Hundermark, M. J. J. Vrakking, P. Johnsson, K. Nagaya, S. Yase, Y. Mizoguchi, M. Yao, M. Nagasono, K. Tono, T. Togashi, Y. Senba, H. Ohashi, M. Yabashi, and T. Ishikawa, Phys. Rev. A **84**, 063405 (2011).

Chapter 2

State Selective Two-Photon Double Ionization of Rare Gas Atoms

Simultaneous two-electron emission processes of Ar induced by high-order harmonics of near-infrared femtosecond laser pulses were investigated by coincidence photoelectron spectroscopy. Two-photon double ionization processes via the $3s3p^6np$ ($n \sim 25$) intermediate resonances of Ar were observed, which selectively created the $3s3p^5\ ^1P$ state of Ar^{2+}. The similar double ionization processes were also observed in Kr. The selective creation indicates that the core electron configuration of the doubly ionized state tends to be the same as that of the intermediate state and that the emitted two electrons tend to form the singlet state. Parts of this chapter is published in ref. [1].

2.1. Introduction

In one-photon single ionization processes of rare gas atoms, it has been known that the resultant energetically allowed singly charged states are populated according to their statistical weight [2]: When one outermost *np* electron is emitted, the population distribution of the resultant $^2P_{1/2}$ and $^2P_{3/2}$ levels is $^2P_{1/2} : {}^2P_{3/2} = 1 : 2$ (Fig. 2-1(a),1(b)). However, in the case of one-photon double ionization processes (Fig. 2-1(c),1(d)), it has been reported that the population distribution can deviate from the statistical weight of $^1S_0 : {}^1D_2 : {}^3P_{2,1,0} = 1 : 5 : 9$ [3-5], and the deviation has also been observed in a multi-photon sequential double ionization process [6-8]. The origin of these deviations in the double photoionization of atoms has been an attractive issue in recent decades [3-15].

In this section, previously reported deviations of the population distribution in double photoionization processes and their mechanisms are introduced. Then I describe a possibility of the deviation in another double photoionization process, and introduce our work.

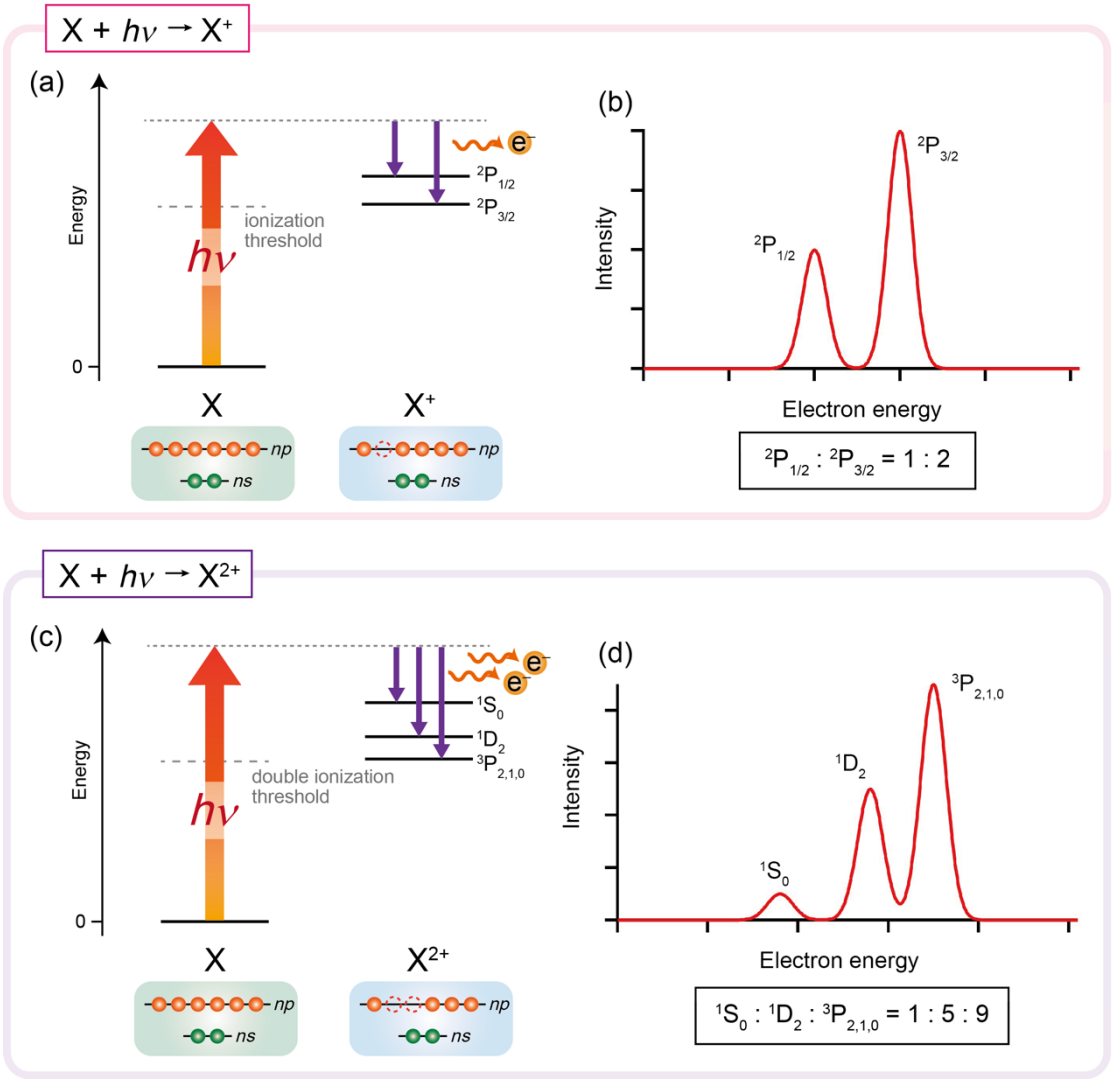

Figure 2-1 (a,c) Schematics of one-photon ionization processes and (b,d) energy distributions of photoelectrons expected from their statistical weights. In the one-photon single ionization process of rare gas atoms (a,b), *np* electron emission creates singly charged ion in the $^2P_{1/2}$ and $^2P_{3/2}$ levels, and the population distribution is $^2P_{1/2}$: $^2P_{3/2}$ = 1 : 2. In the one-photon double ionization process of rare gas atoms (c,d), emission of two *np* electrons creates doubly charged ion in the ^1S, ^1D, and ^3P states, and the population distribution is ^1S : ^1D : ^3P = 1 : 5 : 9. However, the population distribution in the double ionization process does not necessarily follow the statistical weight. See the text for more detail.

2.1.1. Previous Studies of Population Distribution in Double Ionization

2.1.1.1. Threshold Direct Double Ionization

In a threshold direct double ionization process, a simultaneous two-electron emission is induced by one photon whose energy is close to the energy of the resultant doubly charged state from the neutral ground state. It has been known that this process follows the extended Wannier's law, and the total angular momentum L, spin S, and parity π of the emitted electron pair tend to be all odd or all even.

The extended Wannier's law has been originally derived for the electron impact ionization of a singly charged positive atom [16]. In 1970s, the cross section of the electron impact ionization was actively investigated. *Wannier* showed that the Wannier ridge, where the two electrons leave the parent ion to the opposite directions having the same kinetic energies (Fig. 2-2), is important in the threshold electron impact ionization process. He derived that the cross section σ of the ionization is written as

$$\sigma \propto E^m, \tag{2-1}$$

where E is the excess photon energy, and m is 1.127 when the emitted electron pair is forming the ${}^1S^e$ state [17]. Later on, it has been shown that the m value is 3.881 when the emitted electron pair is in the ${}^3S$ or ${}^1P^e$ states [18]. This means that σ is smaller for the emission of the electron pair in the ${}^3S$ or ${}^1P^e$ states rather than the emission of the electron pair in the ${}^1S^e$ state. This smaller σ is caused by the existence of the nodes in the two-electron wave functions when they are in the ${}^3S$ or ${}^1P^e$ states [19]. *Stauffer* focused on the fact that σ becomes smaller when the wave function of the emitted electron pair has nodes, and showed that the two-electron wave function has no nodes at the Wannier ridge

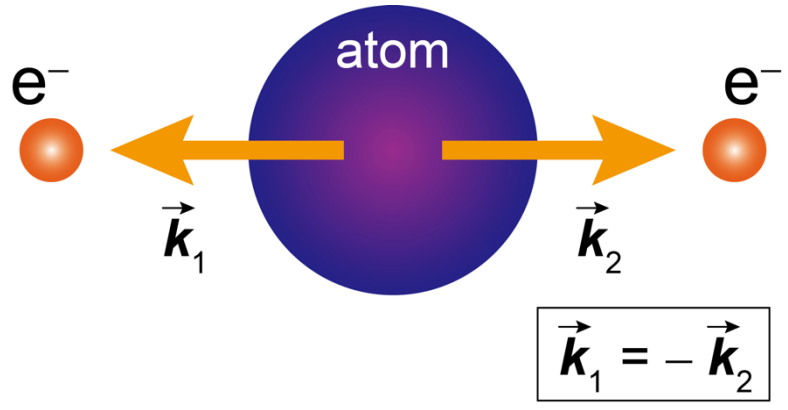

Figure 2-2 Positions of an atom and emitted electrons at the Wannier ridge. In a threshold ionization process, the electrons are emitted in the opposite directions having the same kinetic energies.

when L, S, and π are all odd or all even [16]. Because the Wannier ridge is important in the threshold electron impact ionization process, σ is large when L, S, and π are all odd or all even. This propensity is called the extended Wannier's law.

It has been known that the electron impact ionization process is similar to the direct double photoionization process when the dominant mechanism is the knockout mechanism, in which one electron gains the photon energy and the electron knocks out another electron as it escapes from the atom [10,12]. Because the knockout mechanism is dominant when the excess photon energy is small, this mechanism is expected to be dominant in the threshold direct double ionization process, and the process is expected to show a similar propensity to the one shown in the electron impact ionization process.

The applicability of the extended Wannier's law to the threshold direct double ionization process has been theoretically investigated by *Huetz et al.* [20]. They described the positions of the electrons by using angles θ_1, φ_1, θ_{12}, and Ψ_B. The definitions of the angles θ_1, φ_1 and θ_{12} are depicted in Fig. 2-3, and Ψ_B is defined as the angle between the (O, e_1, e_2) and (O, e_1, z) planes. Using these angles, they derived the triple differential cross section,

$$\frac{d^3\sigma}{dE_1 d\Omega} = g \sum_{mMM_i} \left| \sum_L \langle L_i M_i LM | lm \rangle a_{LS\pi} E^{m_{LS\pi}} B_{LMS\pi}(\theta_{12}, \varphi_1, \theta_1, \Psi_B) \right|^2 G(180° - \theta_{12}), \quad (2\text{-}2)$$

where E_1 is the energy of e_1 in Fig. 2-3, and Ω is the collective solid angle relating to θ_1, φ_1, θ_{12}, and Ψ_B. g is 1 when the photon is linearly polarized and 0.5 when the photon is unpolarized.

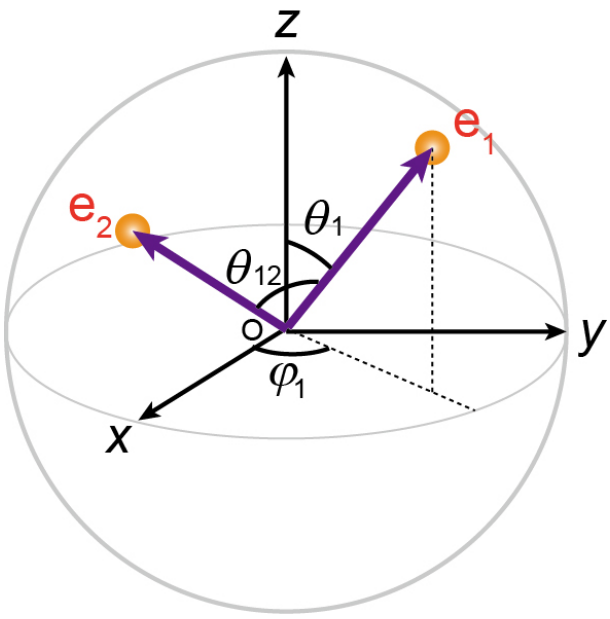

Figure 2-3 Definitions of angles θ_1, φ_1, and θ_{12} for describing the positions of the electrons escaping from the parent ion at the point of origin (O).

$\langle L_i M_i L M | lm \rangle$ is a vector coupling coefficient, $a_{LS\pi}$ is a constant defined for each state of the escaping electron pair, E is the excess photon energy, and $B_{LMS\pi}$ is the angular factor of the two-electron wave function for each state. $m_{LS\pi}$ is defined as

$$m_{LS\pi} = 0.5n - 0.75 - 0.25q_{LS\pi}, \tag{2-3}$$

where $n = 1.056$ is the threshold exponent and $q_{LS\pi}$ is the number of nodes in the function $B_{LMS\pi}$ at $\theta_{12} = 180°$. The function $G(180° - \theta_{12})$ is written as

$$G(180° - \theta_{12}) = \exp\left[-4 \ln 2 \, (180° - \theta_{12})^2 \big/ \left(\theta_0 E^{0.25}\right)^2\right], \tag{2-4}$$

where θ_0 is proposed to be either 103 deg $eV^{-0.25}$ [21] or 91 deg $eV^{-0.25}$ [22,23] when the ion is doubly charged. When we define a function $I_{i,j}(E)$ as

$$I_{i,j}(E) = \int_0^{180°} \cos^i(0.5\theta_{12}) \sin^j(0.5\theta_{12}) G(180° - \theta_{12}) \, d\theta_{12}, \tag{2-5}$$

the energy-dependent double ionization cross section $\sigma(E)$ of each state of the emitted electron pair is derived by integrating Eq. (2-2) as

$$\sigma(E) = \begin{cases} \dfrac{32}{3} I_{3,1}(E) |a_{LS\pi}|^2 E^{n-1} & \text{for } {}^1P^o \\ \dfrac{32}{3} I_{1,3}(E) |a_{LS\pi}|^2 E^{n-0.5} & \text{for } {}^3P^o \\ \dfrac{128}{3} I_{3,5}(E) |a_{LS\pi}|^2 E^{n-1} & \text{for } {}^1D^o \\ \dfrac{128}{3} I_{5,3}(E) |a_{LS\pi}|^2 E^{n-1.5} & \text{for } {}^3D^o \end{cases}. \tag{2-6}$$

The calculated $\sigma(E)$ using Eqs. (2-6) are plotted in Fig. 2-4. θ_0 was set to be 91 deg $eV^{-0.25}$ [22,23] in the calculation. Assuming that the values of $a_{LS\pi}$ are similar among ${}^3P^o$, ${}^1D^o$, ${}^1P^o$, and ${}^3D^o$ states, Fig. 2-4 indicates that the emission of the electron pair in the ${}^3P^o$ state is dominant. This means that the extended Wannier's law is also applicable to the threshold direct double ionization process, but the law is more like a weak propensity rule than a strong selectivity rule because the emissions of the electron pair which does not have all odd or all even L, S, and π are not negligibly small.

This propensity of the emitted electron pair induces the deviation of the population distribution of the resultant doubly charged ions. The L, S, and π of the pair of electrons emitted in the creation of doubly charged ion in each state is derived from the conservation rules of **L**, **S**, and π under the LS scheme:

$$\mathbf{L}_{\text{ini}} + \mathbf{L}_{\text{photon}} = \mathbf{L}_{\text{ion}} + \mathbf{L}_{\text{e–e}}, \tag{2-7}$$

$$\mathbf{S}_{\text{ini}} + \mathbf{S}_{\text{photon}} = \mathbf{S}_{\text{ion}} + \mathbf{S}_{\text{e–e}}, \tag{2-8}$$

$$(-1)^{\pi_{\text{ini}}} \cdot (-1)^{\pi_{\text{photon}}} = (-1)^{\pi_{\text{ion}}} \cdot (-1)^{\pi_{\text{e–e}}}, \tag{2-9}$$

where the subscripts, ini, photon, ion, and e–e mean the initial atom, absorbed photon, created doubly charged ion, and the emitted electron pair, respectively. Because the rare gases are initially in the ${}^1S^e$

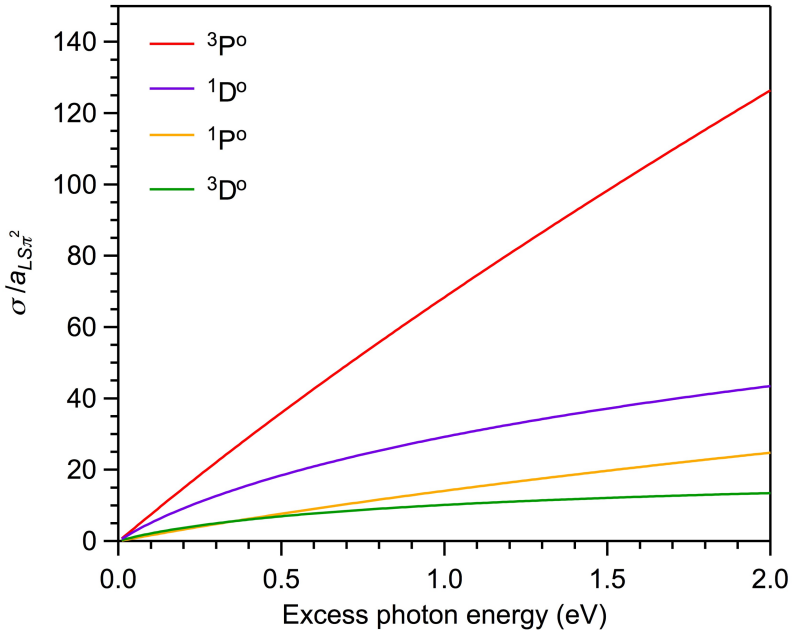

Figure 2-4 Calculated excess photon energy dependence of the cross section divided by the constant, $a_{LS\pi}{}^2$. θ_0 was set to be 91 deg $eV^{-0.25}$ [22,23]. The red, purple, yellow, and green curves correspond to the emissions of the electron pairs in the ${}^3P^o$, ${}^1D^o$, ${}^1P^o$, and ${}^3D^o$ states, respectively.

state and **L**, **S**, and $(-1)^\pi$ of a photon are 1, 0, and −1, respectively, the states of the emitted electrons are derived as listed in Table 2-1.

Table 2-1 Derivation of states of emitted electron pair.

Atom, X	State of X^{2+}	State of electron pair
He	${}^1S^e$	${}^1P^o$
Other rare gases	${}^3P^e$	${}^3P^o$, ${}^3D^o$
	${}^1D^e$	${}^1P^o$, ${}^1D^o$, ${}^1F^o$
	${}^1S^e$	${}^1P^o$

As shown in Table 2-1, only in the creation of X^{2+} in the ${}^3P^e$ state, the emitted electron pair is in the ${}^3P^o$ state, where L, S, and π are all odd. Therefore, the relative yield of X^{2+} in the ${}^3P^e$ state becomes larger than expected from the statistical weight according to the extended Wannier's law.

The deviation of the population distribution of the doubly charged ions was experimentally confirmed by *Hall et al.* [3]. They induced the one-photon threshold double ionization of rare gas atoms by a synchrotron radiation source, and coincidently detected the emitted two electrons having the energy close to zero. When they measured the photon-energy-dependence of the signal intensity,

the creation of the $^3P^e$ state of doubly charged ion was preferred in the double ionization of Ar, Kr, and Xe as expected from the extended Wannier's law (Fig. 2-5). For example in the case of Ar shown in Fig. 2-5(a), the relative peak intensity was ^3P : ^1D : $^1S \approx 110 : 17 : 1$ although the relative intensity expected from the statistical weight is ^3P : ^1D : $^1S = 9 : 5 : 1$.

It was also experimentally confirmed by *Eland et al.* that the extended Wannier's law cannot be applied when the excess photon energy is about 5 eV or more [5]. When they induced one-photon double ionization of Xe, Kr, and Ar using a photon with energy up to 51 eV and measured the distribution of the total energy of the emitted electrons, they found that the population distributions are close to the statistical weight. Furthermore, when the contribution from the autoionization process was taken into account, the yield of the ^3P state of doubly charged ion was even smaller than expected from the statistical weight in their study.

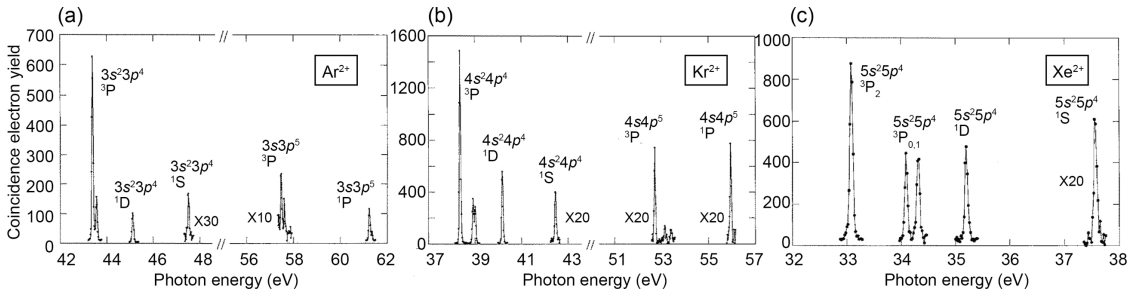

Figure 2-5 Photon energy dependence of the coincidence signal yields. (a) Ar, (b) Kr, and (c) Xe were doubly ionized by one photon, and the emitted electrons having close-to-zero energies were detected. The data are adopted from ref. [3].

2.1.1.2. Spin States of Simultaneously Emitted Electron Pairs

The population distribution of the created doubly ionized states is expected to deviate from the statistical distribution also when there is a preference in the spin state of the electron pairs simultaneously emitted in a one-photon direct double ionization process. The preference in the spin state of the emitted electron pair has been theoretically investigated for the one-photon double ionization of excited He ($1s2s$) [9-12], ground-state Li ($1s^22s$) [13,14], and excited Be ($1s^22s2p$) [15]. The investigations were performed by the *R*-matrix method [9,13], the convergent close-coupling method [10,14], the time-dependent close-coupling method [11,13,14], the exterior complex scaling method [15], and a method in which the knockout process was treated quasiclassically and the shake-

off process was treated quantum mechanically [12]. These studies consistently showed that the emitted electron pair tends to be in the singlet state. For example, in the double photoionization of the ground state of Li, the cross section of the singlet electron pair emission was calculated to be 2.7 times larger than that of the triplet electron pair emission at the excess energy of 5 eV when the statistical weight factors are included [13] as shown in Fig. 2-6.

This tendency emerges qualitatively because the electrons having parallel spins cannot get closer to each other according to Pauli's exclusion principle, and the interaction between them are smaller compared to the antiparallel electron pair [9,12]. Because the interaction between the parallel electrons are smaller, the cross section of the triplet electron pair emission, which includes the parallel electron pair emission, is smaller than that of the singlet electron pair emission.

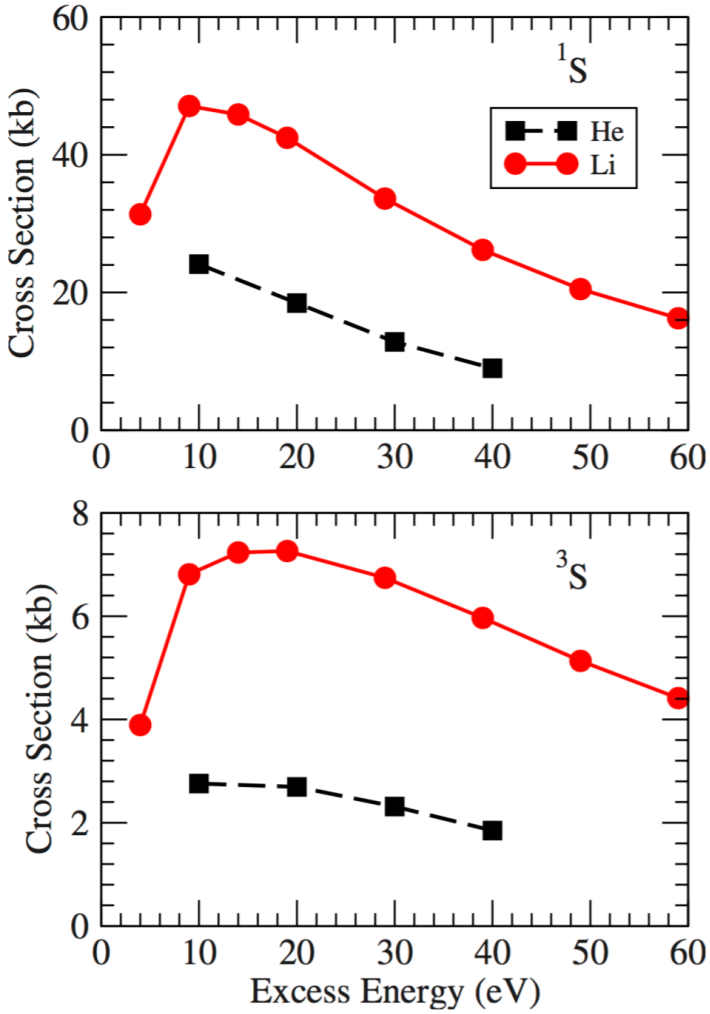

Figure 2-6 Calculated excess energy dependences of the cross sections of singlet electron pair emissions (above) and those of triplet electron pair emissions (bottom). Red dots and black dots correspond to the ionizations of ground-state Li and excited He, respectively. The figure is adopted from ref. [13].

Although the preferred emission of the singlet electron pair in a one-photon double ionization process has not been experimentally observed to the best of our knowledge, the preference has been experimentally observed in the electron impact ionization processes of excited He [24,25] and alkali-metal atoms [26,27]. As mentioned in section 2.1.1.1, the electron impact ionization is similar to the one-photon double ionization when the excess photon energy is small. In these works, the ionization rate when the polarizations of the atoms and the electrons were antiparallel ($N_{\uparrow\downarrow}$) and the one when the polarizations were parallel ($N_{\uparrow\uparrow}$) were measured. Then, the spin asymmetry A was calculated as

$$A = \frac{1}{P_e P_a} \times \frac{N_{\uparrow\downarrow} - N_{\uparrow\uparrow}}{N_{\uparrow\downarrow} + N_{\uparrow\uparrow}}, \tag{2-10}$$

where P_e and P_a are the polarizations of the electron beam and the atomic beam, respectively. Because the spin part of the two-electron wave function in the singlet state is written as

$$\phi = \frac{1}{\sqrt{2}}\big(\alpha(1)\beta(2) - \beta(1)\alpha(2)\big), \tag{2-11}$$

and the two-electron wave function in the triplet state is written with the combination of

$$\phi_{m_s=+1} = \alpha(1)\alpha(2), \tag{2-12}$$

$$\phi_{m_s=0} = \frac{1}{\sqrt{2}}\big(\alpha(1)\beta(2) + \beta(1)\alpha(2)\big), \tag{2-13}$$

and

$$\phi_{m_s=-1} = \beta(1)\beta(2), \tag{2-14}$$

the ionization rates, $N_{\uparrow\downarrow}$ and $N_{\uparrow\uparrow}$, are written as

$$N_{\uparrow\downarrow} \propto \sigma_s + \sigma_t \tag{2-15}$$

and

$$N_{\uparrow\uparrow} \propto \sigma_t + \sigma_t, \tag{2-16}$$

where σ_s and σ_t are the singlet and the triplet components of the total ionization cross section, respectively. Therefore, Eq. (2-10) is rewritten as

$$A = \frac{\sigma_s - \sigma_t}{\sigma_s + 3\sigma_t}. \tag{2-17}$$

Eq. (2-17) indicates that $A = 1$ for the pure singlet ionization, $A = -1/3$ for the pure triplet ionization, and $A = +1/3$ when the singlet and the triplet ionization cross sections are the same *i.e.* $\sigma_s = 3\sigma_t$. Figure 2-7 shows the incidence electron energy dependence of the asymmetry, and A is larger than +1/3 when the incident energy is lower than ~15 eV for He and ~20 eV for Li, which means that the creation of the singlet electron pair was preferred in these lower energy regions.

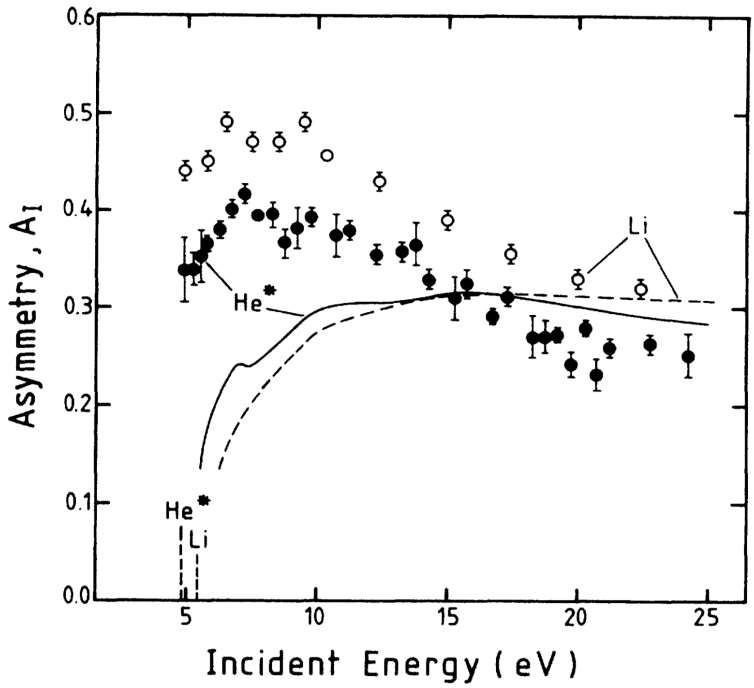

Figure 2-7 Incident energy dependence of the asymmetry (A_I) of the electron pair created in an electron impact ionization. Black dots are the A_I of excited He measured in [25], and white dots are the A_I of Li measured in [27]. Filled curve is the theoretically calculated A_I of excited He, and the dashed curve is the theoretically calculated A_I of Li [42]. The figure is adopted from ref. [25].

2.1.1.3. Three-Photon Sequential Double Ionization

The deviation of the population distribution has been also reported in a three-photon sequential double ionization process of Ar induced by an intense extreme ultraviolet free-electron laser [6-8,28,29]. This process takes three steps to form Ar^{2+} as shown in Fig. 2-8. In the first step, Ar is singly ionized and Ar^+ in the $3p^5\ ^2P_{1/2,\,3/2}$ level is created:

$$\mathrm{Ar}(3p^6,\ ^1S) + h\nu \rightarrow \mathrm{Ar}^+(3p^5,\ ^2P_{1/2,\,3/2}) + \mathrm{e}^-. \tag{2-18}$$

In the second step, Ar^+ is resonantly excited to the $3p^4 3d\ ^2D_{3/2,\,5/2}$ level of Ar^+*:

$$\mathrm{Ar}^+(3p^5,\ ^2P_{1/2,\,3/2}) + h\nu \rightarrow \mathrm{Ar}^+{}^*(3p^4 3d,\ ^2D_{3/2,\,5/2}), \tag{2-19}$$

and finally, the third photon singly ionizes Ar^+*:

$$\mathrm{Ar}^+{}^*(3p^4 3d,\ ^2D_{3/2,\,5/2}) + h\nu \rightarrow \mathrm{Ar}^{2+}(3p^4,\ ^3P \text{ or } ^1D \text{ or } ^1S) + \mathrm{e}^-. \tag{2-20}$$

Hikosaka et al. [6] reported that the population distribution of the created Ar^{2+} states varied as the photon energy changed from 21.0 to 21.4 eV as shown in Fig. 2-9. The mechanism of the variation was explained as follows: The precursors of Ar^{2+} in the ^3P and ^1S states are Ar^+* in the $^2D_{3/2,\,5/2}$

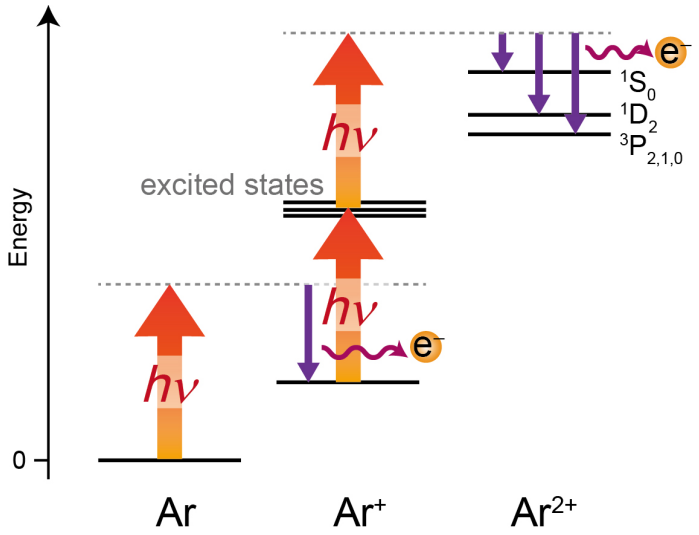

Figure 2-8 Schematic of the three-photon sequential double ionization process of Ar. Ar^+ in the $3s^2 3p^5\ ^2P_{3/2,1/2}$ levels are resonantly ionized by the absorption of additional two photons via the intermediate resonances of Ar^+. It was found that the population distribution in the resultant $3s^2 3p^4\ ^3P$, ^1D, and ^1S states of Ar^{2+} is significantly influenced by the choice of the intermediate resonance of Ar^+. See the text for more detail.

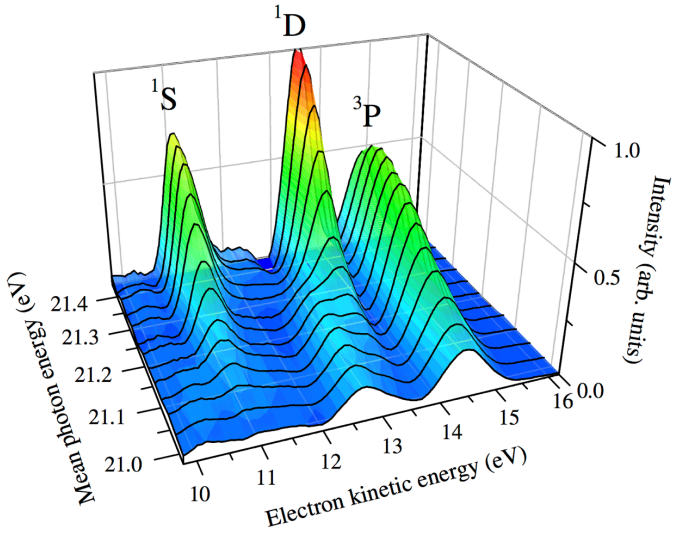

Figure 2-9 Photon energy dependence of the population distribution of Ar^{2+} created through the three-photon sequential double ionization. Depending on the photon energy, Ar^+* in the $^2P_{1/2,3/2}$ levels or $^2D_{3/2,5/2}$ levels are created. Because the precursor of Ar^{2+} in the ^3P and ^1S states are Ar^+* in the $^2D_{3/2,\ 5/2}$ levels, and the precursors of Ar^{2+} in the ^1D state are Ar^+* in the $^2P_{1/2,\ 3/2}$ levels, the population distribution of Ar^{2+} varies depending on the photon energy. The figure is adopted from ref. [43].

levels, whereas the precursors of Ar^{2+} in the ^1D state are Ar^{+}* in the $^2P_{1/2,\ 3/2}$ levels. Because the resonance energies of the transitions $^2P_{1/2} \rightarrow {}^2D_{3/2}$, $^2P_{3/2} \rightarrow {}^2D_{5/2}$, $^2P_{1/2} \rightarrow {}^2P_{3/2}$, and $^2P_{1/2} \rightarrow {}^2P_{1/2}$ are 21.251, 21.367, 21.447, and 21.498 eV, the cross sections of the creation of Ar^{2+} in the ^3P and ^1S states increase when the photon energy is around 21.31 eV, and that of the creation of Ar^{2+} in the ^1D state increases when the photon energy is around 21.47 eV.

Miyauchi et al. [7] also observed the variation of the population distribution when they changed the photon energy from 21.4 to 24.6 eV, and they theoretically showed that the mixing ratio of the $3p^4$ core configuration of the intermediate Ar^{+}* ($3p^4 3d$) is an important factor in deciding the resultant Ar^{2+} state.

The three-photon sequential double ionization of Ar has been also investigated by angle-resolved photoelectron spectroscopy [8,28]. The experimentally observed angular distribution of the electrons emitted in the double ionization process was reproduced by the theoretically calculated angular distribution only when the resonant excitation to the $3p^3 n_1 l_1 n_2 l_2$ autoionizing state of Ar^{+} is considered, which indicates that the third step of the ionization proceeds as:

$$Ar^{+}*(3p^4 3d,\ ^2D_{3/2,\ 5/2}) + h\nu \rightarrow Ar^{+}**(3p^3 n_1 l_1 n_2 l_2) \rightarrow Ar^{2+}(3p^4,\ ^3P \text{ or } ^1D \text{ or } ^1S) + e^{-}, \quad (2\text{-}21)$$

instead of Eq. (2-20).

Although there is no correlation between the emitted electrons in the three-photon sequential double ionization process because the electrons are emitted one-by-one, these studies showed that the electron configuration of the resonantly created intermediate state largely affects the population distribution of the resultant doubly ionized states.

2.1.2. Purpose of This Study

As described in section 2.1.1, the deviations of the population distribution of the resultant doubly ionized states from the statistical weight have been reported in simultaneous two-electron emission processes and in a sequential double ionization process via an intermediate state (Fig. 2-10). However, the population distribution has not been investigated in a simultaneous two-electron emission process via an intermediate state. In such an ionization process, the correlation between the emitted electrons might induce a deviation of the population distribution, and the distribution might also be affected by the electron configuration of the intermediate state.

In the present study, we induced resonantly enhanced two-photon double photoionization processes of Ar and Kr by using high-order harmonics of near-infrared laser pulses, and we investigated the population distributions of Ar^{2+} and Kr^{2+}. They were found to be largely deviated from

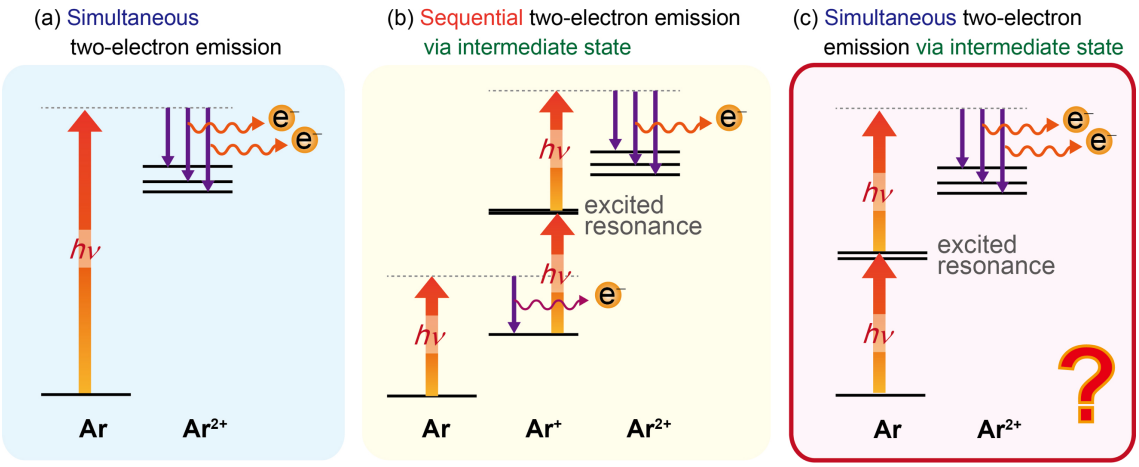

Figure 2-10 (a) Simultaneous two-electron emission process, (b) sequential two-electron emission process via an intermediate state, and (c) simultaneous two-electron emission process via an intermediate state. The deviations of the population distribution of Ar^{2+} from the statistical weights have been reported in (a) and (b), but there have been no reports on the population distribution in (c).

the statistical distributions, indeed, only one of the energetically allowed states was prepared exclusively. On the basis of this finding, we examine the role of the intermediate resonant states of Ar and Kr in determining the population distribution of the resultant Ar^{2+} and Kr^{2+}.

2.2. Experimental Setup

The experimental setup consists of a high-order harmonic generation part, a harmonic order selection part, a flat-field type extreme ultra-violet (EUV) spectrometer, and a magnetic-bottle type photoelectron spectrometer. The schematic of the setup is shown in Fig. 2-11, and the detailed descriptions of the setup are provided in the following sections.

2.2.1. High-Order Harmonic Generation

High-order harmonics were generated by focusing Ti:sapphire laser pulses (~10 mJ, ~40 fs, 1 kHz, 795 nm) by a quartz lens (f = 2 m) into a 15 mm-long gas cell with a hole (1.5 mm ϕ) filled with an Ar gas as shown in Fig. 2-12. The Ar gas was introduced into the gas cell through a pulsed valve operated synchronously with the laser pulses.

The spectrum of the generated high-order harmonics was observed by a flat-field type EUV spectrometer [30-32]. The harmonics entered the spectrometer through a narrow slit, and the

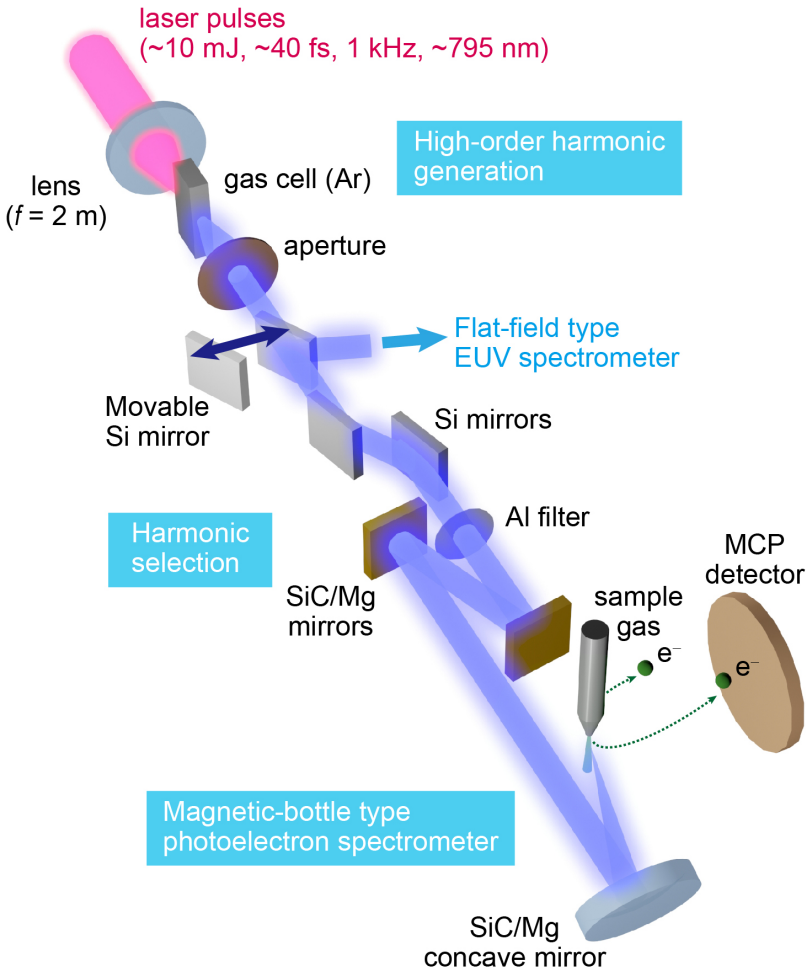

Figure 2-11 Schematic of the experimental setup. The laser pulses are focused into a gas cell filled with Ar gas to generate high-order harmonics. By moving in the movable Si mirror, the generated harmonics are led to a flat-field type EUV spectrometer and the harmonics spectrum is observed. When the movable Si mirror is moved out of the optical path, the orders of the harmonics are selected by Si mirrors, an Al filter, and SiC/Mg multi-layered mirrors. The selected harmonics are focused on sample gas by a SiC/Mg concave mirror. The energies of the emitted electrons are measured by a magnetic-bottle type photoelectron spectrometer.

harmonics were focused by a concave grating onto a multi-channel plate (MCP) detector with a phosphor screen. The image on the phosphor screen was observed by a CCD camera (Andor technology inc.). Because the reflection angle depends on the wavelength of the light pulses, the harmonics are focused on a different position of the detector, therefore, the wavelength of each harmonic can be confirmed from the focused position on the detector. One example of the observed harmonic spectrum is shown in Fig. 2-13. It was confirmed from Fig. 2-13 that the high-order harmonics up to the 29th were generated.

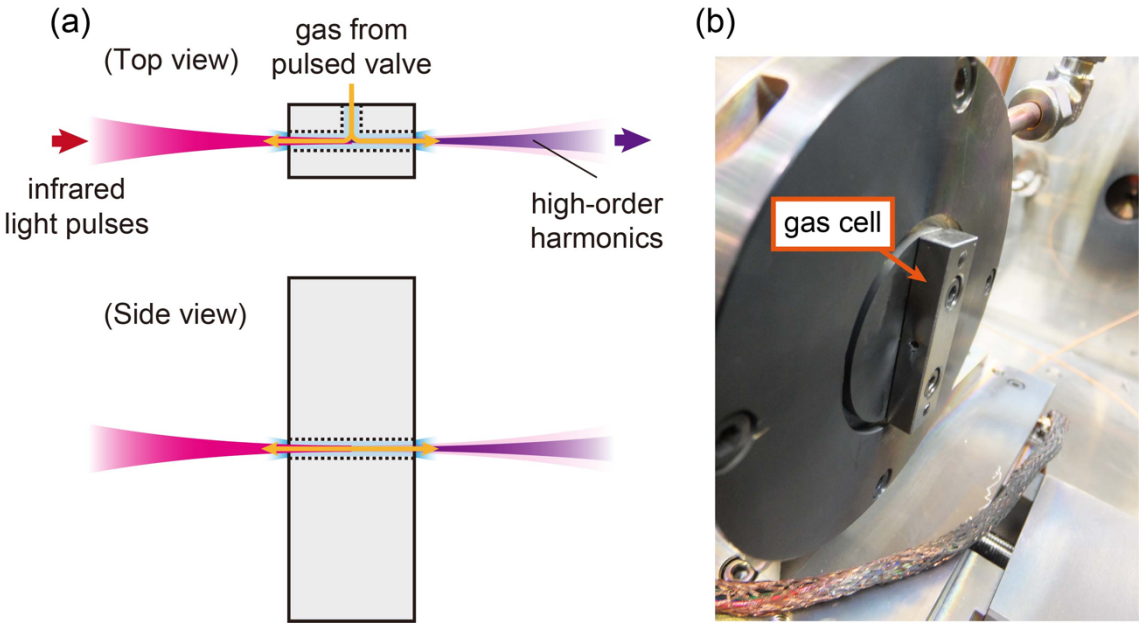

Figure 2-12 (a) Schematic of the gas cell and (b) picture of the gas cell. The gas cell has a T-shaped hole, and the gas is introduced into the hole as shown in (a). The infrared light pulses are focused into the gas cell, and high-order harmonics are generated.

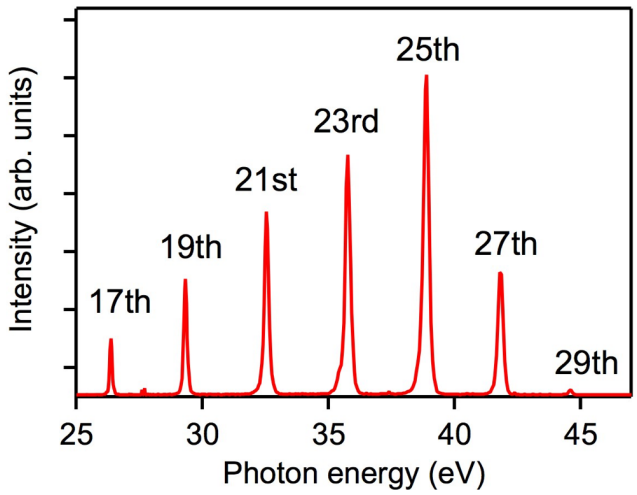

Figure 2-13 Harmonic spectrum observed by using the flat-field type EUV spectrometer. Generation of up to the 29th harmonics were confirmed.

The total intensity of the generated harmonics was measured by a calibrated photodiode (AXU100G, Opto Diode Co.), which was set in front of the EUV spectrometer, and the intensity was ~4 nJ/pulse. Because the intensity of the 23rd harmonic is ~25 % of the total harmonic intensity (Fig. 2-13), the intensity of the 23rd harmonic is ~1 nJ/pulse.

2.2.2. Selection of Harmonics

The generated harmonics passed through two apertures of 6 mm and 3 mm diameters, which block the outer part of the co-propagating fundamental laser beam having the divergence angle larger than that of the harmonics. The harmonics were reflected by two Si mirrors at the Brewster's angle of the fundamental light pulses (~15º) in order to further reduce the intensity of the residual fundamental light pulses. The intensities of the residual fundamental light pulses and the 9th and lower-order harmonics became negligibly small after they passed through an Al filter whose thickness is 200 nm. Fig. 2-14 shows the calculated transmittance of the Al filter [33]. The transmittance is smaller than ~10^{-6} for the fundamental light and the low-order harmonics in the wavelength range longer than 88 nm, while it is larger than 0.6 for the 13th and higher-order harmonics. The 23rd and 25th harmonics were selected by using two SiC/Mg multi-layered mirrors (NTT-AT Co.), having the reflectivities of 3, 5, 49, 19, and 3 % at the incident angle of ~2º for the 19th, 21st, 23rd, 25th, and 27th harmonics, respectively.

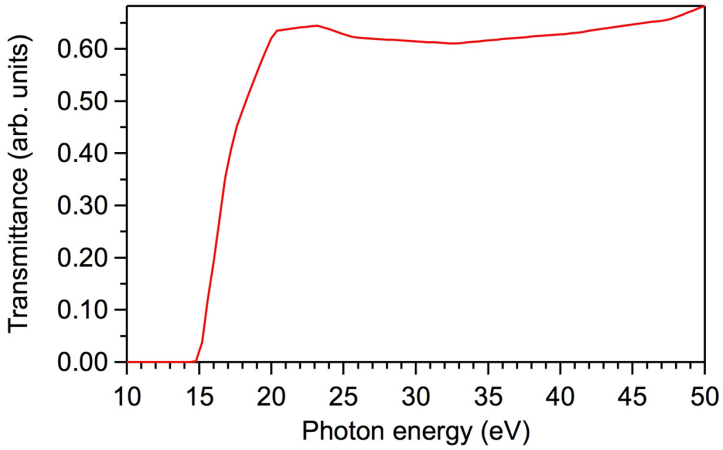

Figure 2-14 Transmittance of an Al filter with the thickness of 200 nm. With this filter, the intensities of the 9th and lower-order harmonics are reduced. The data is from ref. [33].

2.2.3. Photoelectron Spectroscopy by Magnetic-Bottle Type Photoelectron Spectrometer

The selected harmonics propagated ~10 mm below the interaction region in a magnetic-bottle type photoelectron spectrometer (FOM, Netherland) [34] as shown in Fig. 2-15, and were back-focused onto the interaction region by a SiC/Mg multi-layered concave mirror (f = 150 mm, NTT-AT Co.) at the incident angle of ~2º. The total intensity of the harmonics at the interaction region was

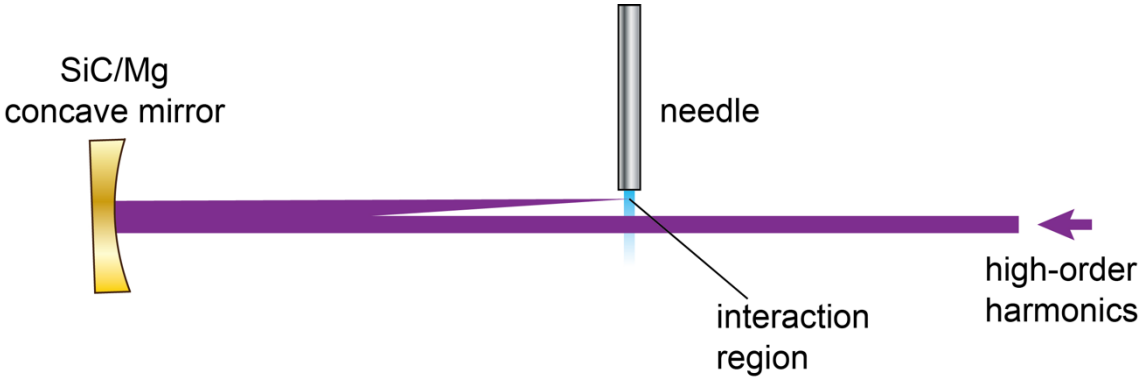

Figure 2-15 Schematic around the interaction region in the magnetic-bottle type photoelectron spectrometer. The high-order harmonics are introduced ~10 mm below the interaction region and they are focused by a SiC/Mg multi-layered concave mirror to the interaction region. The incident angle is ~2º. The tip of the needle is placed ~2 mm above the interaction region, and the gas sample is introduced through the needle. The TOF axis is orthogonal to the sheet plane.

estimated to be in the range of 10^7-10^8 W/cm^2 by taking into account the reflectivities of the mirrors and the transmittance of the filter. The polarization direction of the harmonics was parallel to the time-of-flight (TOF) axis. A sample gas was continuously introduced through a needle whose inner diameter is 70 μm ϕ. The tip of the nozzle needle was placed ~2 mm above the interaction region, and the focused harmonics crossed the sample atomic beam.

The photoelectrons emitted from the sample gas in the interaction region were introduced into the TOF tube through an aperture (2 mm ϕ). The magnetic fields of 1 T and 2 mT are appplied on the interaction region and the drift tube, respectively, which creates a bottle-shaped magnetic field as shown in Fig. 2-16. The electrons move helically in the magnetic field towards an MCP detector (PHOTONIS) placed at the end of the drift tube. Because the relation between the initial angle (θ_i) and the final angle (θ_f) of the electrons with respect to the TOF axis is written by using the magnetic field at the interaction region (B_i) and the magnetic field in the drift region (B_f) as [34]

$$\frac{\sin\theta_f}{\sin\theta_i} = \left(\frac{B_f}{B_i}\right)^{1/2}, \tag{2-22}$$

the electrons emitted with θ_i smaller than 90° has θ_f smaller than 2.56°. This means that even the electrons emitted almost perpendicular to the TOF axis are parallelized in the magnetic field, and therefore can reach the MCP detector. In other words, the magnetic-bottle type photoelectron spectrometer shows a large electron collection angle of 2π steradians.

The signals were recorded by a data acquisition board (TDC8HP, RoentDek GmbH), and when two electrons were detected for one shot of harmonics, they were regarded as simultaneously emitted

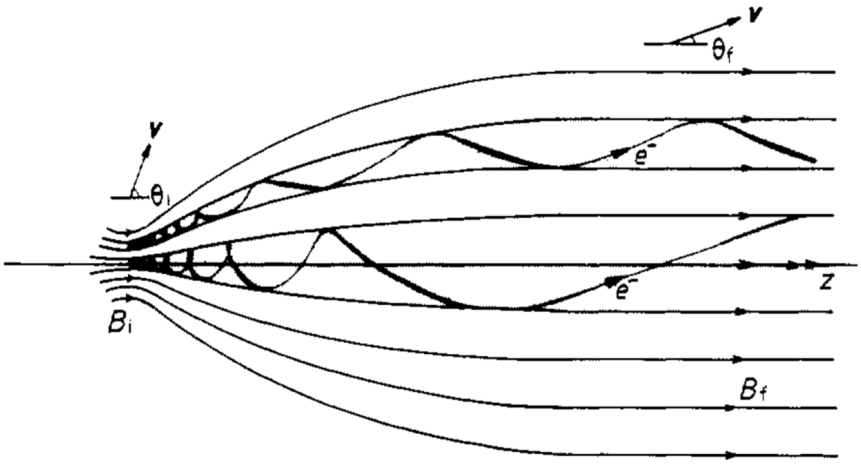

Figure 2-16 Schematic of the magnetic fields created in the magnetic-bottle type photoelectron spectrometer. B_i and B_f are the magnetic fields applied in the interaction region and the drift tube region, respectively. The electrons emitted in the interaction region move helically towards the MCP detector. The initial angle of the electron θ_i is reduced to the final angle θ_f, and the spectrometer shows a high electron collection efficiency. The figure is adopted from ref. [34].

electrons. The signal count rate was kept below 0.3 counts/pulse in order to sufficiently reduce the number of false coincidence events.

The energy axis of the recorded photoelectron spectra was calibrated by the photoelectron peaks originating from the 5*p* electron emissions from Xe induced by the 9th to 13th harmonics and by the 21st to 25th harmonics, such that the energy difference between the $5s^2 5p^5\ ^2P_{3/2}$ and $^2P_{1/2}$ levels of Xe^+ becomes close to 1.3064 eV [35]. The calibrated photoelectron spectrum of Xe is shown in Fig. 2-17. The uncertainties in the calibrated electron kinetic energies were estimated to be ±4 %. The full widths at half-maximum of these peaks in the photoelectron spectra were ~0.7 eV, which can be regarded as the energy resolution of the recorded photoelectron spectra. From the photoelectron spectrum of Xe, it was confirmed that up to the 27th harmonics were selected by the Si and SiC/Mg mirrors, and the intensities of the 23rd and 25th harmonics became two orders of magnitude larger than those of the rest of the harmonics when the Al filter was inserted. The photon energy of the *i*th harmonic ($h\nu_i$) was estimated by calculating

$$h\nu_i = E_e(5p, i) + E(Xe^+, 5s^2 5p^5), \tag{2-23}$$

where $E_e(5p, i)$ is the observed energy of the 5*p* electron emitted in the single ionization induced by the *i*th harmonic, and $E(Xe^+, 5s^2 5p^5)$ is the energy of the created Xe^+ ($5s^2 5p^5$) from the neutral ground state.

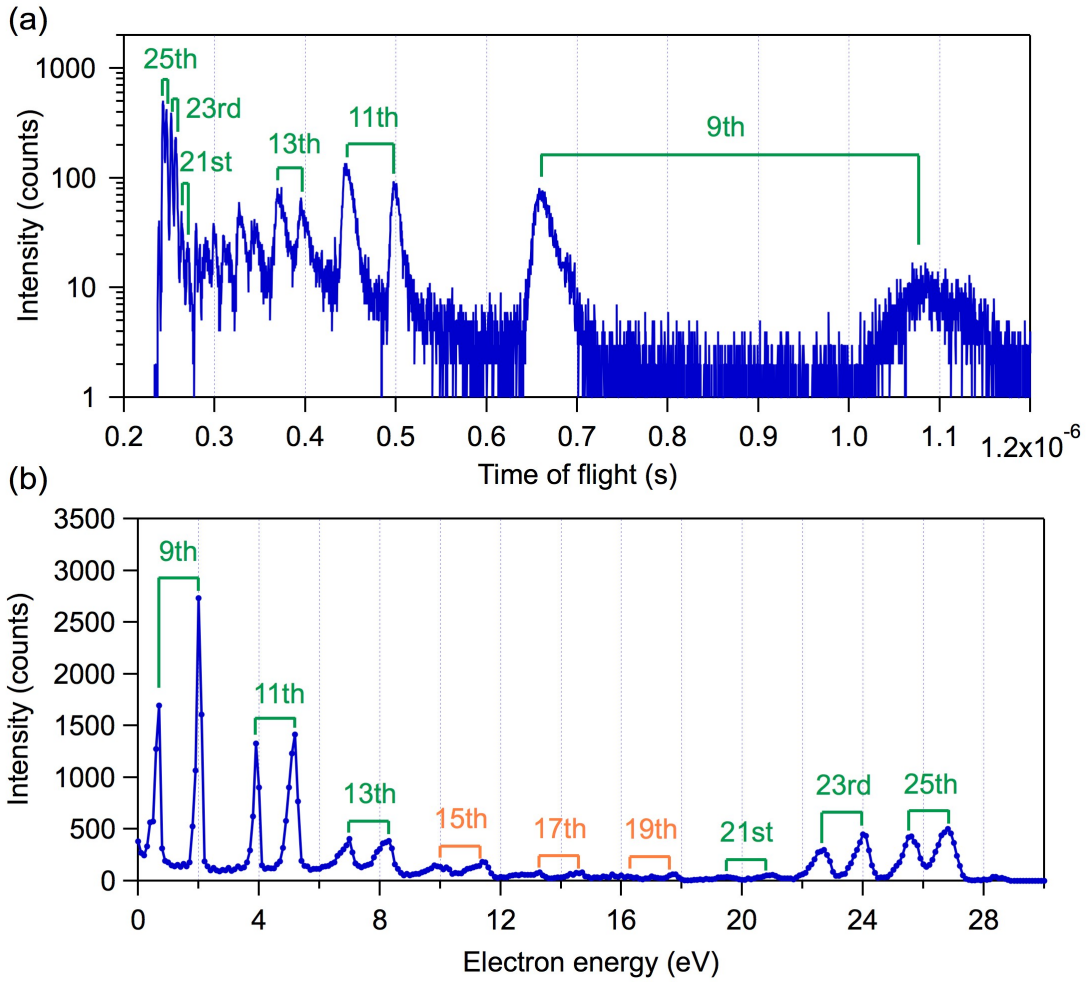

Figure 2-17 Photoelectron spectra of Xe irradiated with high-order harmonics generated in Condition 1. See the text for the definition of Condition 1. The measurement was performed without inserting the Al filter. (a) The time-of-flight of the emitted electrons were measured, and (b) the time-of-flight was converted to photoelectron energy such that the energy difference between the photoelectron peaks assigned to the creation of the $5s^2 5p^5\ ^2P_{3/2}$ and $^2P_{1/2}$ levels of Xe^+ becomes close to 1.3064 eV [35]. The peaks used for the calibration of the energy axis are indicated with green lines.

The photoelectron measurements of Ar were performed with the harmonics generated in two different conditions using the same experimental setup. In one condition, the Ar gas pressure at the harmonics-generation chamber was 2×10^{-2} Pa and the fundamental pulse energy was 10.3 mJ (Condition 1), while in the other condition, the Ar gas pressure at the harmonics-generation chamber was 6×10^{-2} Pa and the fundamental pulse energy was 11.3 mJ (Condition 2). In each condition, the distance between the gratings in the pulse compressor was adjusted so that the total intensities of the harmonics were maximized. The signals were accumulated for 3.3 hours in Condition 1 and for 8.3 hours in Condition 2. The coincidence photoelectron measurement of the double ionization of Kr was performed using the harmonics generated in Condition 1, and the accumulation time was 0.5 hours.

2.3. Results and Discussion

2.3.1. Relative Intensities of Harmonics

Figure 2-18 shows the observed photoelectron spectra of Ar. The 23rd and 25th harmonics induced one-photon single ionization of Ar through which one 3*p* electron is emitted, and two peaks originating from these processes were observed in the photoelectron spectra in the region between 18 and 25 eV in both cases when the harmonics were generated in Condition 1 (Fig. 2-18(c)) and in Condition 2 (Fig. 2-18(d)). The spin-orbit splitting of the $3s^2 3p^5\ ^2P_{3/2,1/2}$ levels was not resolved because the energy separation of 0.18 eV [35] was smaller than the energy resolution (~0.7 eV) of the measurements. The peak at 20.3 eV in Condition 1 (Fig. 2-18(c)) and the peak at 19.8 eV in Condition 2 (Fig. 2-18(d)) were assigned to the emission of a 3*p* electron induced by the 23rd harmonic, and the peak at 23.3 eV in Condition 1 and the peak at 22.8 eV in Condition 2 were assigned to the emission

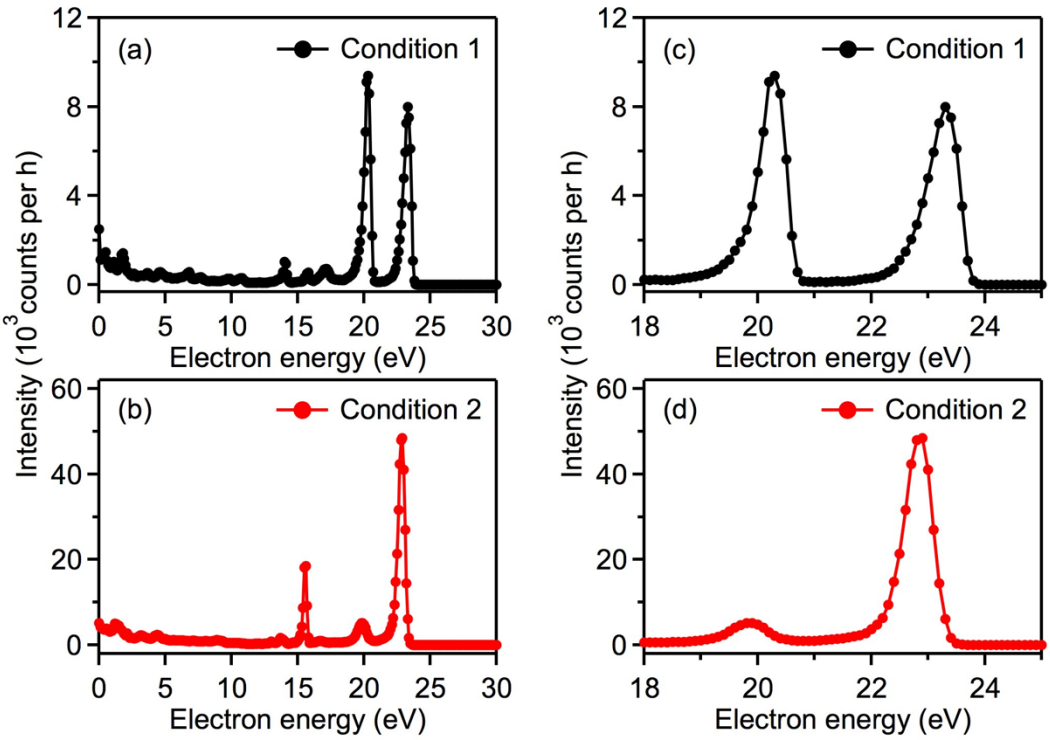

Figure 2-18 Photoelectron spectra of Ar observed (a,b) in the energy region of 0 to 30 eV and (c,d) in the energy region of 18 to 25 eV. The lower energy peak in (c) and (d) are assigned to the 3*p* electron emission induced by the 23rd harmonic, and the higher energy peak in (c) and (d) are assigned to the 3*p* electron emission induced by the 25th harmonic. The peaks observed around 15 eV in (a) and (b) are the ringing signals of the peaks observed in (c) and (d). The photoelectron spectra in (c) and (d) are adopted from ref. [1].

of a 3*p* electron induced by the 25th harmonic. The peak energies in Condition 2 were smaller by ~0.5 eV than those in Condition 1 because the fundamental laser pulses were more positively chirped in Condition 2 than in Condition 1, and consequently, the harmonics were red-shifted. Although the photoelectron spectra in the energy region lower than 18 eV showed peaks assigned to the 3*p* electron emissions induced by the 11th to 21st harmonics and the 3*s* electron emissions induced by the 19th to 25th harmonics (Figs. 2-18(a) and 18(b)), they were about two orders of magnitude less intense than the peaks observed in Figs. 2-18(c) and 18(d).

The relative integrated intensity of the photoelectron peak associated with the creation of the $3s^2 3p^5\ ^2P$ state of Ar^+ by the 23rd harmonic to the corresponding peak produced by the 25th harmonic was 1.1 in Condition 1 while it was 0.16 in Condition 2. Because the relative cross section of the 3*p* electron emission induced by the 23rd harmonic to the 3*p* electron emission induced by the 25th harmonic is ~1.8 [36] as shown in Fig. 2-19, the relative intensities of the 23rd harmonic to the 25th harmonic were estimated to be 0.6 in Condition 1 and 0.09 in Condition 2.

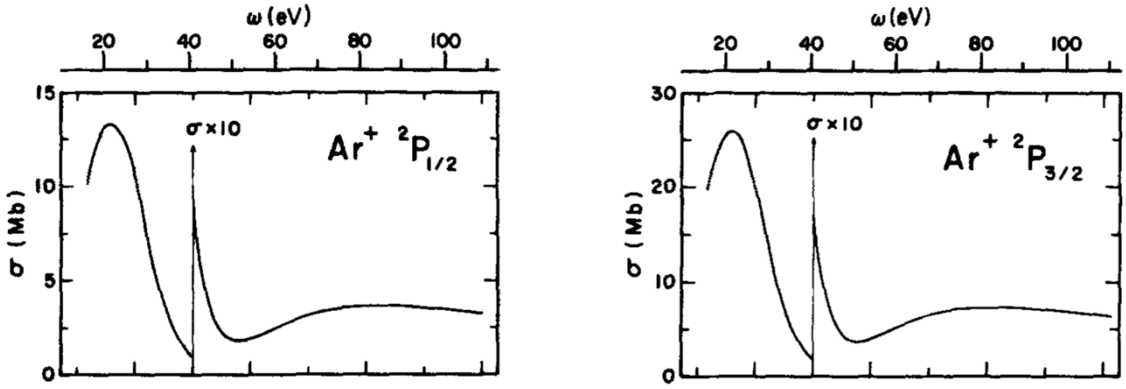

Figure 2-19 Photon energy (ω) dependences of the cross sections (σ) of the single photoionization of Ar in which Ar^+ is created in the $^2P_{1/2}$ level (left) and in the $^2P_{3/2}$ level (right). The figures are adopted from ref. [36].

2.3.2. Two-Photon Double Ionization Process

Correlation maps of the energies of the slower electrons (E_{slow}) and the faster electrons (E_{fast}) are plotted for Condition 1, in which the intensities of the 23rd and 25th harmonics are comparable (Fig. 2-20(a)), and for Condition 2, in which the intensity of the 25th harmonic dominates (Fig. 2-20(b)). Fig. 2-20(a) exhibits two lines whose slope is −1.0, and Fig. 2-20(b) exhibits one line whose slope is −1.0. These lines indicate that the excess photon energies for double ionizations are distributed

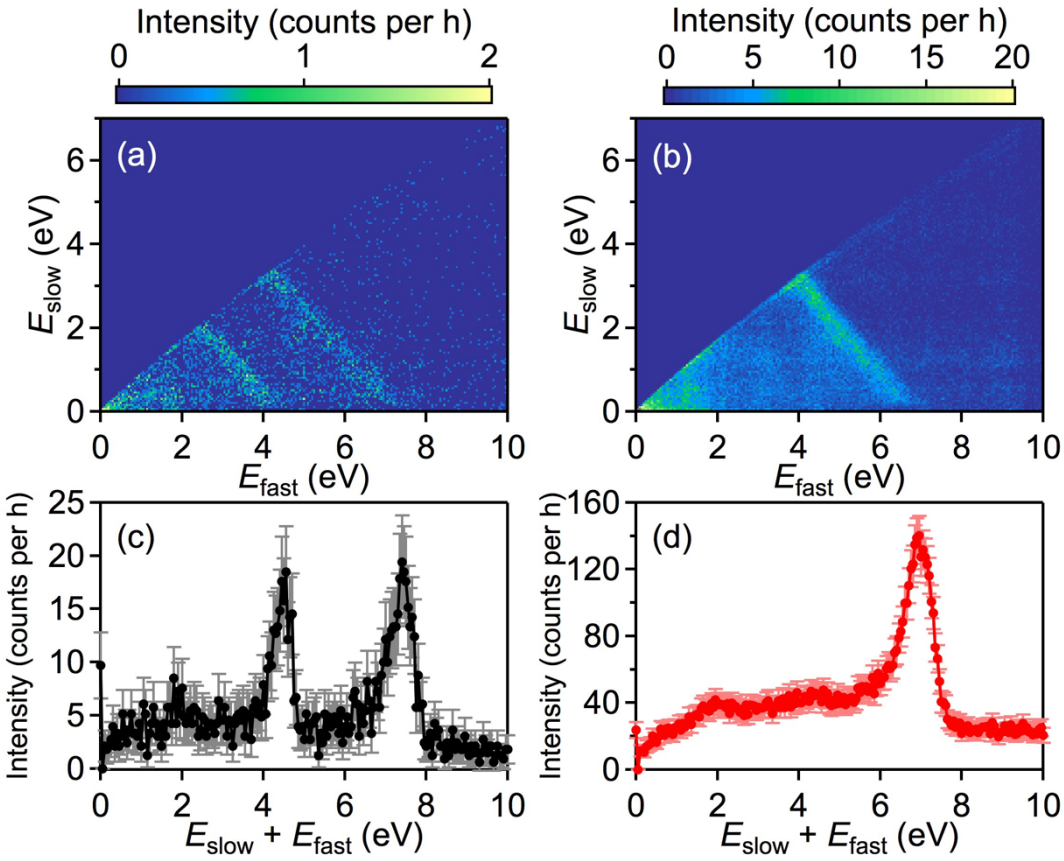

Figure 2-20 (a,b) Correlation maps of the energies of the slower and faster electrons emitted from Ar and (c,d) the distributions of the total energies of the coincidently detected faster and slower electrons. (a) and (c) are obtained when Ar is irradiated with harmonics generated in Condition 1. (b) and (d) are obtained when Ar is irradiated with harmonics generated in Condition 2. Coincidence signals were not detected in (a) and (b) when the energies of the slower and faster electrons are close because the data acquisition board could not separate the time-of-flight of these signals. The peaks observed in (c) and (d) correspond to the lines with the slope of −1.0 observed in (a) and (b), respectively. The figure is adopted from ref. [1].

between two emitted electrons, therefore the two electrons are emitted simultaneously. The excess photon energies in these processes appear as the peaks in the distribution of the total kinetic energies of the slower and faster electrons detected in coincidence (Figs. 20(c) and 20(d)). Figure 2-20(c) shows that the excess photon energies are 4.48 and 7.42 eV in Condition 1, and Fig. 2-20(d) shows that the excess photon energy was 6.94 eV in Condition 2.

The distributions of the total kinetic energies in Figs. 2-20(c) and 20(d) look very similar to the photoelectron spectra in Figs. 2-18(c) and 18(d), respectively. The similarity indicates that the 23rd harmonic contributes to the simultaneous two-electron emission process with the excess energy of 4.48 eV observed in Condition 1 (Process I), and the 25th harmonic contributes to the processes with the excess energy of 7.42 eV in Condition 1 and 6.94 eV in Condition 2 (Process II). These processes

are multi-photon processes because the double ionization threshold energy of Ar (43.39 eV [35]) is higher than the photon energies of the 23rd and 25th harmonics. Because the energy difference between the two peaks observed in Fig. 2-20(c) corresponded to the energy difference between the 23rd and 25th harmonics, the additional photon energy should be common in these processes. The energy of the additional photon is expected to be in resonance with the energy of an excited state of Ar because a multi-photon process can be realized only when there is resonance enhancement at the weak intensities of the harmonics (10^7-10^8 W/cm^2), which is four orders of magnitude weaker than the intensities in the previous studies on the two-photon non-resonant double ionization processes of Ar [37,38].

The sum of the energy of the additional photon in resonance with an excited state of Ar, E_{res} and the photon energy of the high order harmonic is equal to the sum of the energy of the resultant state of Ar^{2+}, $E(Ar^{2+})$ and the total kinetic energy of the two electrons E_{2e} (= E_{slow} and E_{fast}) ejected upon the double ionization, that is,

$$E_{res} + h\nu(23rd) = E(Ar^{2+}) + E_{2e}(I) \quad (2\text{-}24)$$

holds for Process I, where $h\nu$(23th) denotes the photon energy of the 23rd harmonic, and

$$E_{res} + h\nu(25th) = E(Ar^{2+}) + E_{2e}(II) \quad (2\text{-}25)$$

holds for Process II, where $h\nu$(25th) denotes the photon energy of the 25th harmonic. It was found that these two equations are fulfilled when E_{res} corresponds to the photon energy of the 19th harmonic (29.2 eV in Condition 1 and 29.5 eV in Condition 2) with which Ar^{2+} is prepared either in the $3s3p^5$ ^1P state or in the $3s^23p^33d$ ^5D state of Ar^{2+} (Table 2-2).

Table 2-2 Derivation of E_{res} for each double ionization process of Ar.

Ar^{2+} state	$E(Ar^{2+})$ (eV)[a]	Condition	$h\nu$ (eV)[b]	E_{2e} (eV)	E_{res} (eV)[c]
^1P ($3s3p^5$)	61.25	1	36.1	4.48	29.6
			39.1	7.42	29.6
		2	38.6	6.94	29.6
^5D ($3s^23p^33d$)	61.35	1	36.1	4.48	29.7
			39.1	7.42	29.7
		2	38.6	6.94	29.7

[a]Reference [35].
[b]Energies derived from Fig. 2-18 assuming that the first ionization potential of Ar is 15.8 eV [35]. The photon energies of 36.1 and 39.1 eV correspond respectively to the photon energies of the 23rd and 25th harmonics generated in Condition 1, and the photon energy of 38.6 eV corresponds to the photon energy of the 25th harmonic generated in Condition 2.
[c]Derived from Eqs. (2-24) and (2-25).

It was also found that the photon energy of the 19th harmonic coincides with the $3s3p^6np$ ($n \sim 25$) Rydberg states of Ar, which converge to the $3s3p^6\ ^2S_{1/2}$ level of Ar^+ (29.24 eV) [35], therefore, the 19th harmonic can contribute to the ionization process even though its intensity is much weaker than the intensities of the 23rd and 25th harmonics, and the two-photon process is realized.

The $3s3p^6np$ Rydberg states of Ar are considered to be in the ^1P states so that it is accessed from the ground ^1S state of Ar by one-photon absorption. The mixing with other configurations is known to be negligible [39]. As for Ar^{2+}, as long as the total spin angular momentum in the double ionization process is conserved, the ^5D state of Ar^{2+} could not be created. Therefore, as shown in Fig. 2-21, it is highly probable that the double ionization is resonantly enhanced and proceeds as

$$Ar(3s^23p^6,\ ^1S) + h\nu(19\text{th}) \rightarrow Ar^*(3s3p^6np,\ ^1P), \tag{2-26}$$

$$Ar^*(3s3p^6np,\ ^1P) + h\nu(23\text{rd or } 25\text{th}) \rightarrow Ar^{2+}(3s3p^5,\ ^1P) + 2e^-. \tag{2-27}$$

Although the total photon energies of 19th + 23rd and 19th + 25th harmonics are sufficiently high for the creation of the other lower lying states of Ar^{2+} (See Fig. 2-21), no other lines with a slope of −1.0 can be identified in the higher energy region of the correlation maps shown in Figs. 2-26(a) and 26(b) in Appendix. As explained in section 2.1, some deviations from the statistical population

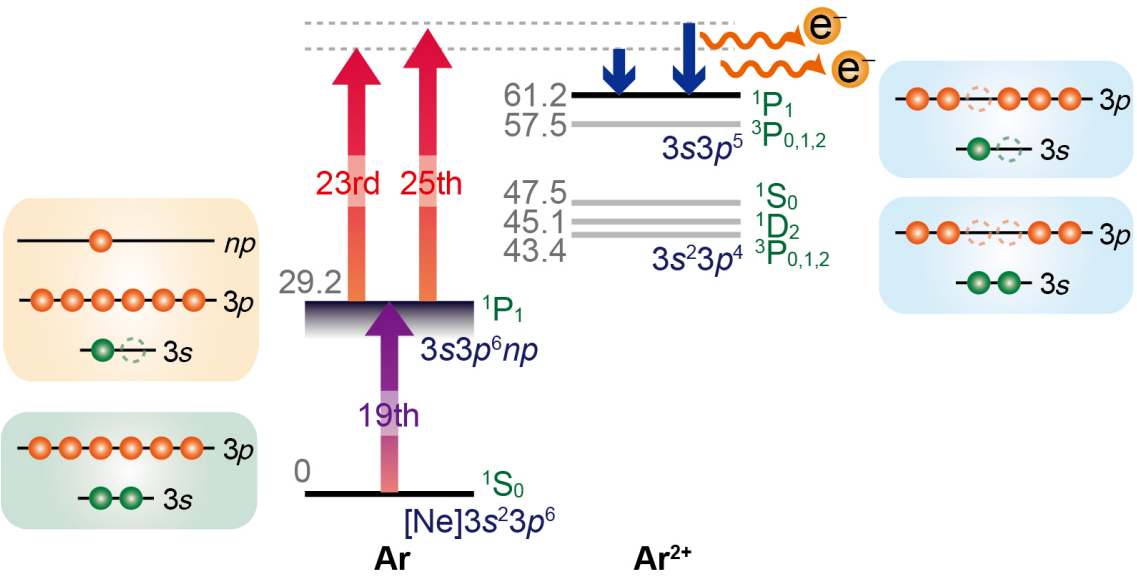

Figure 2-21 Schematic of the two-photon double ionization process of Ar. The 19th harmonic excites Ar to the Rydberg states, and the 23rd or 25th harmonic induces a simultaneous two electron emission to create the $3s3p^5\ ^1P_1$ level of Ar^{2+}. The energies from the ground state of Ar to the $3s^23p^4\ ^3P_2$, $^1D_2$, $^1S_0$ levels and the $3s3p^5\ ^3P_2$, $^1P_1$ levels of Ar^{2+} and the $3s3p^6\ ^2S_{1/2}$ level of Ar^+ are shown in the unit of eV. Part of the figure is adopted from ref. [1].

distribution of the resultant electronic states of doubly charged atoms upon the double photoionization have been reported before [3-8,20,28,29]. Unlike these reported processes, the observed process showed the exclusive preparation of doubly charged atoms in only one single electronic state.

2.3.3. Anomalous Selectivity

In the ionization of the excited Ar ($3s3p^6np$ ($n \sim 25$)) to Ar^{2+} ($3s3p^5$), one np and one of the $3p$ electrons are emitted (Fig. 2-22). On the other hand, in the ionization of the excited Ar to Ar^{2+} ($3s^23p^4$), one of the $3p$ electrons relaxes to the $3s$ orbital in addition to the emissions of the np and $3p$ electrons. The selective creation of Ar^{2+} ($3s3p^5$) suggests that the double ionization proceeds with the minimum changes in the electron configuration from that of the resonance intermediate state. The changes in the electron configuration in the single photoionization process is discussed by using Dyson norm [40], which is defined as the overlap integral between the wave functions of the initial and singly ionized states. It has been known that the Dyson norm becomes large when the core electron configuration is kept during the ionization. Because the single ionization probability is proportional to the Dyson norm,

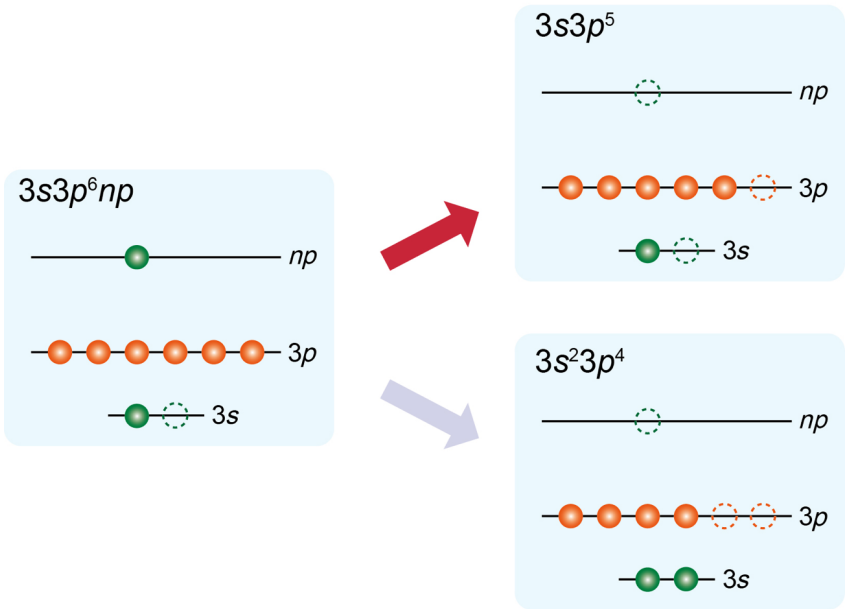

Figure 2-22 Electron configurations of the intermediate Ar* ($3s3p^6np$) and Ar^{2+} ($3s3p^5$ or $3s^23p^4$). In the creation of Ar^{2+} ($3s3p^5$), one np and one of the $3p$ electrons are emitted. On the other hand, in the creation of Ar^{2+} ($3s^23p^4$), one of the $3p$ electrons relaxes to the hole in the $3s$ orbital in addition to the emission of the np and $3p$ electrons.

the dominant ionization process has the minimum electron configuration changes. Our observation indicates that this propensity of the minimum configuration change in single ionization processes can also be applied to the double ionization from the $3s3p^6np$ ($n \sim 25$) excited Ar.

Within the *LS* scheme, the total spin angular momentum of Ar is conserved through the double ionization process as

$$\mathbf{S}_{int} = \mathbf{S}_{ion} + \mathbf{S}_{e\text{-}e}, \tag{2-28}$$

where $\mathbf{S}_{int}$, $\mathbf{S}_{ion}$, and $\mathbf{S}_{e\text{-}e}$ are the spin angular momenta of the intermediate excited state, the doubly ionized state, and the electron pair, respectively. Because both the intermediate excited Ar and the created Ar^{2+} are in the singlet states, which means $S_{int} = S_{ion} = 0$, the emitted electron pair should be in the singlet state, that is, $S_{e\text{-}e} = 0$.

The observed two-electron emissions are achieved by the one-photon excitation of the excited Ar ($3s3p^6np$), in which one electron is promoted to the outermost orbital (Fig. 2-23). One-photon double ionizations of atoms having this type of configuration such as excited He ($1s2s$) [9-12], ground-state Li ($1s^22s$) [13,14], and excited Be ($1s^22s2p$) [15] have been theoretically studied as described in section 2.1.1.2. In these studies, the cross section of the emission of a triplet electron pair is always

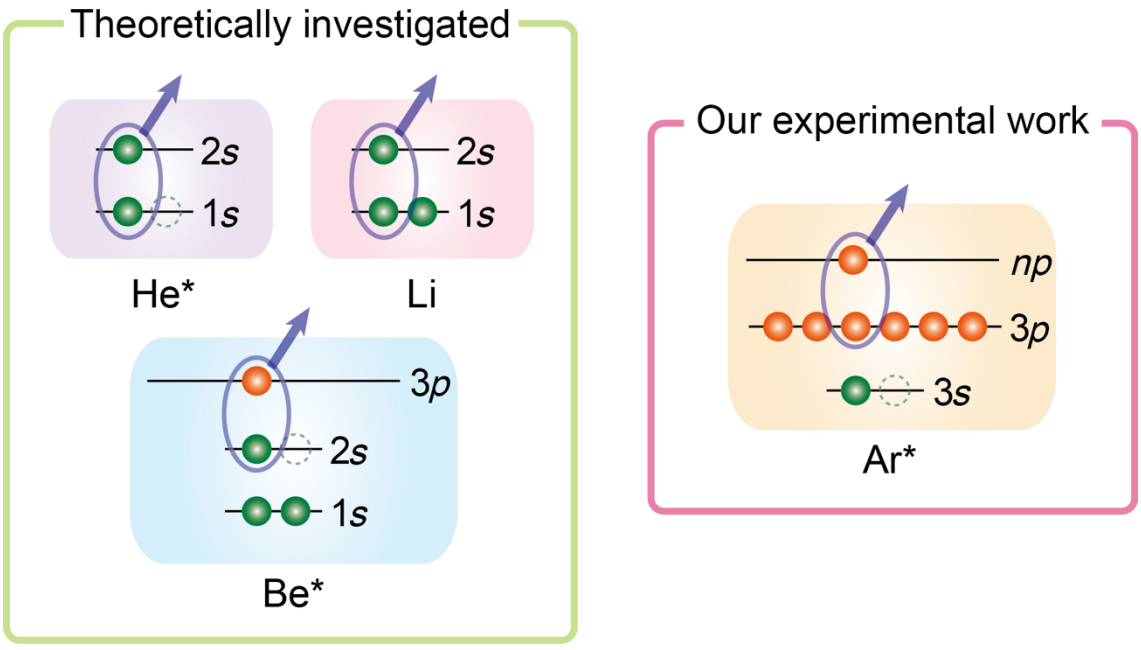

Figure 2-23 Electron configurations of the excited He ($1s2s$), ground-state Li ($1s^22s$), excited Be ($1s^22s2p$), and excited Ar ($3s3p^6np$). The spin states of the electron pairs emitted in the one-photon double ionization of He*, Li, and Be* have been theoretically investigated, and all of these studies showed a preference in the singlet electron pair emission. In our work, we experimentally observed a selective emission of the singlet electron pair from Ar*.

smaller than the cross section of the emission of a singlet electron pair, and this propensity for the emission of the singlet pair was interpreted by the Pauli's exclusion principle explaining the smaller correlation between the electrons in a triplet pair. Our observation showed that the singlet electron pair emission occurs exclusively in the one-photon double ionization of the excited Ar ($3s3p^6np$). It seems that the emitted electron pair tends to be in the singlet state in the one-photon double ionization of atoms having the configuration in which one electron is in the outermost orbital (Fig. 2-23).

2.3.4. Double Ionization of Kr

In a similar manner introduced above for the double ionization of Ar, we investigated the double ionization of Kr induced by the irradiation of the high-order harmonics of near-infrared laser pulses generated in Condition 1. In Condition 1, the intensities of the 23rd and 25th harmonics were comparable, and two lines exhibiting a slope of −1.0 are observed in the correlation map below 15 eV as shown in Fig. 2-24(a). No other lines were observed in the higher energy region. The sum of the energies of the simultaneously emitted electrons were 7.57 eV and 10.58 eV as seen in Fig. 2-24 (b), which indicate that the excess energy is 7.57 eV when the 23rd harmonic contributes to the simultaneous two-electron emission process (Process I') and the excess energy is 10.58 eV when the 25th harmonic contributes to the emission process (Process II').

From the energy conservation, in a similar manner as in the case of Ar,

$$E_{\mathrm{res}} + h\nu(23\mathrm{rd}) = E(\mathrm{Kr}^{2+}) + E_{2\mathrm{e}}(\mathrm{I}') \tag{2-29}$$

holds for Process I', and

$$E_{\mathrm{res}} + h\nu(25\mathrm{th}) = E(\mathrm{Kr}^{2+}) + E_{2\mathrm{e}}(\mathrm{II}') \tag{2-30}$$

holds for Process II'. The photon energies, $h\nu$(23rd) and $h\nu$(25th), are those derived from the photoelectron spectrum of Ar in Fig. 2-18(c). It was found that these two equations are approximately fulfilled (i) when E_{res} corresponds to the photon energy of the 9th harmonic (14.1 eV in Condition 1) and the $4s^24p^4\ ^1S$ state of Kr^{2+} is prepared or (ii) when E_{res} corresponds to the photon energy of the 17th harmonic (26.6 eV in Condition 1) and the $4s4p^5\ ^1P$ state or the $4s^24p^34d\ ^5D$ state of Kr^{2+} is prepared (Table 2-3).

It is also found that (i) the photon energy of the 9th harmonic coincides with the $4s^24p^5nd$ ($n \sim 20$) Rydberg states of Kr and (ii) the photon energy of the 17th harmonic coincides with the $4s4p^6np$ ($n \sim 7$) Rydberg states of Kr converging to the $4s4p^6\ ^2S_{1/2}$ state of Kr^+ (27.5 eV) [35].

Table 2-3 Derivation of E_{res} for each double ionization process of Kr.

Kr^{2+} state	$E(Kr^{2+})$ (eV)[a]	$h\nu$ (eV)[b]	E_{2e} (eV)	E_{res} (eV)[c]
^1S ($4s^24p^4$)	42.46	36.1	7.57	13.9
		39.1	10.58	13.9
^5D ($4s^24p^34d$)	55.54	36.1	7.57	27.0
		39.1	10.58	27.0
^1P ($4s4p^5$)	55.95	36.1	7.57	27.4
		39.1	10.58	27.4

[a]Reference [35].
[b]Energies derived from Fig. 2-18 assuming that the first ionization potential of Ar is 15.8 eV [35]. The photon energies of 36.1 and 39.1 eV correspond respectively to the photon energies of the 23rd and 25th harmonics generated in Condition 1.
[c]Derived from Eqs. (2-29) and (2-30).

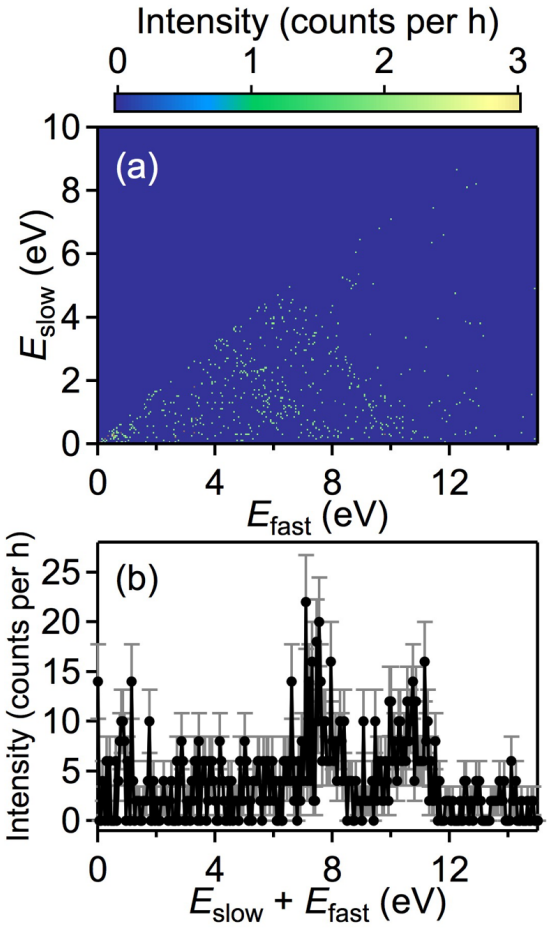

Figure 2-24 (a) Correlation map of the energies of the two electrons ejected from Kr and (b) the total energy distribution of the correlated electrons. The spectrum was observed by the irradiation of the harmonics generated in Condition 1. Similar to the correlation maps of the energies of the electrons emitted in the two-photon double ionization of Ar, two diagonal-line shaped structures were observed in (a). The figure is adopted from ref. [1].

However, in the current experimental conditions, the intensity of the 9th harmonic at the interaction point is estimated to be smaller than the intensity of the 17th harmonic by one order of magnitude. Therefore, it is more probable that the resonance enhancement is achieved by the 17th harmonic. In addition, as long as the *LS* scheme is assumed, the preparation of the $4s^2 4p^3 4d\ ^5D$ state of Kr^{2+} is less likely because of the conservation of the total spin angular momentum under the *LS* scheme [41].

Therefore, as shown in Fig. 2-25, it is probable that the double ionization of Kr is resonantly enhanced and proceeds as

$$Kr(4s^2 4p^6, {}^1S) + h\nu(17\text{th}) \rightarrow Kr^*(4s4p^6 np, {}^1P), \tag{2-31}$$

$$Kr^*(4s4p^6 np, {}^1P) + h\nu(23\text{rd or } 25\text{th}) \rightarrow Kr^{2+}(4s4p^5, {}^1P) + 2e^-. \tag{2-32}$$

It should be noted that E_{res} = 27.4 eV, obtained from Eq. (2-29) or equivalently from Eq. (2-30), is larger than the photon energy of the 17th harmonic (26.6 eV) by 0.8 eV. Therefore, the resonance is considered to be achieved by the high-energy tail of the 17th harmonic, and the selective preparation of the doubly charged atomic state is realized in Kr by the resonantly enhanced two-photon double ionization in the same way as in Ar.

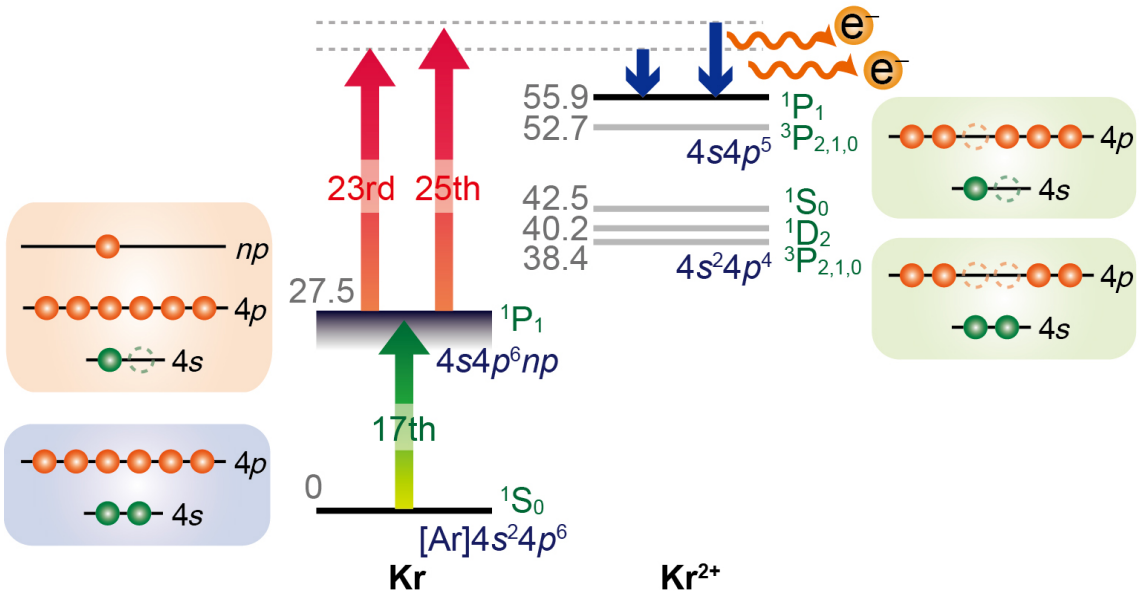

Figure 2-25 Two-photon double ionization process of Kr. The 17th harmonic excites Kr to the Rydberg states, and the 23rd or 25th harmonic induces a simultaneous two electron emission to create the $4s4p^5\ ^1P_1$ level of Kr^{2+}. The energies from the ground state of Kr to the $4s^2 4p^4\ ^3P_2$, $^1D_2$, $^1S_0$ levels and the $4s4p^5\ ^3P_2$, $^1P_1$ levels of Kr^{2+} and the $4s4p^6\ ^2S_{1/2}$ level of Kr^+ are shown in the unit of eV. Part of the figure is adopted from ref. [1].

2.4. Summary

The coincidence photoelectron measurements revealed the selective creation of the $3s3p^5\ ^1P$ state of Ar^{2+} through a resonantly enhanced two-photon double ionization of Ar via the $3s3p^6np$ ($n \sim 25$) Rydberg states. In addition, a similar propensity was suggested in the two-photon double ionization of Kr, in which the $4s4p^5\ ^1P$ state of Kr^{2+} was selectively prepared through a resonantly enhanced two-photon double ionization of Kr via the $4s4p^6np$ ($n \sim 15$) Rydberg states. In the observed processes, it was suggested that the core electron configuration did not change when the excited neutral Ar and Kr are doubly ionized, and all the emitted electron pairs are in the singlet state. Our observation suggested that the one-photon double ionization of an excited rare gas atom with the $msmp^6np$ electron configuration shows a unique selectivity, and the process can be an attractive target for theoretical studies of the electron correlations in a many electron system. If the mechanism of the observed selectivity is clarified, it is expected that we can obtain useful insights into the control of resultant ionic states in photo-ionization processes.

2.5. Appendix

2.5.1. Correlation Maps of Ar in Higher Energy Region

The correlation maps of the slower electrons whose energy E_{slow} is below 21 eV and the faster electrons whose energy E_{fast} is below 30 eV are plotted in Fig. 2-26. Figures 2-26(a) and 26(b) were obtained in Condition 1 and Condition 2, respectively. Figure 2-26(a) exhibits vertical distributions at E_{fast} = 14.0, 15.7, 20.4 and 23.3 eV. The two vertical lines observed at 20.4 and 23.3 eV are assigned to false coincidence events between a slower electron and a $3p$ electron emitted after the single ionization by the 23rd and 25th harmonics. The two vertical lines at 14.0 and 15.7 eV are assigned to the ringing signals appearing ~36 μs after the false coincidence signals. In a similar manner, in Fig. 2-26(b), the two vertical lines at 19.9 and 22.9 eV are the false coincidence signals, and the two vertical lines at 13.8 and 15.6 eV are their ringing signals.

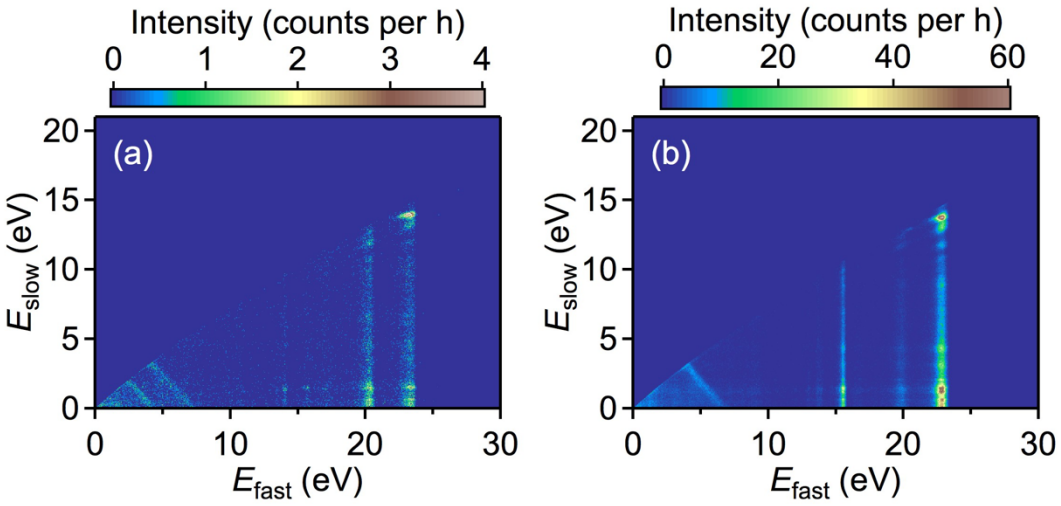

Figure 2-26 Correlation maps of the energies of the electrons emitted from Ar irradiated with the high-order harmonics generated in (a) Condition 1 and (b) Condition 2. The figure is adopted from ref. [1].

[1] K. Yamada, A. Iwasaki, T. Sato, K. Midorikawa, and K. Yamanouchi, Phys. Rev. A **94**, 053414 (2016).

[2] J. H. D. Eland, *Photoelectron Spectroscopy* (Butterworths, London, 1974).

[3] R. I. Hall, G. Dawber, A. G. McConkey, M. A. MacDonald, and G. C. King, Z Phys D **23**, 377 (1992).

[4] B. Möbus, K.-H. Schartner, A. Ehresmann, and H. Schmoranzer, Z Phys D **30**, 285 (1994).

[5] J. Eland, O. Vieuxmaire, T. Kinugawa, and P. Lablanquie, Physical Review **90**, 053003 (2003).

[6] Y. Hikosaka, M. Fushitani, A. Matsuda, C. M. Tseng, A. Hishikawa, E. Shigemasa, M. Nagasono, K. Tono, T. Togashi, H. Ohashi, H. Kimura, Y. Senba, M. Yabashi, and T. Ishikawa, Phys. Rev. Lett. **105**, 133001 (2010).

[7] N. Miyauchi, J. Adachi, A. Yagishita, T. Sako, F. Koike, T. Sato, A. Iwasaki, T. Okino, K. Yamanouchi, K. Midorikawa, K. Yamakawa, F. Kannari, H. Nakano, M. Nagasono, K. Tono, M. Yabashi, T. Ishikawa, T. Togashi, H. Ohashi, H. Kimura, and Y. Senba, J. Phys. B **44**, 071001 (2011).

[8] H. Fukuzawa, E. V. Gryzlova, K. Motomura, A. Yamada, K. Ueda, A. N. Grum-Grzhimailo, S. I. Strakhova, K. Nagaya, A. Sugishima, Y. Mizoguchi, H. Iwayama, M. Yao, N. Saito, P. Piseri, T. Mazza, M. Devetta, M. Coreno, M. Nagasono, K. Tono, M. Yabashi, T. Ishikawa, H. Ohashi, H. Kimura, T. Togashi, and Y. Senba, J. Phys. B **43**, 111001 (2010).

[9] H. W. van der Hart, K. W. Meyer, and C. H. Greene, Phys. Rev. A **57**, 3641 (1998).

[10] A. S. Kheifets, A. Ipatov, M. Arifin, and I. Bray, Phys. Rev. A **62**, 052724 (2000).

[11] J. Colgan and M. S. Pindzola, Phys. Rev. A **67**, 012711 (2003).

[12] A. Emmanouilidou, T. Schneider, and J.-M. Rost, J. Phys. B **36**, 2717 (2003).

[13] J. Colgan, D. C. Griffin, C. P. Ballance, and M. S. Pindzola, Phys. Rev. A **80**, 063414 (2009).

[14] A. S. Kheifets, D. V. Fursa, C. W. Hines, I. Bray, J. Colgan, and M. S. Pindzola, Phys. Rev. A **81**, 023418 (2010).

[15] F. L. Yip, C. W. McCurdy, and T. N. Rescigno, Phys. Rev. A **81**, 063419 (2010).

[16] A. D. Stauffer, Phys. Lett. **91A**, 114 (1982).

[17] G. H. Wannier, Phys. Rev. **90**, 817 (1953).

[18] H. Klar and W. Schlecht, J. Phys. B **9**, 1699 (1976).

[19] C. H. Greene and A. R. P. Rau, Phys. Rev. Lett. **48**, 533 (1982).

[20] A. Huetz, P. Selles, D. Waymel, and J. Mazeau, J. Phys. B **24**, 1917 (1991).

[21] A. Rau, J. Phys. B **9**, L283 (1976).

[22] J. M. Feagin, J. Phys. B **17**, 2433 (1984).

[23] D. Crothers, J. Phys. B **19**, 463 (1986).

[24] M. J. Alguard, V. W. Hughes, M. S. Lubell, and P. F. Wainwright, Phys. Rev. Lett. **39**, 334 (1977).

[25] G. Baum, M. Fink, W. Raith, H. Steidl, and J. Taborski, Phys. Rev. A **40**, 6734 (1989).

[26] G. Baum, W. Blask, P. Freienstein, L. Frost, and S. Hesse, Phys. Rev. **69**, 3037 (1992).

[27] G. Baum, M. Moede, and W. Raith, J. Phys. B **18**, 531 (1985).

[28] E. V. Gryzlova, R. Ma, H. Fukuzawa, K. Motomura, A. Yamada, K. Ueda, A. N. Grum-Grzhimailo, N. M. Kabachnik, S. I. Strakhova, A. Rouzée, A. Hundermark, M. J. J. Vrakking, P. Johnsson, K. Nagaya, S. Yase, Y. Mizoguchi, M. Yao, M. Nagasono, K. Tono, T. Togashi, Y. Senba, H. Ohashi, M. Yabashi, and T. Ishikawa, Phys. Rev. A **84**, 063405 (2011).

[29] A. N. Grum-Grzhimailo and E. V. Gryzlova, J. Mod. Opt. **63**, 334 (2016).

[30] R. J. Fonck, A. T. Ramsey, and R. V. Yelle, Appl. Opt. **21**, 2115 (1982).

[31] T. Kita, T. Harada, N. Nakano, and H. Kuroda, Appl. Opt. **22**, 512 (1983).

[32] N. Nakano, H. Kuroda, T. Kita, and T. Harada, Appl. Opt. **23**, 2386 (1984).

[33] B. L. Henke, E. M. Gullikson, and J. C. Davis, Atomic Data and Nuclear Data Tables **54**, 181 (1993).

[34] P. Kruit and F. H. Read, J. Phys. E **16**, 313 (1983).

[35] A. Kramida, Yu. Ralchenko, J. Reader, and NIST ASD Team, *NIST Atomic Spectra Database (ver. 5.2), (online)* (National Institute of Standards and Technology, Gaithersburg, MA, 2014).

[36] K. N. Huang, W. R. Johnson, and K. T. Cheng, Atomic Data and Nuclear Data Tables **26**, 33 (1981).

[37] E. P. Benis, D. Charalambidis, and T. N. Kitsopoulos, Phys. Rev. A **74**, 051402 (2006).

[38] K. Furusawa, T. Okino, T. Shimizu, and H. Hasegawa, Appl. Phys. B **83**, 203 (2006).

[39] R. P. Madden, D. L. Ederer, and K. Codling, Phys. Rev. **177**, 136 (1969).

[40] M. Spanner, S. Patchkovskii, C. Zhou, S. Matsika, and M. Kotur, Phys. Rev. A **86**, 053406 (2012).

[41] D. L. Ederer, A. C. Parr, J. B. West, D. Holland, and J. L. Dehmer, Phys. Rev. A **25**, 2006 (1982).

[42] K. Bartschat, Physics Reports **180**, 1 (1989).

[43] Y. Hikosaka, M. Fushitani, A. Matsuda, C. M. Tseng, A. Hishikawa, E. Shigemasa, M. Nagasono, K. Tono, T. Togashi, H. Ohashi, H. Kimura, Y. Senba, M. Yabashi, and T. Ishikawa, Phys. Rev. Lett. **105**, 133001 (2010).

Chapter 3

Observation of Laser-Enabled Auger Decay Process by Coincidence Photoelectron Spectroscopy

When an electron in the second outermost 3*s* orbital is emitted from Ar by photoionization, the Auger decay process does not normally occur. However, it has been recently suggested that the Auger decay proceeds when there is an additional laser field. This process is called a laser-enabled Auger decay (LEAD). In this work, Ar was irradiated with near-infrared (NIR) light pulses and their high-order harmonics, and photoelectron coincidence measurements were performed changing the time delay between the NIR pulses and the harmonics. A secondary electron emission after the emission of the 3*s* electron was observed only when Ar was irradiated with the NIR pulses after the irradiation of the harmonics. The observed process might be assigned to the LEAD process. Parts of this chapter is published in ref. [1].

3.1. Introduction

After the emission of an inner-valence electron in an atom by the irradiation of extreme ultra-violet light pulses, various types of relaxation processes, such as the Auger decay, proceed on the attosecond to femtosecond time scales. If we modify the energy of the secondary emitted electrons by additional short pulsed near-infrared (NIR) laser pulses and observe the time-delay dependence of the sideband peaks, the decay processes can be tracked in real-time [2]. However, this method could not be applied to decay processes emitting no secondary electron.

When an *ns* electron is emitted from the second outermost orbital in rare gas atoms, the created hole in the *ns* orbital is filled by an *np* electron from the outermost orbital (Fig. 3-1). Because the released energy by this hole-filling process is not large enough for another *np* electron to overcome the double ionization threshold energy, a radiative decay process instead of a secondary electron emission process occurs on the nanosecond time scale, that is, the Auger decay process is energetically forbidden. However, in recent studies [3,4], it was suggested from the time-delay dependence of Ar^{2+}

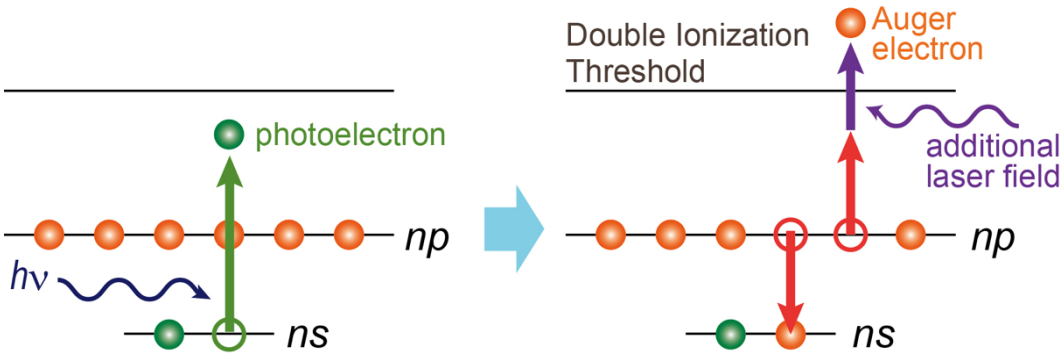

Figure 3-1 Schematic of the laser-enabled Auger decay process in rare gas atoms. An *ns* electron in the second outermost orbital is emitted by the absorption of an extreme ultra-violet photon. The created hole is filled by one of the *np* electrons in the outermost orbital, and another *np* electron is emitted by gaining the energy released in the relaxation of the *np* electron and the energy from the additional laser field. The secondary electron emission does not proceed when there is no additional laser field. The figure is adopted from ref. [1].

yield that the forbidden Auger decay process becomes an allowed process when there is an additional laser field. In these studies, Ar atoms were irradiated with high-order harmonics and the delayed additional NIR light pulses, and the photons from the additional laser field compensated energy deficiency for an *np* electron to be emitted as shown in Fig. 3-1. This process is called a laser-enabled Auger decay (LEAD) process [3,4], and it is expected to occur on the femtosecond time scale.

By forcing a secondary electron emission in a decay process, the decay dynamics after the hole creation by high-order harmonic pulses can be investigated. When a hole is created in a molecule, the hole is expected to migrate within the molecule, and a theoretical study showed that the cross section of the LEAD process is sensitively affected by the position of the hole [5], which means that the hole migration process can be investigated by making use of the LEAD process. However, the direct observation of the secondary electron emission through this process has not yet been reported for atoms nor molecules. This is probably because the cross section of the *ns* electron emission is too small and/or there are other competing double ionization processes. For example, the NIR assisted shake-off process and the non-sequential double ionization process induced by the combination of NIR light pulses and harmonics may bury the signal from the laser-enabled secondary electron emission which occurs after the *ns* electron emission.

In the present study, we performed photoelectron coincidence measurements of Ar irradiated with high-order harmonics and NIR light pulses, and tried to observe the signals purely from the LEAD process. In the following subsections, the previous works on the LEAD process are introduced, and experimental scheme of the observation of the signal purely from the LEAD process is described.

3.1.1. Previous Studies on Laser-Enabled Auger Decay Process

3.1.1.1. First Suggestion of the Existence of Laser-Enabled Auger Decay Process

Ranitovic et al. [3] irradiated Ar atoms with high-order harmonics having the energies of around 42 eV together with time-delayed intense near-infrared (NIR) light pulses, and they recorded the time-delay dependence of the ion yields using a cold target recoil ion momentum spectrometer. Figure 3-2(a) shows the observed Ar^{2+} and Ar^{2+}/Ar^{+} yields. The Ar^{2+}/Ar^{+} yield was 0.3 % when the NIR pulses came more than 50 fs before the harmonics, and the yield increased as the time delay decreased. The yield took the maximum value of 4 % when the NIR pulses temporally overlapped with the harmonics, and it decreased to 3 % when the NIR pulses came after the harmonics.

There are five possible double ionization processes which contribute to the creation of Ar^{2+} when the NIR pulses and the harmonics temporally overlap or when the NIR pulses come after the harmonics (Fig. 3-2(b)): (a) NIR assisted shake-off process, where the simultaneous absorption of the NIR pulses and the harmonics induces one electron emission followed by the second emission of an electron

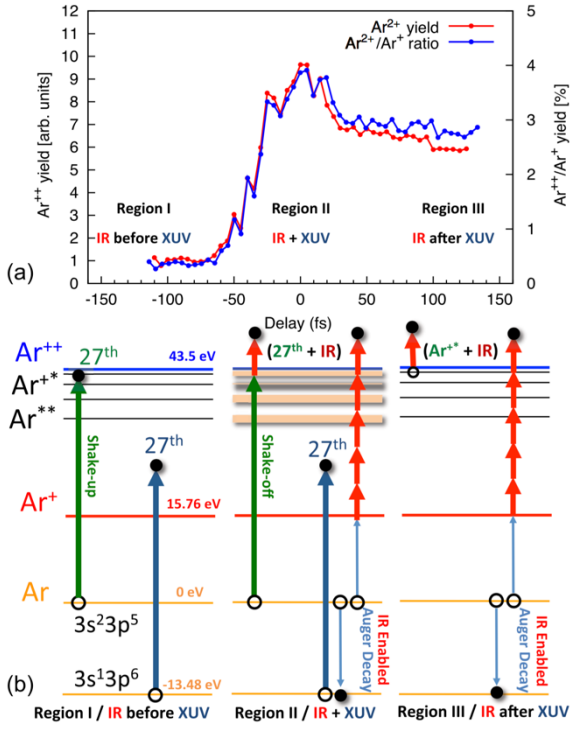

Figure 3-2 (a) Time-delay dependence of Ar^{2+} yield and Ar^{2+}/Ar^{+} yield observed by *Ranitovic et al.* [3] and (b) possible ionization pathways. The Ar^{2+}/Ar^{+} yield increased when the harmonics and the infrared (IR) pulses temporally overlapped. The LEAD process is expected to contribute to the observed increase of the Ar^{2+}/Ar^{+} yield. See the text for more detail. The figure is adopted from ref. [3].

having a low electron energy, (b) NIR assisted shake-up process, where the harmonics induce one electron emission followed by an excitation of another electron, and the excited electron is emitted by the absorption of the NIR pulses, (c) knockout ionization, where one electron absorbs the harmonics and the NIR pulses, and the electron interacts with another electron while it leaves the parent ionic core resulting in a simultaneous two electron emission, (d) double excitation of Ar induced by the harmonics followed by double ionization induced by the NIR pulses, and (e) the laser-enabled Auger decay process.

The maximum contribution of the processes (a), (b), and (c) to the Ar^{2+}/Ar^{+} yield at the time delay of zero is estimated by multiplying the 3*s* or 3*p* photoelectron yield having the energy above the double ionization threshold (P_t) by the total shake-off and shake-up probability after the removal of 3*s* or 3*p* electron (P_s). *Ranitovic et al.* [3] obtained the energy distribution of the electrons emitted by above-threshold ionization, $dP(E)/dE$, by solving the time-dependent Schrödinger integral equation using the split-operator method, and P_t was calculated to be 30 % by integrating $dP(E)/dE$ over the region where E is larger than the double ionization threshold energy. They calculated P_s by using the sudden approximation, and P_s was 4 % at the maximum. Therefore, the maximum contribution of the processes (a), (b), and (c) to the observed Ar^{2+}/Ar^{+} yield is 1.2 %. Because the observed Ar^{2+}/Ar^{+} yield was 4 % at the time delay of zero, this result indicates a significant contribution from the processes (d) and/or (e).

The doubly excited state created by the irradiation of the harmonics in the process (d) autoionizes on the femtosecond time scale, which reduces the Ar^{2+}/Ar^{+} yield. This decrease of the yield is observed when the NIR pulses come more than ~20 fs after the harmonics, which indicates the contribution of the process (d). However, the exact calculation of the contribution from the process (d) is theoretically difficult and *Ranitovic et al.* did not perform the calculation.

The contribution from the laser-enabled Auger decay process (e) was estimated by calculating the laser-intensity dependent Auger decay rate [3,4]. The outline of their calculation is provided in the following. The wave functions of the $3s3p^6\ ^2S$ state of Ar^{+}, the resulting $3s^23p^4\ ^1S$ or ^1D state of Ar^{2+}, and the secondary emitted electron in the Auger decay are defined to be $\Psi_h(N-1)$, $\Psi_c(N-2)$, and ψ_a, respectively. Their corresponding Hamiltonians are $H_h(N-1)$, $H_c(N-2)$, and h_a, respectively. $h_a(t)$ is written as

$$h_a(t) = -\frac{\nabla^2}{2} + V_{eff}(r) - zE(t), \tag{3-1}$$

where $V_{eff}(r)$ is the model potential [6] of the atomic ions, and z is the electron coordinate parallel to

the polarization direction of the NIR. When $F(\boldsymbol{r})$ is written as

$$F(\boldsymbol{r}) = \langle \Psi_c(N-2)|V_{res}(\tau)|\Psi_h(N-1)\rangle, \tag{3-2}$$

where $V_{\mathrm{res}}(\tau) = H_{\mathrm{c}}(N-2) + h_{\mathrm{a}}(\tau) - H_{\mathrm{h}}(N-1)$, the time evolution of the Auger electron wave function, ψ_a, can be written as

$$\psi_a(\boldsymbol{r}, t) = -i \int_{-\infty}^{t} e^{-i\int_{\tau}^{t} h_a(t')dt'} e^{-i(E_h - E_c)\tau} F(\boldsymbol{r}) d\tau, \tag{3-3}$$

where E_{h} and E_{c} are the total energies of $\Psi_h(N-1)$ and $\Psi_c(N-2)$, respectively. Eq. (3-3) expresses that the secondary electron is emitted at time τ and the wave function propagates until time t in the Hamiltonian of h_{a}. By defining a radial function $f(r)$ as

$$f(r) = \int_0^{\infty} R_{3s}(r_1) \frac{r_<}{r_>^2} R_{3p}(r_1) R_{3p}(r) r_1^2 dr_1, \tag{3-4}$$

where $r_<$ and $r_>$ represents the smaller and larger one of the r and r_1, respectively, and $R_{nl}(r)$ is the radial wave function. $F(r)$ is rewritten by using $f(r)$ and the spherical surface harmonics $Y_{lm}(\hat{\boldsymbol{r}})$ as

$$F(\boldsymbol{r}) = -\frac{1}{\sqrt{3}} f(r) Y_{00}(\hat{\boldsymbol{r}}), \tag{3-5}$$

for the creation of the ^1S state of Ar^{2+}, and

$$F(\boldsymbol{r}) = -\sqrt{\frac{2}{15}} f(r) Y_{2M}(\hat{\boldsymbol{r}}), \tag{3-6}$$

for the creation of the ^1D state of Ar^{2+}. Substituting Eq. (3-5) or (3-6) in Eq. (3-3), ψ_a was numerically calculated, and when a temporal window function $e^{-\tau^2/T^2}$ was added to the equation (3-3), ψ_a at temporal infinity is expressed in the form of

$$\psi_a(\boldsymbol{r}, t \to \infty) = \int C(\varepsilon) \psi_\varepsilon(\boldsymbol{r}) d\varepsilon, \tag{3-7}$$

where $\psi_\varepsilon(\boldsymbol{r})$ is the atomic continuum wave function without a laser field. Because the distribution of the emitted electron energy $dP(\varepsilon)/d\varepsilon$ is the square of $C(\varepsilon)$ in Eq. (3-7), the LEAD rate (R_{a}) is

$$R_a = \frac{\sqrt{2\pi}}{T} \int_0^{\infty} |C(\varepsilon)|^2 d\varepsilon. \tag{3-8}$$

The calculated result of the NIR-intensity dependence of R_{a} for Ar is shown in Fig. 3-3, which is adopted from ref. [3].

The dashed black line in Fig. 3-3 indicates the rate of the radiative decay. Although the radiative decay is dominant when the NIR laser intensity is less than 5×10^{12} W/cm^2, the Auger decay rate becomes comparable to the radiative decay rate when the NIR laser intensity is around 10^{13} W/cm^2,

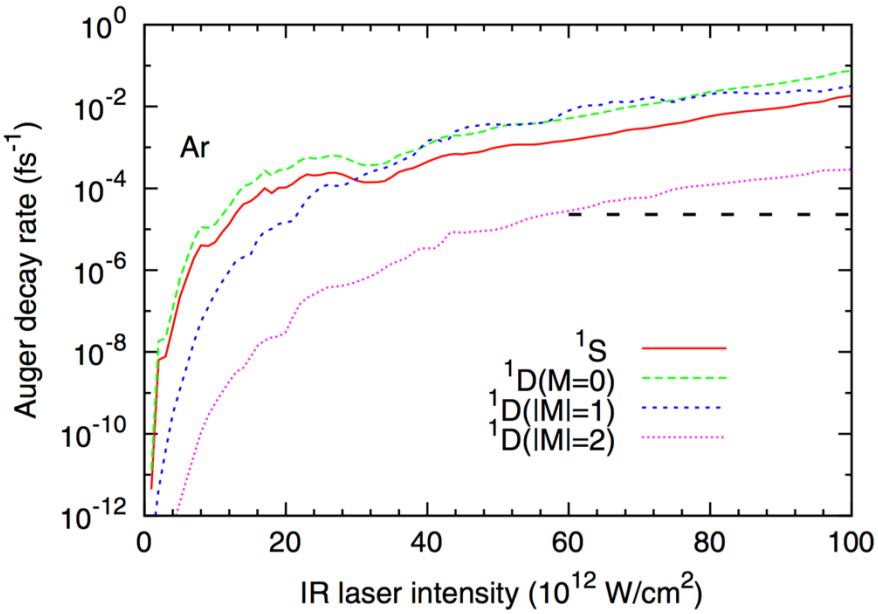

Figure 3-3 IR laser intensity dependence of Auger decay rate when Ar^{2+} are created in the ^1S state (red line), ^1D(M=0) state (green line), ^1D(|M|=1) state (blue line), and ^1D(|M|=2) state (pink line) calculated by *Ranitovic et al.* [3]. The dashed black line indicates the radiative decay rate. The figure is adopted from ref. [3].

and it becomes even larger as the intensity of the NIR pulses increases. Instead of calculating how much the LEAD process contributes to the observed Ar^{2+}/Ar^{+} yield ratio, *Ranitovic et al.* showed that the LEAD process becomes comparable to the radiative decay process, which means that the LEAD process should contribute to the creation of Ar^{2+}.

3.1.1.2. Application of Laser-Enabled Auger Decay process

The LEAD process can also proceed when the additional energy necessary for the secondary electron emission is given by the absorption of one extreme-ultraviolet (EUV) photon, not by multiple NIR photons. This process is called a single-photon LEAD (sp-LEAD) process, whose existence has been theoretically suggested [5].

In the sp-LEAD process, absorption of the second EUV photon induces the relaxation of an outer-valence electron to the inner-valence hole and the emission of another outer-valence electron. In this process, the situations of two electrons are changed by the absorption of one photon. This type of change in the electron configuration cannot be described by one single-electron dipole operator, and the configuration interaction must be taken into consideration. This makes the sp-LEAD process different from the LEAD process induced by the multi-photon absorption, where the decay can be described by more than one single-electron dipole operators. Because the cross section of the sp-

LEAD process is expected to be strongly affected by the configuration mixing, the sp-LEAD process might be useful for tracking a process in which the configuration mixing plays an important role.

One of such processes is the ultrafast hole migration process within a molecule [7], which occurs on the sub-femtosecond to few-femtosecond time scales. Because the rearrangements of the nuclear position occur on the several tens of femtosecond time scale, this process is solely induced by the configuration mixing. Therefore, it might be possible to temporally track this process by measuring the temporal evolution of the cross section of the sp-LEAD process.

The application of the sp-LEAD process to the observation of the hole migration process has been theoretically simulated by *Cooper and Averbukh* [5]. They chose glycine as the target, and they considered the situation where the electron is suddenly removed from the $11A'$ molecular orbital resulting in the oscillation between the $11A'$- and $12A'$-ionized states. They calculated the temporal evolution of the survival probability of the initial ionic state, which has a hole on a certain position of the molecule. When the hole migrates away from the initial position, the survival probability decreases, and when the hole comes back to the initial position, the survival probability increases. This means that the survival probability reflects the position of the hole in the molecule. The temporal evolution of the cross section of the sp-LEAD process was also calculated, and Fig. 3-4 shows that the temporal modulation of the cross section of the sp-LEAD is synchronized with the oscillation of the survival probability, in other words, the oscillation of the hole position. This result indicates that the ultrafast

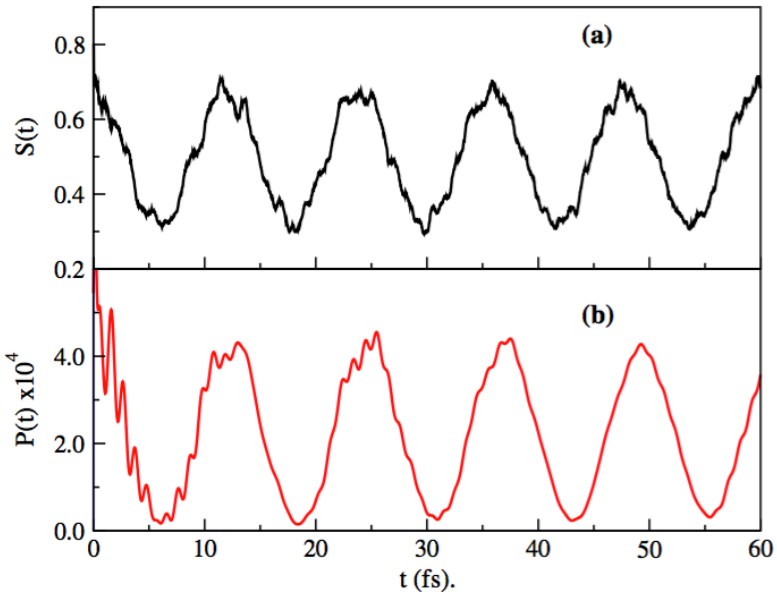

Figure 3-4 (a) Temporal evolutions of the survival probability and (b) the cross section of the sp-LEAD process in glycine induced by the sudden removal of an electron from the $11A'$ molecular orbital. The figure is adopted from ref. [5].

hole migration process can be tracked by measuring the time-delay dependence of the signals generated as a result of the sp-LEAD process, such as the yield of the doubly charged ions or the yield of the secondary emitted electrons.

3.1.2. Purpose and the Experimental Scheme in This Work

In this work, we tried to observe the LEAD process of Ar by coincidence photoelectron spectroscopy. Ar has six electrons in the outermost $3p$ orbital and two electrons in the second outermost $3s$ orbital. The first step of the LEAD process, in which one of the $3s$ electrons is removed, can be induced by around 23rd harmonics, and the emitted $3s$ electron has the energy E_{1st} described as

$$E_{1st} = h\nu_{HH} - E(Ar^+, 3s3p^6), \tag{3-9}$$

where $h\nu_{HH}$ is the photon energy of the harmonic, and $E(Ar^+, 3s3p^6) = 29.2$ eV [8] is the energy of the created $3s3p^6\ ^2S$ state of Ar^+ from the ground state of Ar (Fig. 3-5). When one of the $3p$ electrons relaxes to fill the $3s$ hole in the $3s3p^6\ ^2S$ state of Ar^+, energy α is released, and another one of the $3p$ electrons is emitted by gaining the released energy α and the energy of the NIR photons $h\nu_{NIR}$. The energy of the electron emitted in this process E_{2nd} is written as (Fig. 3-5)

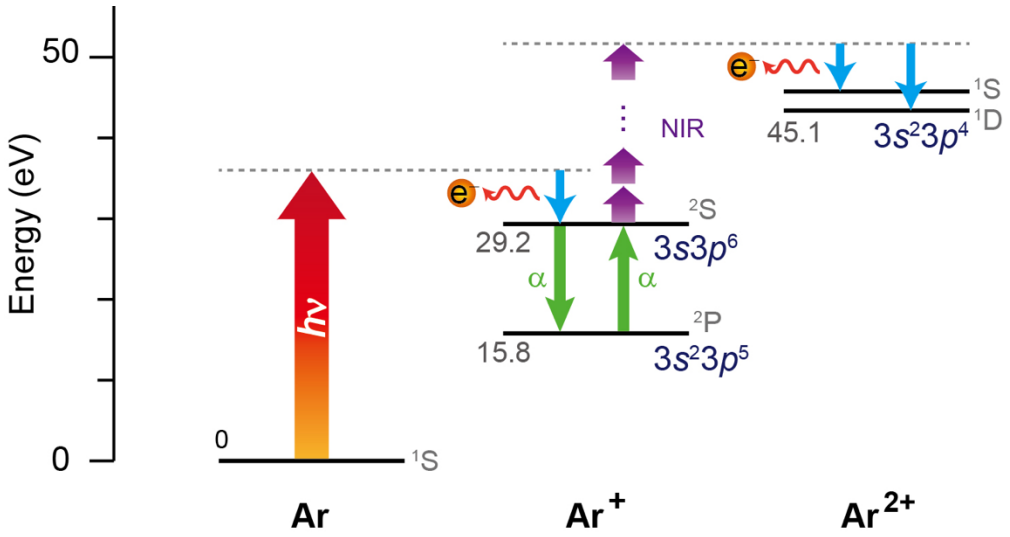

Figure 3-5 Schematic of the LEAD process in Ar. When Ar absorbs an extreme-ultraviolet photon, the $3s3p^6\ ^2S$ state of Ar^+ is created emitting an electron having the energy which corresponds to the energy difference between the absorbed photon and the energy of the created Ar^+. When Ar^+ absorbs multiple NIR photons, the $3s^23p^4\ ^1S$ and ^1D states of Ar^{2+} are created emitting an electron. This energy corresponds to the energy difference between the resultant Ar^{2+} and the sum of the total energy of the absorbed NIR photons and the energy of Ar^+ in the $3s3p^6\ ^2S$ state from the neutral ground state.

$$E_{2nd} = n \times h\nu_{NIR} + \alpha - (E(Ar^{2+}, 3s^2 3p^4) - E(Ar^{+}, 3s^2 3p^5)), \quad (3\text{-}10)$$

where n is the number of absorbed NIR photons, $E(Ar^{2+}, 3s^2 3p^4)$ is the energy of the created Ar^{2+} ($3s^2 3p^4$), $E(Ar^{+}, 3s^2 3p^5)$ is the energy of the intermediate Ar^{+} ($3s^2 3p^5$). Because α is the energy difference between Ar^{+} ($3s 3p^6$) and Ar^{+} ($3s^2 3p^5$), Eq. (3-10) is rewritten as

$$E_{2nd} = n \times h\nu_{NIR} - (E(Ar^{2+}, 3s^2 3p^4) - E(Ar^{+}, 3s 3p^6)), \quad (3\text{-}11)$$

where $E(Ar^{2+}, 3s^2 3p^4) - E(Ar^{+}, 3s 3p^6)$ = 15.89 eV and 18.27 eV when the ^1D and the ^1S states are created, respectively. Because $h\nu_{NIR}$ = 1.56 eV when the wavelength of the NIR pulse is 795 nm, n should be larger than ten in order to induce the LEAD process.

As described in section 3.1.1.1, when Ar is irradiated with high-order harmonics and NIR pulses, (a) NIR assisted shake-off process, (b) NIR assisted shake-up process, (c) knockout ionization, and (d) double excitation of Ar by the harmonics followed by double ionization by the NIR pulses are expected to occur in addition to the LEAD process. The LEAD process can be distinguished from the processes (a)-(d) by a pump-probe photoelectron coincidence spectroscopy as follows: Because the process (a) is induced when the harmonics and the NIR pulses are temporally overlapped, the contribution of (a) to the double ionization of Ar is eliminated when the NIR pulses comes after the harmonics although the LEAD process still occurs. The process (b) is induced when Ar is simultaneously irradiated with the harmonics and the NIR pulses or when the NIR pulses comes after the harmonics. This means that the photoelectron signals from the process (b) might overlap with the signals from the LEAD process when the energy of the electron emitted in the shake-up process coincides with E_{1st} in the LEAD process. This can occur when the $3s^2 3p^4 3d\ ^4D$ state of Ar^{+}* is created in the shake-up process induced by the Nth harmonic for the following reason: The energy of the emitted $3p$ electron E_{3p} in the creation of the $3s^2 3p^4 3d\ ^4D$ state of Ar^{+}* is

$$E_{3p} = h\nu_{HH,\,N} - E(Ar^{+}*, 3s^2 3p^4 3d, {}^4D), \quad (3\text{-}12)$$

where $h\nu_{HH,\,N}$ is the photon energy of the Nth harmonic. E_{3p} is close to E_{1st} when the $3s 3p^6\ ^2D$ state of Ar^{+} is created by the (N–2)th harmonic in the LEAD process written as

$$E_{1st} = h\nu_{HH,\,N-2} - E(Ar^{+}, 3s 3p^6, {}^2D) \quad (3\text{-}13)$$

because the energy difference of 2.95 eV between $E(Ar^{+}*, 3s^2 3p^4 3d, {}^4D)$ and $E(Ar^{+}, 3s 3p^6, {}^2D)$ is close to the energy difference of ~3.1 eV between $h\nu_{HH,\,N}$ and $h\nu_{HH,\,N-2}$. However, the conservation rule of the total spin angular momentum forbids the creation of the $3s^2 3p^4 3d\ ^4D$ state of Ar^{+} from the ^1S ground state of Ar, therefore, it is expected that there are no coincidence signals from the process (b) which overlaps with the coincidence signals from the LEAD process. In the processes (c) and (d), two electrons are simultaneously emitted, and these processes appear as lines with a slope of −1.0 in the

correlation map of the energies of the emitted electrons, whereas the signal from the LEAD process is expected to appear as a spot in the correlation map. This means that the signals from the processes (c) and (d) can be distinguished from the LEAD process by the shape of the signals in the correlation map. Therefore, it is possible to distinguish the coincidence signals of the LEAD process from the signals assigned to the other double ionization processes as long as the NIR pulses do not temporally overlap with the harmonics.

3.2. Experimental Setup

Figure 3-6 shows the schematic of the experimental setup. The setup is almost the same as the one used in Chapter 2, but in this experiment, the Ti:sapphire laser pulses (1 kHz, ~9 mJ, ~40 fs, ~795 nm) were split into two by a beam splitter with 95 % transmittance, in order to use the 95 % of the beam for the generation of the high-order harmonics and the 5 % of the beam as the additional NIR laser field.

The transmitted 95 % of the beam was focused by a plano-convex lens (f = 2 m) into a 15 mm-long gas cell filled with an Ar gaseous medium in order to generate high-order harmonics. The generated harmonics were reflected by two Si mirrors at the Brewster's angle of the fundamental light pulses, and led through an Al filter (200 nm thickness) so that the intensities of the lower order harmonics and the fundamental light pulses become negligibly small. The harmonics were then reflected by two SiC/Mg multi-layered mirrors which have the highest reflectivity (~50 %) at around 36 eV, and mainly the 21st, 23rd, and 25th harmonics were selected.

The size of the reflected 5 % NIR pulses were reduced ~3.6 times from the original size by using two lenses (f = 2.5 and 0.7 m) in order not to cut the outer part of the beam by a holed mirror in the downstream. The intensity of the beam was reduced by neutral density filters so that the multi-photon ionization process induced by only the NIR pulses becomes not dominant. The NIR pulses were reflected by a retroreflector on an x-axis stage (TSDS-401S, Sigmakoki) and a piezo linear stage (P-621.1CD, PI), and the pulses were combined with the harmonics by using a mirror with a hole (2mm ϕ) in the center. The time delay of the NIR pulses to the harmonics was varied by using the piezo linear stage.

The harmonics and the NIR light pulses were back-focused on an Ar gas sample at the interaction region in a magnetic-bottle type photoelectron spectrometer (FOM, Netherland) [9], using a SiC/Mg multi-layered plano-concave mirror (f = 150 mm). The emitted electrons were detected by a

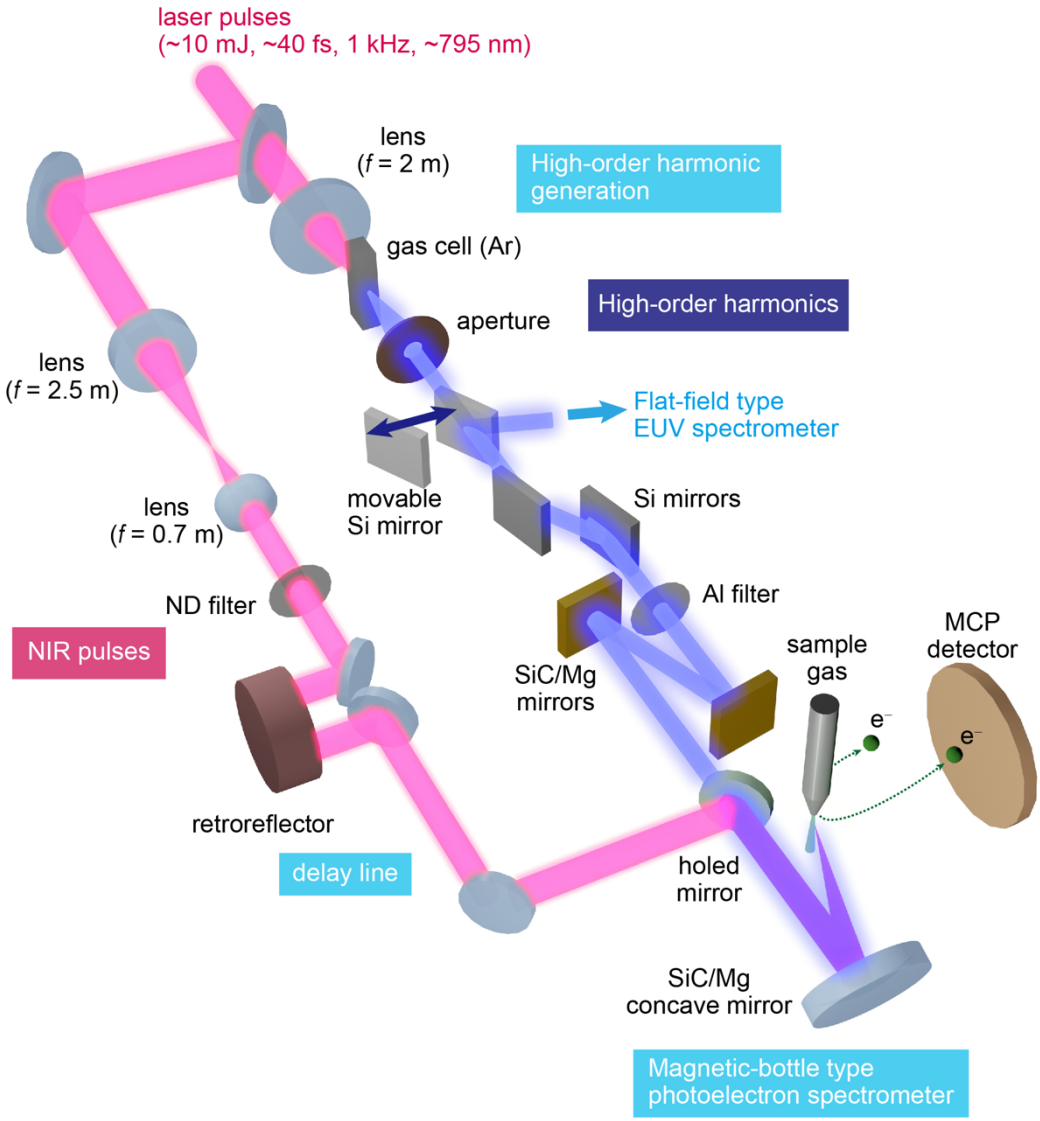

Figure 3-6 Schematic of the experimental setup. The 95 % of the laser pulses were used for the generation of the high-order harmonics, and the 5 % of the laser pulses were led to the delay line. The harmonics and the delayed NIR pulses were recombined with a holed mirror. The combined beam was focused on the sample gas, and the energies of the emitted electrons were measured by a magnetic-bottle type photoelectron spectrometer.

microchannel plate detector (PHOTONIS) and processed by a data acquisition board (TDC8HP, RoentDek) in order to extract the coincidently detected two electrons in each laser shot, and then, the correlation maps of the kinetic energies of the emitted electrons were constructed.

The measurement was performed while alternately changing the time delay between −200 fs (NIR pulses before harmonics) and +50 fs (NIR pulses after harmonics) every 3 seconds. The total

accumulation time was 365 minutes. Each photoelectron signal was recorded with the information of the time delay, and the obtained signals were sorted into data sets for −200 fs and +50 fs after the measurement.

3.3. Results and Discussions

Figure 3-7 shows the photoelectron spectrum of Ar irradiated only with the NIR pulses. The observed peaks are assigned to the emissions of 3*p* electrons by multi-photon single ionization processes. The number of NIR photons absorbed and the total photon energies derived from the observed photoelectron peaks are shown in Table 3-1. With the intensity of the NIR pulses used in the measurement of Fig. 3-7, false coincidence signals did not appear in the correlation map of the energies of the faster and slower electrons. Therefore, the pump-probe experiments were performed without changing the intensity of the NIR pulses from the one used in the observation of Fig. 3-7.

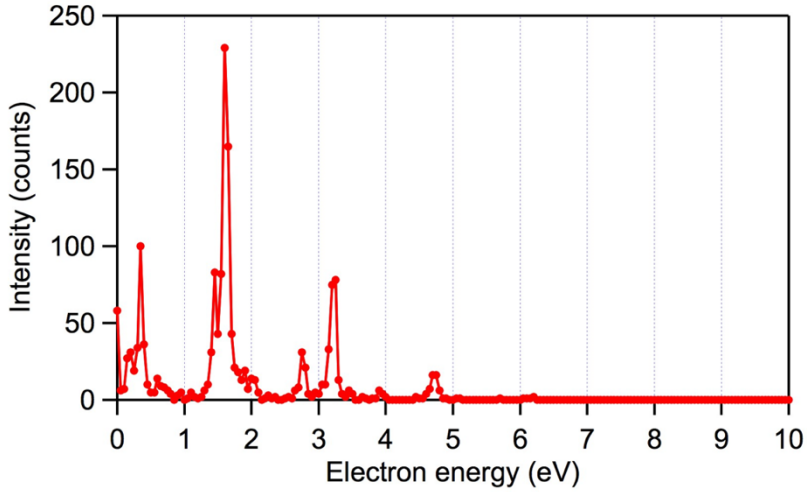

Figure 3-7 Photoelectron spectrum of Ar irradiated with only the NIR pulses. The observed peaks are assigned to the above threshold ionization induced by ten to thirteen photons.

Table 3-1 Number of absorbed NIR photons and total photon energy.

Number of NIR photons	Total photon energy* (eV)
10	16.15(1)
11	17.40(5)
12	19.1(1)
13	20.5(2)

*Calculated assuming that the first ionization potential of Ar is 15.8 eV [8].

Figure 3-8 shows the energy distribution of the faster electrons observed when the time delays are −200 fs (NIR pulses come 200 fs before the harmonics) and +50 fs (NIR pulses come 50 fs after the harmonics) in the energy region from 0 to 11.5 eV. The photoelectron spectrum at +50 fs was similar to the one at −200 fs. The observed peaks are assigned to the 3*p* electron emissions induced by the 11th to 17th harmonics and the 3*s* electron emissions induced by the 21st to 25th harmonics. The 3*s* electron emission is the first step of the LEAD process, and the second electron emitted in the LEAD process is expected to be detected in coincidence with the 3*s* electrons observed in Fig. 3-8.

The correlation maps of the faster and slower electrons for the time delays of −200 fs and +50 fs are shown in Figs. 3-9(a) and 9(b), respectively, along with the energy distribution of the faster electrons (Fig. 3-9(c)). Both in the cases when the time delays are −200 fs and +50 fs, two diagonal-line shaped structures are observed. These are assigned to the selective creations of the $3s3p^5\ ^1P$ state of Ar^{2+} through the simultaneous two-electron emission processes induced by 19th + 23rd harmonics and 19th + 25th harmonics via an intermediate state [10], and these signals do not depend on the presence of the NIR field.

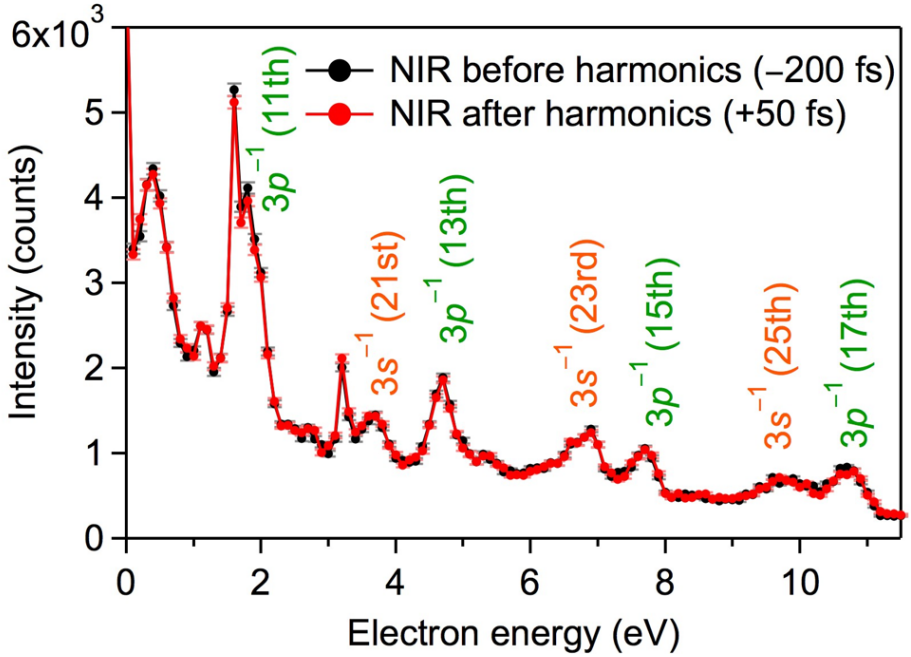

Figure 3-8 Distribution of the energy of the faster electron observed when Ar is irradiated with the NIR pulses before the harmonics (black) and when Ar is irradiated with the NIR pulses after the harmonics (red). The observed peaks are assigned to the 3*p* electron emissions induced by the 11th to 17th harmonics and the 3*s* electron emissions induced by the 21st to 25th harmonics.

In order to extract the signals from the secondary electron emission processes after the 3*s* electron emissions by the 21st, 23rd, and 25th harmonics, the coincidence electron signals with the faster electron kinetic energy of 3.4 to 4.1, 6.4 to 7.1, and 9.2 to 10.2 eV in Figs. 3-9(a) and 9(b) were picked out, and the kinetic energy distributions of the slower electrons for both time delays were plotted in Fig. 3-10. Although the energy distributions at −200 fs and +50 fs are similar when the faster electron is the 3*s* electron emitted by the 21st or 25th harmonics (Figs. 3-10(a), 10(b), 10(e), and 10(f)), when

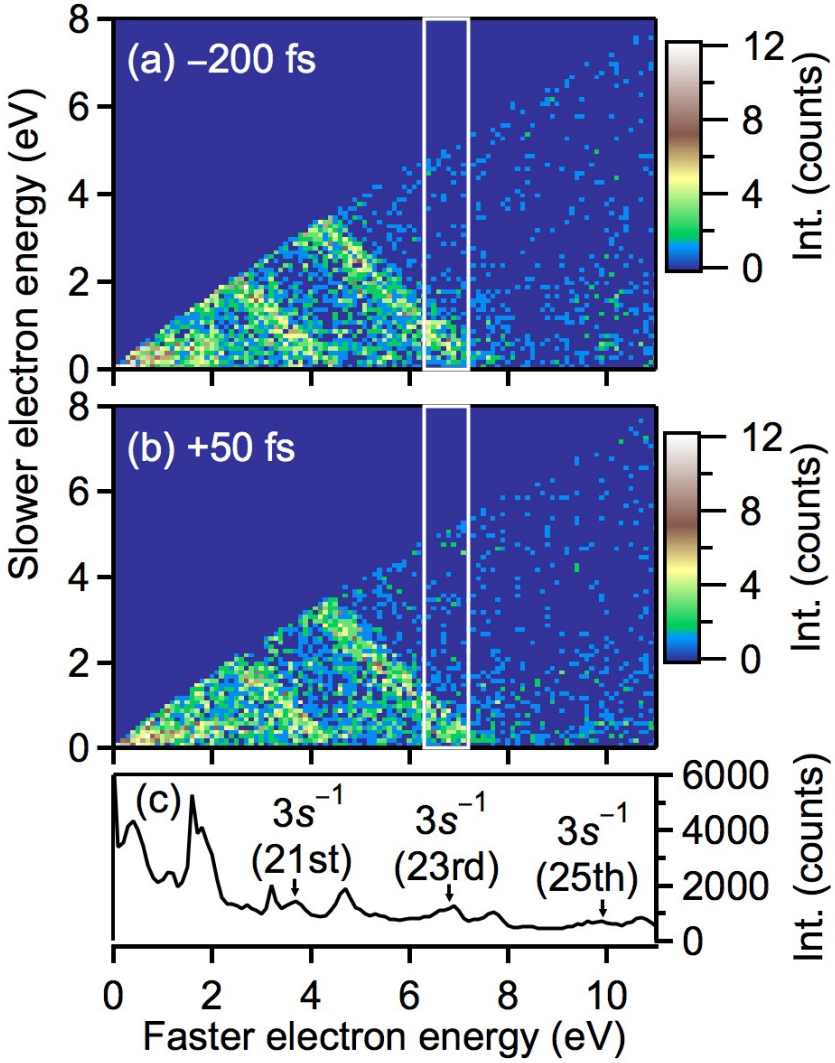

Figure 3-9 Correlation maps of the energies of the slower and faster electrons when the time delay is (a) −200 fs and (b) +50 fs along with (c) the energy distribution of the faster electrons. The white boxes in (a) and (b) indicate the areas where the faster electrons are the 3*s* electrons emitted by the absorption of the 23rd harmonic. The figure is adopted from ref. [1].

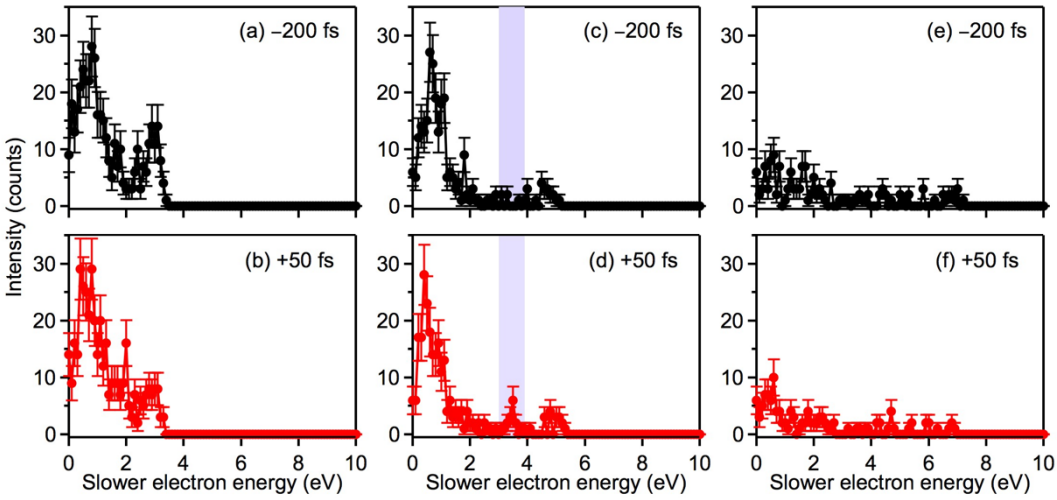

Figure 3-10 Energy distributions of the slower electrons detected in coincidence with 3*s* electrons emitted by (a,b) the 21st, (c,d) the 23rd, and (e,f) the 25th harmonics. (a), (c), and (e) are observed when the time delay is –200 fs, and (b), (d), and (f) are observed when the time delay is +50 fs. (c) and (d) are adopted from ref. [1].

the faster electron is the 3*s* electron emitted by the 23rd harmonic, a peak appeared at 3.5 ± 0.1 eV in the kinetic energy distributions of the slower electron at the time delay of +50 fs (Fig. 3-10(d)), while not at the time delay of –200 fs (Fig. 3-10(c)).

In order to confirm that the peak at 3.5 eV observed in Fig. 3-10(d) is not a noise accidentally detected in the middle of the measurement, the accumulated signals were separated into the signals observed in the first half of the accumulation time and the signals observed in the last half of the accumulation time. As shown in Fig. 3-11, both of the spectra observed in the first half and in the last half of the accumulation time showed a peak at 3.5 eV when the time delay is +50 fs. This means that the observed peak at 3.5 eV is not a noise, and the peak is assigned to the secondary electron emission after the 3*s* electron emission by the 23rd harmonic, which was enabled by the presence of the NIR pulses.

Table 3-2 shows the expected energies of the secondary electrons emitted in the creation of Ar^{2+} ($3s^2 3p^4$) from Ar^+ ($3s3p^6$) with the assist of the absorption of NIR photons, which are derived by using the observed total NIR photon energies listed in Table 3-1. The observed peak energy of 3.5 eV is close to the expected energy of the secondary electron emitted in the ionization of Ar^+ ($3s3p^6$) to the $3s^2 3p^4\ ^1D$ state of Ar^{2+} with the assist of twelve NIR photons (Fig. 3-12, Table 3-2). In this process, one of the 3*p* electrons relaxes to the 3*s* orbital, and another 3*p* electron is emitted, therefore, there is a possibility that the observed signals are from the LEAD process.

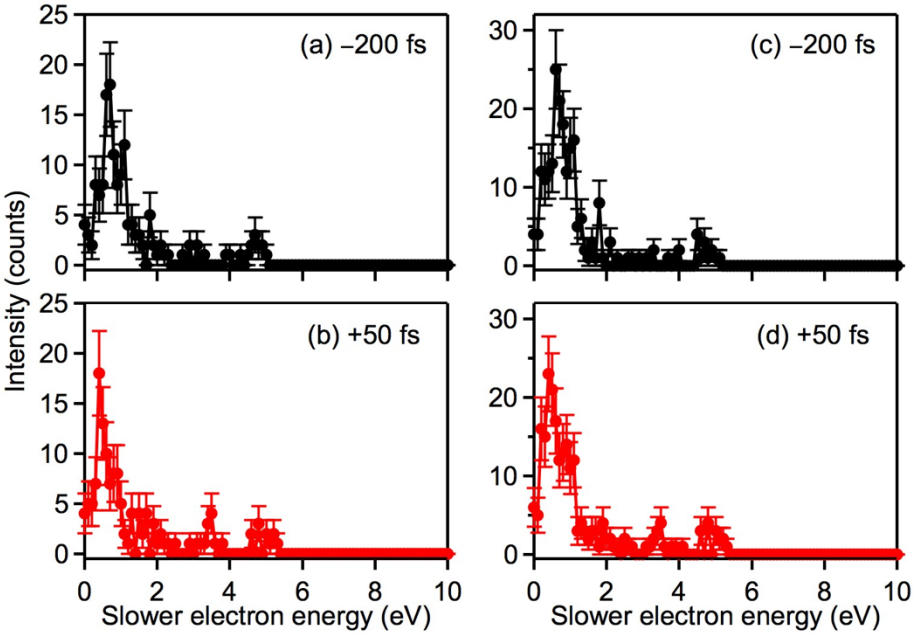

Figure 3-11 Energy distribution of the slower electrons detected in coincidence with the 3*s* electrons emitted by the 23rd harmonic. (a) and (b) are observed in the first half of the accumulation time, and (c) and (d) are observed in the last half of the accumulation time. (a) and (c) are observed when the time delay is –200 fs, and (b) and (d) are observed when the time delay is +50 fs.

Table 3-2 Expected secondary electron energies in the creation of Ar^{2+} ($3s^2 3p^4$) from Ar^+ ($3s3p^6$).*

Number of NIR photons	Ar^{2+} ($3s^2 3p^4$) states	
	^1D	^1S
10	0.260(1)	-
11	1.51(5)	-
12	3.2(1)	0.8(1)
13	4.6(2)	2.2(2)

*The energies are in the unit of eV.

Table 3-2 also shows the other expected secondary electron energies in the NIR assisted ionization processes creating the $3s^2 3p^4\ ^1D$ and ^1S states of Ar^{2+} from Ar^+ ($3s3p^6$). The creation of the $3s^2 3p^4\ ^3P$ state of Ar^{2+} is not expected considering the conservation of the angular momentum and parity [3,4]. When the 3*s* electron is emitted by the 23rd harmonic, the secondary electrons emitted in the creation processes of Ar^{2+} in the ^1D state by ten and eleven NIR photons and the secondary electrons emitted in the creation process of Ar^{2+} in the ^1S state by twelve NIR photons may be overlapped with the diagonal-line shaped structure from the two-photon direct double ionization process observed in Fig.

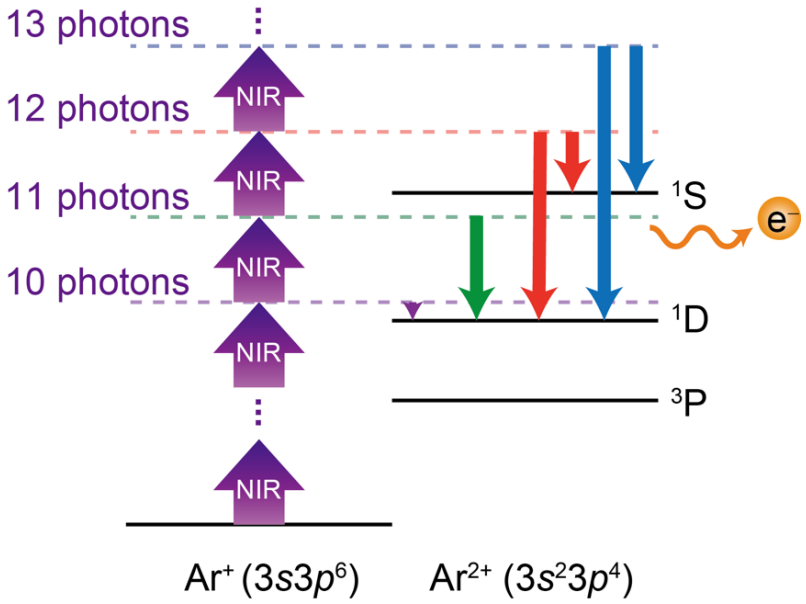

Figure 3-12 Schematic of the secondary electron emission process in the LEAD process. The $3s^2 3p^4$ ^1D state of Ar^{2+} is created by the absorption of more than ten NIR photons, and the $3s^2 3p^4$ ^1S state of Ar^{2+} is created by the absorption of more than twelve NIR photons. The figure is adopted from ref. [1].

3-9(b). The creation of Ar^{2+} ($3s^2 3p^4$) from Ar^+ ($3s3p^6$) with the absorption of thirteen or more NIR photons may not be observed because the intensity of the NIR pulses was not high enough to induce these processes.

When the 3*s* electron is emitted by the 21st harmonic, the secondary electrons with the energies listed in Table 3-2 were not resolved because the signals overlapped with the diagonal-line shaped structure. The reason why the secondary electrons listed in Table 3-2 were not observed when 3*s* electron is emitted by the 25th harmonic might be because the intensity of the 25th harmonic was not intense, and the number of emitted 3*s* electrons was so small that not enough number of coincidence signals from the LEAD process were accumulated.

The difference between the observed secondary electron energy of 3.5 eV and the expected electron energy of 3.2 eV for the LEAD process creating the $3s^2 3p^4$ ^1D state of Ar^{2+} may attribute to the broadening of the NIR photon energy distribution and/or the screening effect induced by the firstly emitted electron, which could reduce the energy defect and increase the energy of the secondary emitted electron [4].

The screening effect in the LEAD process of Ar has been theoretically suggested by *Tong et al.* [4]. When the secondary electron emission is induced while the firstly emitted electron still exists

close to the parent ion, the energy defect becomes smaller than when the first electron is far from the parent ion, which increases the LEAD rate and the energy of the secondary emitted electron. This is called the screening effect. They used a Debye screening potential in the calculation of the energy defect by the density functional theory with self-interaction-correction method. The Debye screening potential is defined as

$$V(r) = -\frac{Z}{r} e^{-r/\lambda_d}, \tag{3-14}$$

where Z is the atomic number and λ_d is the Debye length defined as

$$\lambda_d = \sqrt{\frac{3v^5 t^3}{2}}, \tag{3-15}$$

where v is the velocity of the firstly emitted electron and t is the time after the first electron emission. The calculated λ_d dependence of the energy defect is shown in Table 3-3.

Table 3-3 λ_d dependence of energy defect in the LEAD process of Ar.

λ_d (a.u.)	Energy defect* (eV)	Reduced defect (eV)
(without screening)	14.1	-
500	13.2	0.9
200	11.8	2.3
100	9.4	4.7

*Data adopted from ref. [4].

When the energy of the firstly emitted electron is 6.8 eV, t is calculated to be 2.37, 1.29, and 0.81 fs when λ_d is 500, 200, and 100 a.u., respectively. Because t in our measurement is +50 fs, the reduced defect is expected to be smaller than 0.9 eV from Table 3-3, which is consistent with the observed secondary emitted electron energy of 0.3 eV.

Although the accumulation time was not long, the experimental result suggested the observation of the LEAD process induced by the 23rd harmonic and twelve NIR photons.

3.4. Conclusion

When Ar atoms were irradiated with NIR light pulses after the high-order harmonics, secondary electron emission after the 3*s* electron emission was observed in the photoelectron coincidence spectrum. From the observed electron energies, it was suggested that the observed process might be

assigned to the LEAD process induced by the 23rd harmonic and twelve NIR photons. In order to confirm whether the observed process is the LEAD process, the photoelectron coincidence measurements will be performed with a longer accumulation time, and the time delay will be scanned to temporally follow the process.

[1] K. Yamada, A. Iwasaki, T. Sato, K. Midorikawa, and K. Yamaouchi, International Conference on Ultrafast Phenomena, OSA Technical Digest (online) (Optical Society of America, 2016), paper UM2B.7.

[2] M. Drescher, M. Hentschel, R. Kienberger, M. Uiberacker, V. Yakovlev, A. Scrinzi, T. Westerwalbesloh, U. Kleineberg, U. Heinzmann, and F. Krausz, Nature **419**, 803 (2002).

[3] P. Ranitovic, X. M. Tong, C. W. Hogle, X. Zhou, Y. Liu, N. Toshima, M. M. Murnane, and H. C. Kapteyn, Phys. Rev. Lett. **106**, 053002 (2011).

[4] X. M. Tong, P. Ranitovic, C. W. Hogle, M. M. Murnane, H. C. Kapteyn, and N. Toshima, Phys. Rev. A **84**, 013405 (2011).

[5] B. Cooper and V. Averbukh, Phys. Rev. Lett. **111**, 083004 (2013).

[6] X. M. Tong and C. D. Lin, J. Phys. B **38**, 2593 (2005).

[7] F. Calegari, A. Trabattoni, A. Palacios, D. Ayuso, M. C. Castrovilli, J. B. Greenwood, P. Decleva, F. Martín, and M. Nisoli, J. Phys. B **49**, 142001 (2016).

[8] A. Kramida, Yu. Ralchenko, J. Reader, and NIST ASD Team (2015). *NIST Atomic Spectra Database* (ver. 5.3), [Online]. Available: http://physics.nist.gov/asd [2017, January 6]. National Institute of Standards and Technology, Gaithersburg, MD.

[9] P. Kruit and F. H. Read, J. Phys. E **16**, 313 (1983).

[10] K. Yamada, A. Iwasaki, T. Sato, K. Midorikawa, and K. Yamanouchi, Phys. Rev. A **94**, 053414 (2016).

Chapter 4

Development of Pump-Probe Experimental Setup for Observation of Ultrafast Phenomena with High-Temporal Resolution

A new experimental setup for pump-probe measurements using high-order harmonics and near-infrared (NIR) light pulses was designed and it is now under construction. With this setup, high-order harmonics will be generated as attosecond pulse trains or single attosecond pulses, and various types of phenomena, such as the laser-enabled Auger decay process in an atom and a charge migration process in a molecule, can be investigated. In order to achieve a high temporal resolution in pump-probe measurements, the beam path was made shorter than the former setup, and the chambers were designed such that the mechanical vibrations are isolated from the optics. With the current setup, high-order harmonics were generated as attosecond pulse trains, and the harmonic spectrum was observed by a flat-field type extreme ultra-violet spectrometer. Pump-probe measurements of Ar irradiated with high-order harmonics and NIR light pulses were also performed.

4.1. Introduction

Pump-probe measurements enable us to perform a real-time tracking of chemical reactions which occur on the sub-picosecond timescale [1]. In these measurements, the pump pulse triggers the chemical reaction, and the probe pulse is introduced with a certain time delay to induce another reaction such as photoionization or photoabsorption. By measuring the time-delay dependence of the signals from the process induced by the probe pulse, the chemical reaction induced by the pump pulse is tracked in real time. The pulse durations of the pump and probe pulses need to be shorter than the time scale of the target chemical reaction, therefore, high-order harmonics having attosecond pulse duration are ideal for the investigation of ultrafast processes which take place on the femtosecond to attosecond time scales.

High-order harmonics are generated either as attosecond pulse trains [2] or single attosecond

pulses [3]. When the harmonics are generated as attosecond pulse trains, several attosecond pulses having discrete energies are generated from each fundamental laser pulse. Attosecond pulse trains are useful for example when the target process has several competing processes and it is necessary to distinguish one process from the others by the energy of the emitted electrons. The laser-enabled Auger decay (LEAD) process [4,5] is one of such processes, which is described in Chapter 3. Several competing ionization processes are induced in addition to the LEAD process, and the LEAD process can be distinguished from the other processes by measuring the energies of the electrons emitted by absorbing the harmonics generated as attosecond pulse trains. Because the energies of the harmonics are discrete, the signals from the LEAD process are not energetically blurred. On the other hand, when the harmonics are generated as single attosecond pulses, the energy of the photons is continuous and only one attosecond pulse is generated from one fundamental laser pulse. Single attosecond pulses are useful for probing ultrafast processes such as the charge migration process in a molecule shown in Fig. 4-1 [6-9], which occurs on the few femtosecond or sub-femtosecond timescale. Because the attosecond pulses are temporally well separated, the ultrafast process would not be temporally blurred.

In order to perform pump-probe experiments for a long accumulation time with high temporal accuracy, it is necessary to stabilize the time delay. The time delay instabilities are induced by the mechanical vibrations and the thermal shift of the optics, and these instabilities need to be suppressed both actively and passively. In the active stabilization method [10-15], the delay shift is derived from the interference pattern of the two beams introduced in the pump and probe lines, and the path length

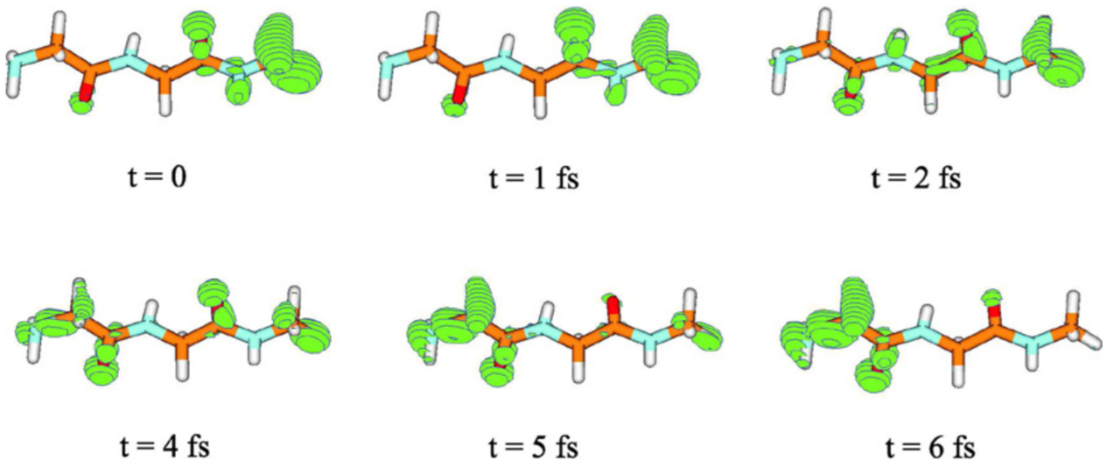

Figure 4-1 Simulated charge migration process within Gly-Gly-NH-CH_3. The hole density is indicated as green spheres. The hole position migrates from one side to the other side of the molecule in ~6 fs. The figure is adopted from ref. [6].

of the delay line is automatically adjusted such that the time delay is stabilized. In the passive delay stabilization method [13,14,16], the turbo-molecular pumps connected to the vacuum chamber is separated from the optical table so that the mechanical vibrations are not introduced to the optics from the pumps and/or the temperature of the board on the optical table is stabilized by cooling the board.

In the present work, a setup for pump-probe experiments using high-order harmonics and near-infrared light pulses is designed, and we are currently constructing the setup. The high-order harmonics can be generated either as attosecond pulse trains or single attosecond pulses, and we can choose the appropriate attosecond pulses for targeted processes. Before we install the active stabilization system, we designed and constructed vacuum chambers whose vibration from the turbo-molecular pump is isolated from the bread board inside the chamber. The current performance of the setup was checked by observing the harmonic spectrum generated as attosecond pulse trains using a flat-field type extreme ultra-violet spectrometer and by observing photoelectron spectra of Ar using a magnetic-bottle type photoelectron spectrometer.

4.2. Experimental setup

Figure 4-2 shows the schematic of the setup. All part of the setup is in vacuum, and all of the chambers are on aluminum frames, which are placed like bridges over the optical tables supported by pillars standing on the floor beside the tables. In this way, the mechanical vibrations of the chambers induced by the turbo-molecular pumps connected to the chambers do not directly penetrate to the optical tables and the optics inside the chambers, therefore the vibration of the optics is significantly suppressed. The near-infrared (NIR) light pulses from a femtosecond Ti:sapphire laser system are separated into two by a beam splitter in the first square chamber. The penetrated beam is used for the harmonic generation, and the generated harmonics are focused by a toroidal mirror. The reflected NIR pulses are focused by a concave mirror, and they are combined with the harmonics by a holed mirror in the second square chamber. Currently, a magnetic-bottle type photoelectron spectrometer is connected next to the second square chamber, and a flat-field type extreme ultra-violet (EUV) spectrometer is connected at the end of the setup. Different from the former setup in Chapters 2 and 3, photoelectron coincidence measurements are performed by the photoelectron spectrometer and at the same time, the harmonic spectra are observed by the EUV spectrometer. It is also possible to perform transient absorption measurements with the EUV spectrometer, and other experiments such as ion-photoelectron coincidence measurements can be performed by changing the spectrometer. The details

of the setup are provided in the followings.

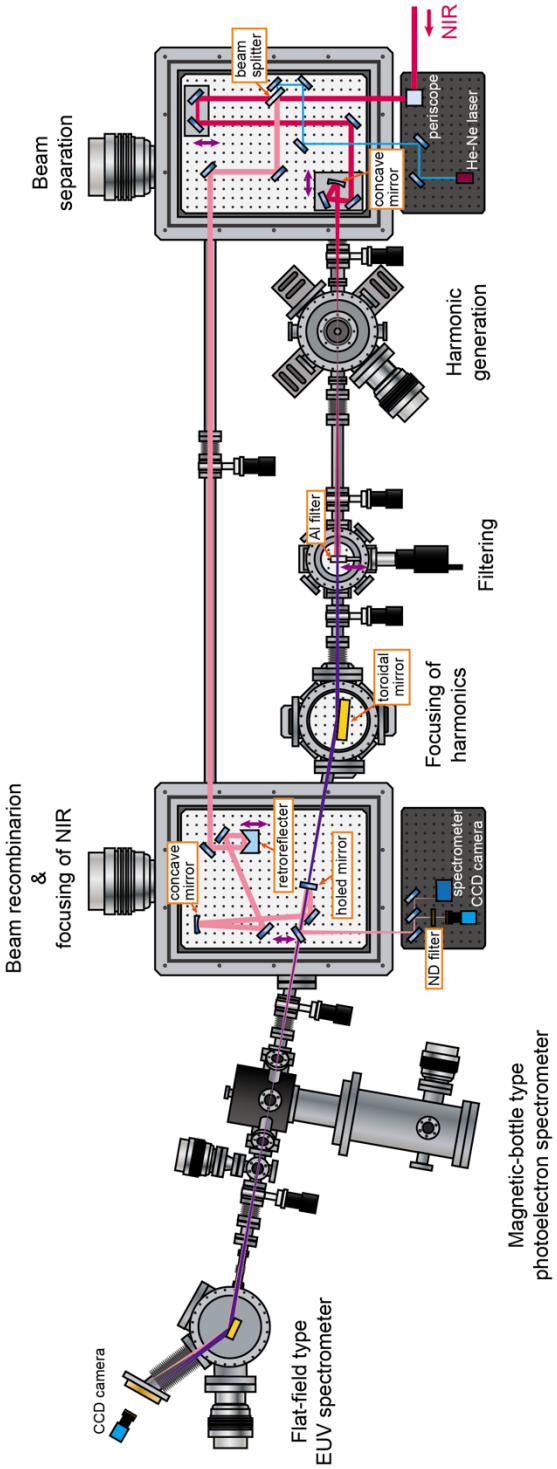

Figure 4-2 Schematic of the setup for pump-probe experiments. The near-infrared light pulses are split into two in the first square chamber. One beam is used for the generation of high-order harmonics and the other beam is combined with the harmonics in the second square chamber. Pump-probe experiments are performed with a magnetic-bottle type photoelectron spectrometer, and the harmonic spectra are observed with a flat-field type extreme ultra-violet spectrometer. See the text for detail.

4.2.1. Ti:sapphire Laser System

Ti:sapphire oscillator (RAINBOW, Femtolasers) is pumped by a Nd:YVO_4 cw 532 nm laser (Verdi, Coherent) and it generates 78 MHz, ~150 mW pulses. The pulses are led into an Offner type grating stretcher [17], and the pulse duration becomes ~100 ps. The spectral intensity and the phase of the stretched pulses are modified by an ultrafast pulse shaper (Dazzler, FASTLITE), and the pulse intensity is amplified by a regenerative amplifier and a 2-pass amplifier, which are amplified by a pump 532 nm laser (5 kHz, 30 W, ETNA, Thales laser). The pulses are finally compressed by a Treacy type grating compressor [18], and the output pulses (~800 nm, 5 kHz, 30 fs) are led into the pump-probe setup.

4.2.2. Passive Delay Stabilization

As shown in Fig. 4-3, the breadboard inside the square chamber is held by four poles standing on the optical table, and the breadboard is strengthened by a sharp-sign-shaped reinforced frame. The poles are covered with highly flexible welding bellows, which are connected to the vacuum chamber. The chamber is held by a bridge-like frame held by pillars standing beside the table in order not to touch the optical table. The turbo-molecular pump is connected to the vacuum chamber with a vibration absorption damper (VIC International) and held on the frame using vibration isolation rubbers (Fig. 4-4). In this way, the vibration of the turbo-molecular pump which penetrate to the optical table and the breadboard inside the chamber is significantly suppressed.

4.2.3. Beam Separation

The laser pulses guided from the femtosecond Ti:sapphire laser system (1.69 W) is introduced into the first square chamber by a periscope through a Brewster window (Fig. 4-5). Between the mirrors of the periscope, a beam splitter with 0.7 % reflectivity is set, and the reflected beam is led to a monitor of a beam pointing stabilization system (Aligna, TEM Messtechnik) passing through neutral density filters. The monitored shift of the beam pointing is automatically compensated by two mirrors put before the periscope, and in this way, the direction of the beam introduced to the chamber becomes always the same.

Figure 4-6 shows the inside of the first square chamber. The beam enters from one of the ports, and it hits a beam splitter with a 5 % reflectivity. The light pulses which penetrated through the beam splitter are reflected by two Ag coated flat mirrors on a manually moved delay stage (TSDS-601C,

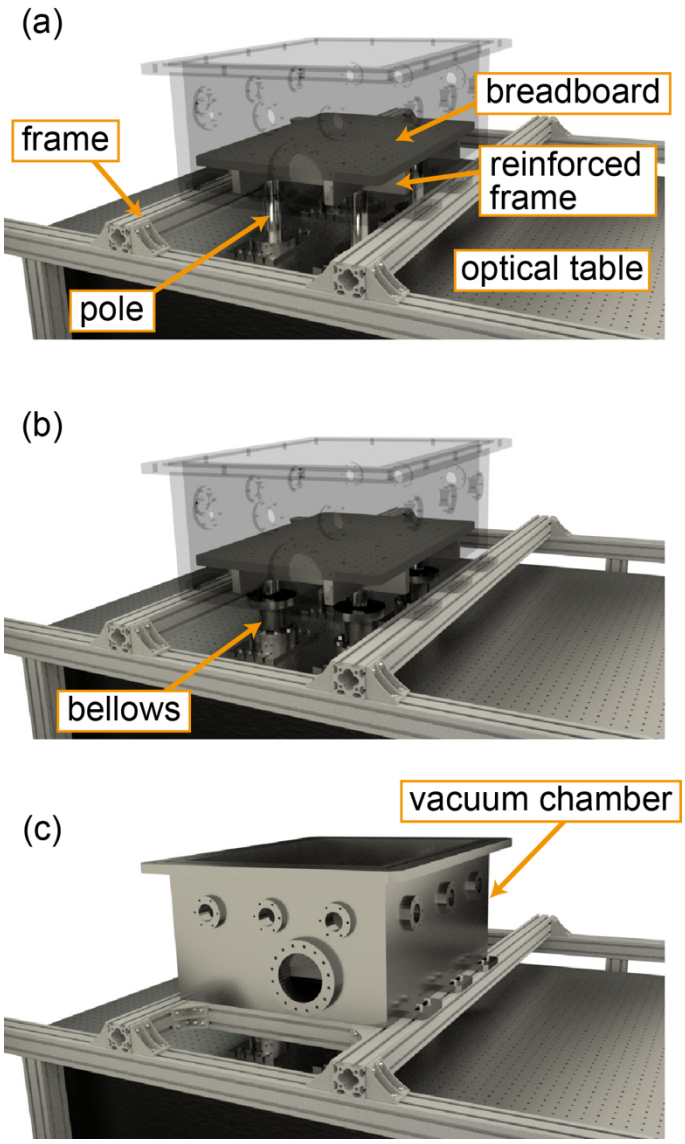

Figure 4-3 Design of the square chamber for passive delay stabilization. (a) The breadboard inside the chamber is on the reinforced frame held by the four poles standing on the optical table, (b) the poles are covered with bellows, and (c) the bellows are connected to the vacuum chamber held by a frame.

Sigmakoki), and led to a concave mirror (f = 450 mm) with three Ag coated flat mirrors. The concave mirror focuses the beam into a gas cell in the next chamber in order to generate high-order harmonics. The mirror mount of the concave mirror is motorized by piezo linear actuators (Picomotor, Newport) and it is fixed on a motorized x-axis stage for the adjustment of the position of the concave mirror after drawing a vacuum on the chamber. In this way, the focal position of the beam is finely adjusted in order to achieve the best high-order harmonic generation condition.

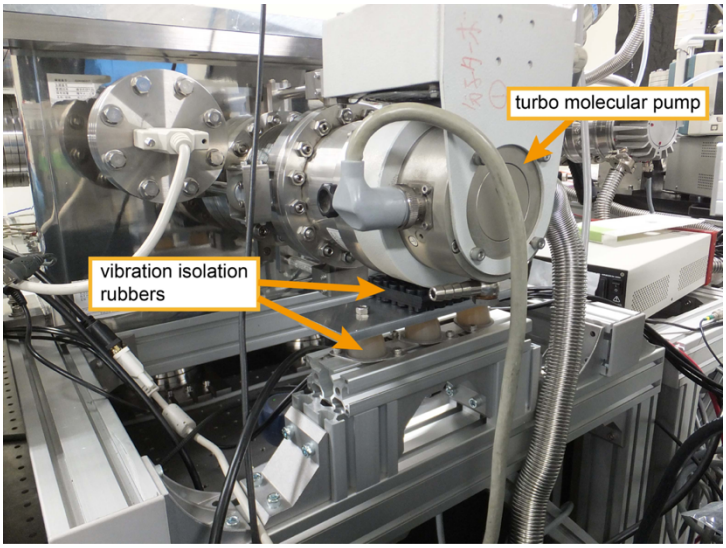

Figure 4-4 Picture around the turbo-molecular pump connected to the square vacuum chamber with a vibration absorption damper. Vibration isolation rubbers are inserted between the pump and the frame.

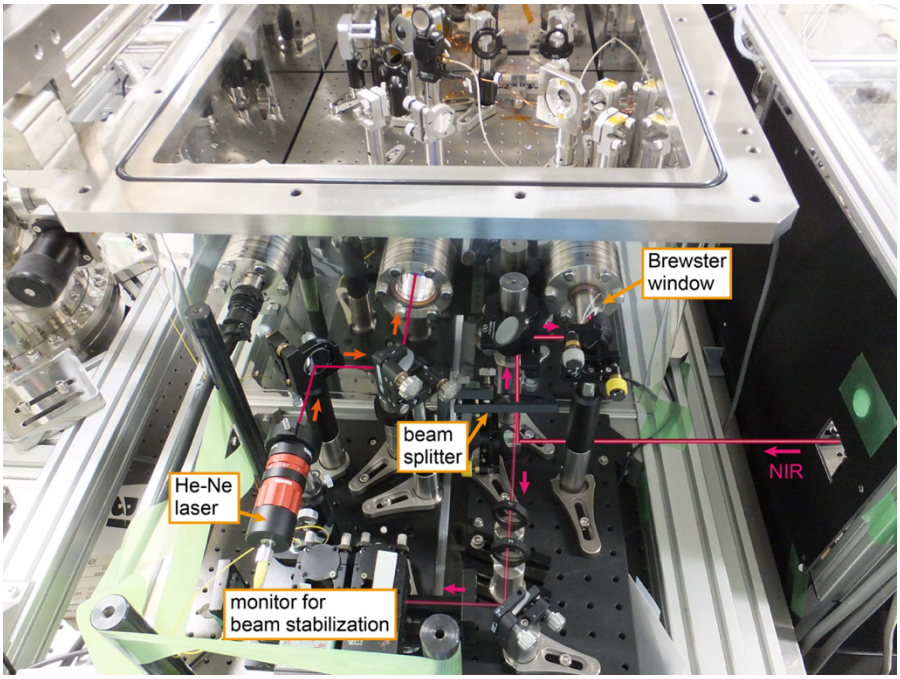

Figure 4-5 Picture around the entrance of the near-infrared light pulses into the first square vacuum chamber. The light pulses are introduced to the chamber by a periscope through a Brewster window. 0.7 % of the pulses are led to the monitor for the beam stabilization after passing through neutral density filters. He-Ne laser light for the alignment of the optics is also introduced to the chamber.

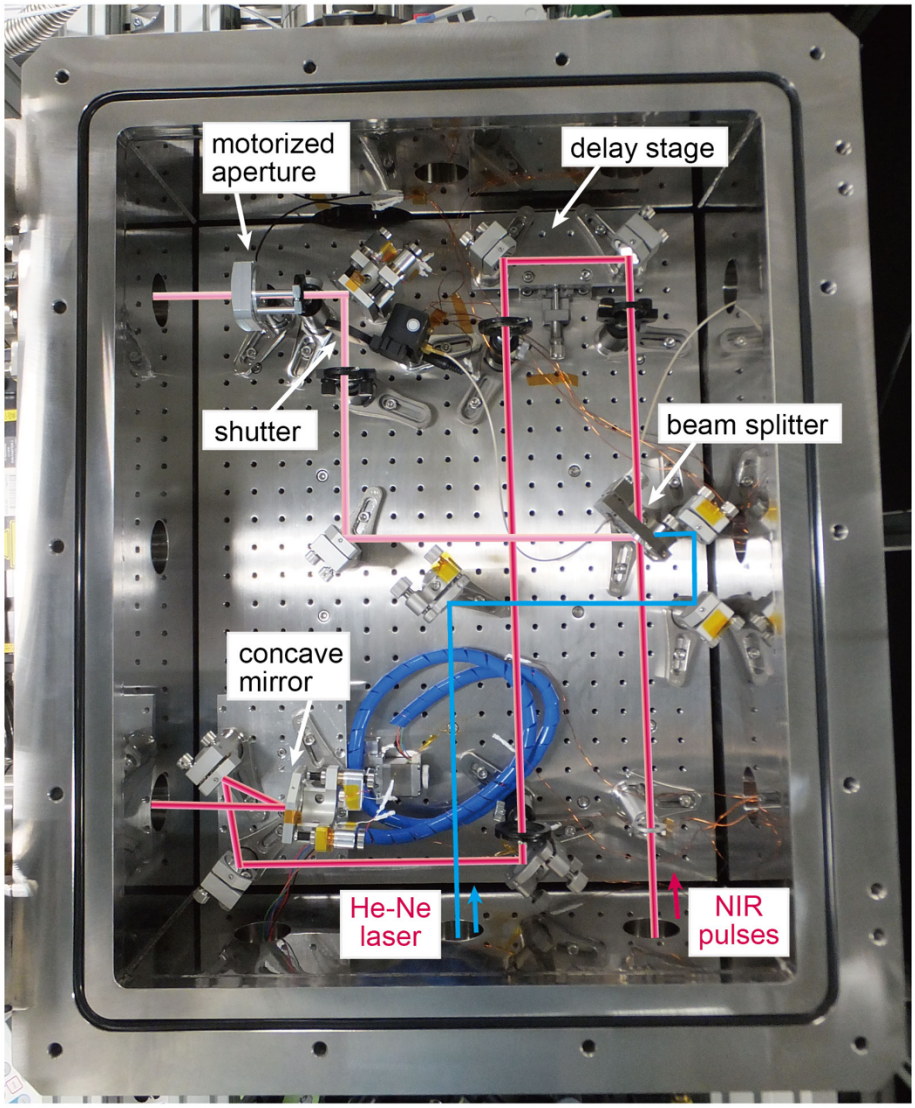

Figure 4-6 Inside of the first square chamber. NIR pulses are split by a beam splitter, and the penetrated beam is focused by a concave mirror into the harmonic-generation chamber. The reflected beam is directly led to the second square chamber. See the text for detail.

The other beam reflected by the beam splitter is led to the chamber for the beam recombination. The intensity of the beam is adjusted by changing the opening size of the aperture which is motorized by using a vacuum compatible rotation stage (AG-PR100V6, Newport). See Fig. 4-7 for the design of the motorized aperture. A motorized flipping mount (MFF101/M, Thorlabs), to which a ground-glass plate is mounted, is used as a shutter to cut the beam for the measurements performed using only high-order harmonics.

In order to make the alignment of the optics easier, apertures are placed and a He-Ne laser is introduced from the back of the beam splitter as shown in Fig. 4-6.

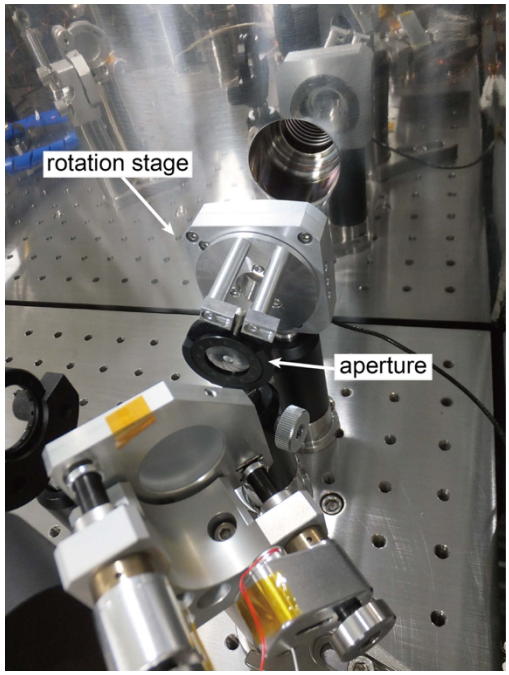

Figure 4-7 Picture of the motorized aperture. The nob of the aperture is held by sticks connected to the rotation stage. By rotating the stage, the opening size of the aperture is changed and the intensity of the NIR beam is adjusted.

4.2.4. High-Order Harmonic Generation

The beam focused by the concave mirror in the first square chamber is led to the next chamber for the high-order harmonic generation. As shown in Fig. 4-8, the chamber has a double-layered structure, which consists of an ICF 253 chamber and an inner chamber whose inner diameter is 78 mm. This inner chamber has 3 mm ϕ holes, and the focusing beam goes through the hole to enter the inner chamber. A 1/8 inch SUS tube with 500 μm holes, which is filled with a gaseous medium is placed inside the inner chamber, and the beam is focused into this gas cell. The outer ICF 253 chamber is vacuumed with a turbo-molecular pump (Turbo-V 250, Varian) connected to the side of the chamber, and the inner chamber is vacuumed with a dry pump (OnTool Booster 150, Pfeiffer vacuum) placed on the floor, which is connected to the bottom of the chamber using ICF 203 bellows, an ICF 152 tube, and an NW 50 connector through a hole piercing through the optical table (Fig. 4-9). Between the ICF 253 chamber and the chamber in the downstream, a Cu gasket with 8 mm ϕ hole is inserted. In this way, these chambers are differentially pumped to keep the chamber evacuated even if a high pressured gaseous medium is introduced to the gas cell.

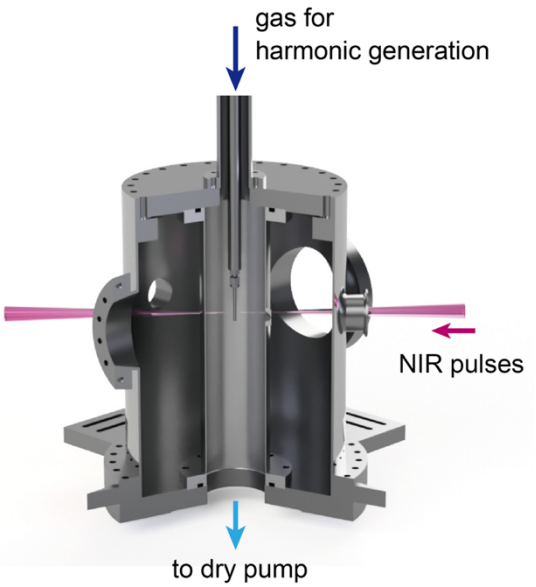

Figure 4-8 Schematic of the chamber for high-order harmonic generation. The ICF 253 chamber has a thinner chamber inside. NIR pulses are introduced to the chamber and focused into the gas cell set inside the inner chamber.

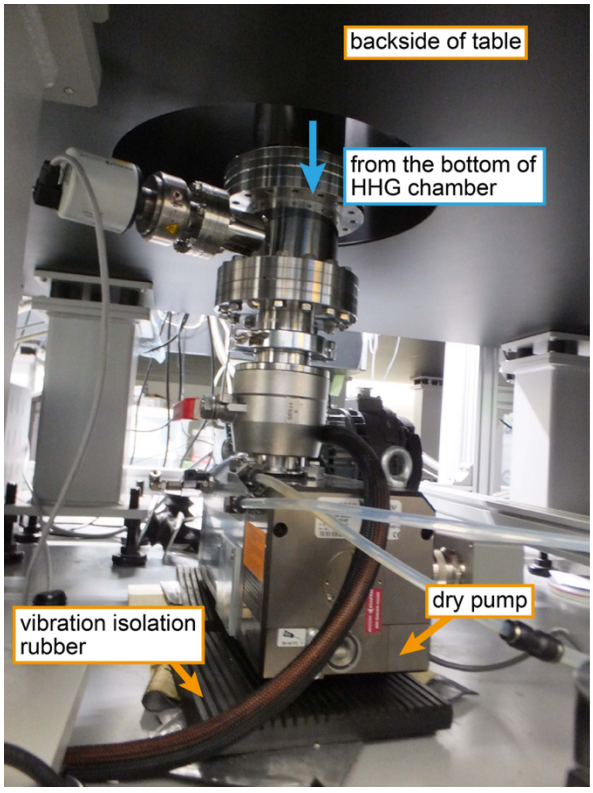

Figure 4-9 Picture of the bottom side of the harmonic generation chamber. The inner chamber is vacuumed by a dry pump. In order to prevent the penetration of the vibration of the dry pump, the pump is placed on a vibration isolation rubber.

The gas cell is connected to a tube (inner diam. 8 mm ϕ) welded to an ICF 70 flange as shown in Fig. 4-10. On the other side of the flange, a Teflon tube is connected as shown in Fig. 4-11, through which a gaseous medium is continuously introduced. The ICF 70 flange is connected to a rotation

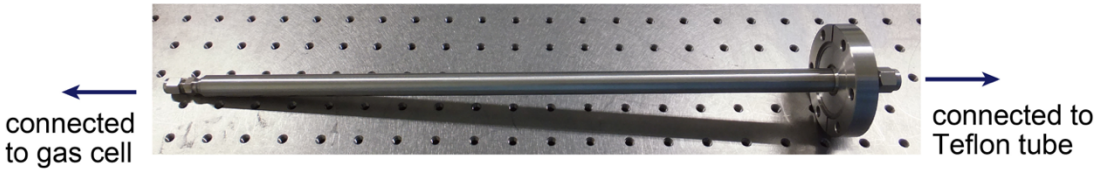

Figure 4-10 Picture of the tube used for introducing the gaseous medium to the gas cell. The tube is welded to the ICF 70 flange, which is connected to the Teflon tube. The gaseous medium is introduced through the Teflon tube, and the gas cell connected to the other side of the tube is filled with the gaseous medium.

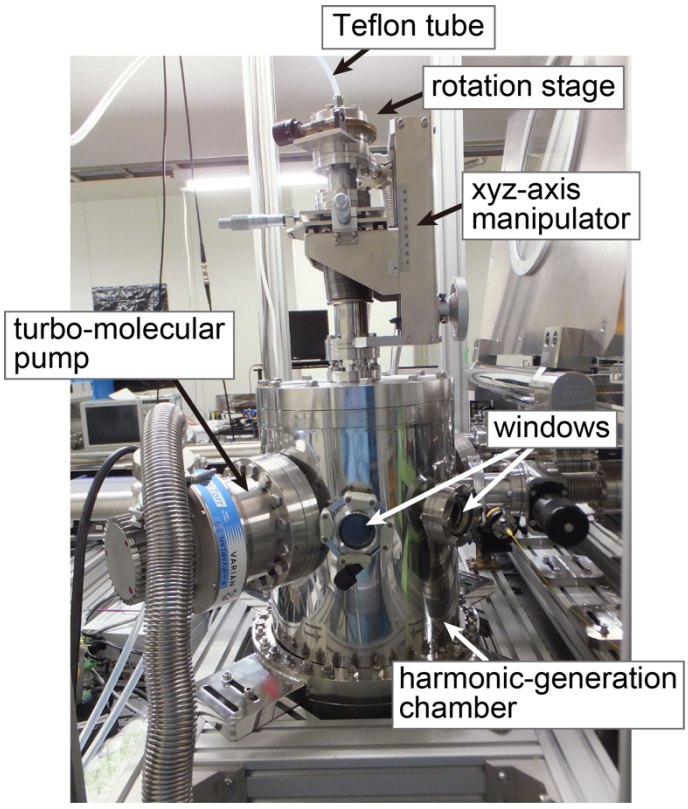

Figure 4-11 Picture of the high-order harmonic generation chamber. The gaseous medium is introduced through the Teflon tube, and the position of the gas cell inside the chamber is adjusted by using the rotation stage and the xyz-axis manipulator. The outer chamber is vacuumed by the turbo-molecular pump.

stage (VRS-070-H, Shinkukogaku) and an xyz-axis manipulator (KMV-70 ST100, Shinkukogaku). By using the rotation stage and the manipulator, the position of the gas cell is finely adjusted to achieve a better harmonic generation condition while checking the position of the gas cell from the windows on the side of the chamber indicated in Fig. 4-11 and also checking the harmonic spectrum observed by the flat-field type EUV spectrometer placed at the end of the setup (Fig. 4-2).

The generated harmonics go through an Al filter with a thickness of 200 nm, which is mounted on a holder connected to a linear motion feedthrough. By inserting the filter, the intensities of the fundamental laser pulses and the harmonics with the energy of less than 15 eV become negligibly small.

4.2.5. Focusing of Harmonics with Toroidal Mirror

The high-order harmonics are focused by a gold coated toroidal mirror with a focus length of 1217.7 mm (Shimadzu). The incidence angle is 85 degrees. The merdional radius of curvature is 14000 mm and the saggital radius of curvature is 105.95 mm so that the beam is focused as a round spot. The toroidal mirror is placed on a motorized 5-axis kinematic stage (8081M-UHV, New Focus), a manually operated rotation stage (KSPS-606M, Sigmakoki), and an xy-axis linear stage (TSDS-602S, Sigmakoki) as shown in Fig. 4-12. The position of the mirror is adjusted such that the harmonics are properly focused without astigmatism.

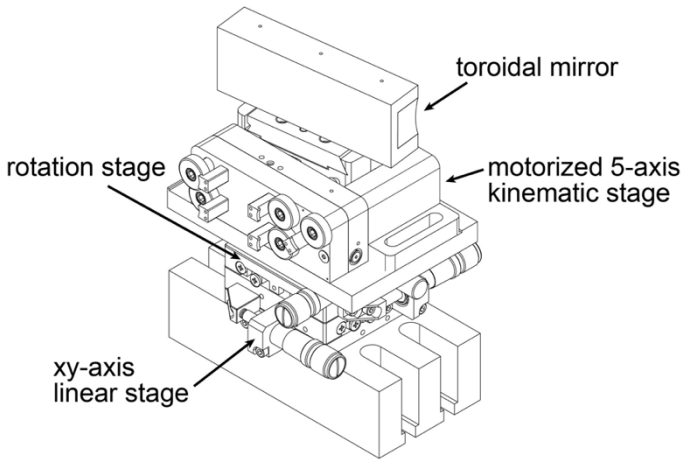

Figure 4-12 Toroidal mirror on a motorized 5-axis kinematic stage, a rotation stage, and an xy-axis linear stage. The high-order harmonics are focused by the toroidal mirror, and the focal position and the shape of the focal spot are adjusted by these stages.

The high-order harmonics are focused by a toroidal mirror instead of a back-focusing concave mirror used in Chapters 2 and 3 so that the harmonics pass through the first interaction chamber and are characterized by the spectrometer placed downstream. In the current setup, the harmonics are focused in the photoelectron spectrometer and the harmonic spectrum is monitored by the EUV spectrometer at the same time.

4.2.6. Beam Recombination and Delay Line

The inside of the second square chamber is shown in Fig. 4-13. The focusing harmonics enters the second square chamber, and they go through a hole drilled on an Ag coated flat mirror to the

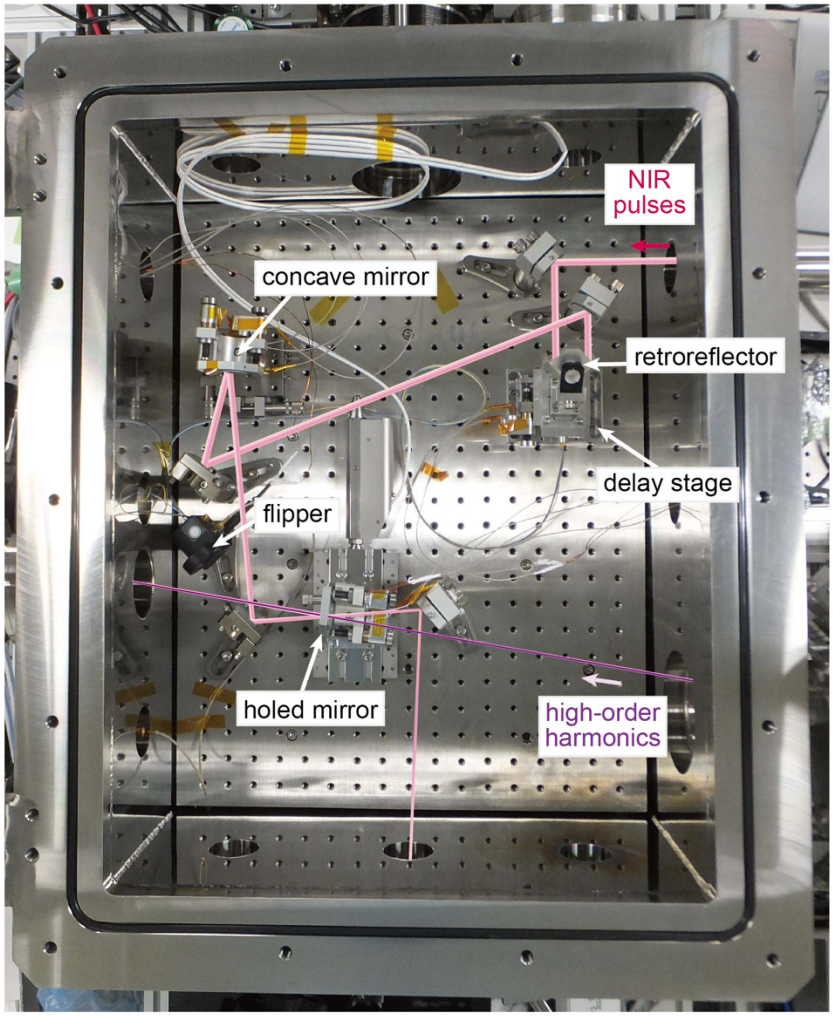

Figure 4-13 Inside of the second square chamber. The time delay of the NIR pulses are varied by moving the delay stage, and the NIR pulses are focused by the concave mirror. The NIR pulses and the focusing high-order harmonics are combined by using the holed mirror, and they are directed to the spectrometers connected downstream.

spectrometers connected next to the chamber. The holed mirror is used for the combination of the harmonics and the delayed NIR light pulses. The thickness of the holed mirror is 1 mm, and a 1.6 mm ϕ hole is drilled perpendicularly to the surface of the mirror. The mirror is mounted on a motorized mirror mount, which stands on a manually-operated z-axis stage (TSDS-403, Sigmakoki) on a motorized x-axis stage (LTAHSPPV6, Newport). By using these stages, the position of the holed mirror is adjusted such that the harmonics go through the hole properly. If the combination of the harmonics and the NIR pulses is not necessary, the holed mirror can be moved out of the optical path by the x-axis stage.

The NIR pulses also enters this chamber from the first square chamber. The NIR pulses are reflected by a retroreflector, and are led to a concave mirror (f = 900 mm). The focusing NIR pulses are combined with the harmonics by the holed mirror, and they are led to the spectrometers. In order to make the NIR pulses and the harmonics both spatially and temporally overlapped, the combined beam is led to the outside of the chamber by a mirror mounted on a motorized flipping mount (MFF101/M, Thorlabs) during the adjustment of the optics. The schematic of the setup placed outside of the chamber is shown in Fig. 4-2. A part of the beam is led to a charge coupled device (CCD) camera (DMK 21BU04 IMAGINGSOURCE) and another part of the beam is led to a miniature fiber optic spectrometer (USB2000, Ocean Optics). The positions of the concave mirror and the holed mirror are adjusted such that the NIR pulses are spatially overlapped with the harmonics by moving the motorized mirror mounts while checking the focal spots observed by the CCD camera. The temporal overlapping of the NIR pulses and the harmonics is checked by observing the spectral interference of these pulses by the miniature fiber optic spectrometer. The delay time is changed by moving the retroreflector on two motorized stages. For the coarse adjustment, the x-axis stage (TSDS-601S, Sigmakoki) is moved by a piezo linear actuator (Picomotor, Newport), and for the fine adjustment, the x-axis piezo stage (P-752, Physik Instrumente) is moved. When the pulses are temporally overlapped, the spectral interference pattern becomes less spiky, and the focal beam spot observed by the camera starts to blink.

4.2.7. Magnetic-Bottle Type Photoelectron Spectrometer

A magnetic-bottle type photoelectron spectrometer (FOM, Netherland) [19] is connected after the second square chamber. The focused beams interact with gas sample introduced into the photoelectron spectrometer through a syringe whose inner diameter is 70 μm ϕ. Magnetic fields of 1 T and 2 mT are applied on the interaction region and the drift tube, respectively, and the photoelectrons

are detected with a high collection efficiency. The photoelectron signals are recorded with a data acquisition board (TDC8HP, RoentDek GmbH). The detail of the spectrometer is described in section 2.2.3.

The calibration of the energy axis of the photoelectron spectrum was performed by using the photoelectron spectrum of Xe such that the photoelectron peaks assigned to the creation of the $5s^2 5p^5$ $^2P_{3/2}$ and $^2P_{1/2}$ levels of Xe^+ are separated by 1.3064 eV [20].

4.2.8. Flat-Field Type Extreme Ultra-Violet Spectrometer

A flat-field type EUV spectrometer is set at the end of the setup. This allows us to monitor the variation of the intensity or the wavelength of the generated harmonics while performing photoelectron spectroscopy. It is also possible to perform transient absorption spectroscopy with the EUV spectrometer.

Figure 4-14 shows the external view and the schematic of the flat-field type EUV spectrometer. The beam enters the spectrometer through a slit, which is 25 μm wide and 4 mm long. This slit improves the spectral resolution. The beam is then reflected by an Au coated flat-field toroidal grating (Jobin Yvon) and the beam is focused on an MCP detector with a phosphor screen (PHOTONIS). The image on the phosphor screen is captured by a CCD camera (Imaging Source).

The relation among the incidence angle (α), the reflection angle (β), and the wavelength of the beam (λ) is written as

$$\sin\alpha + \sin\beta = Nm\lambda, \tag{4-1}$$

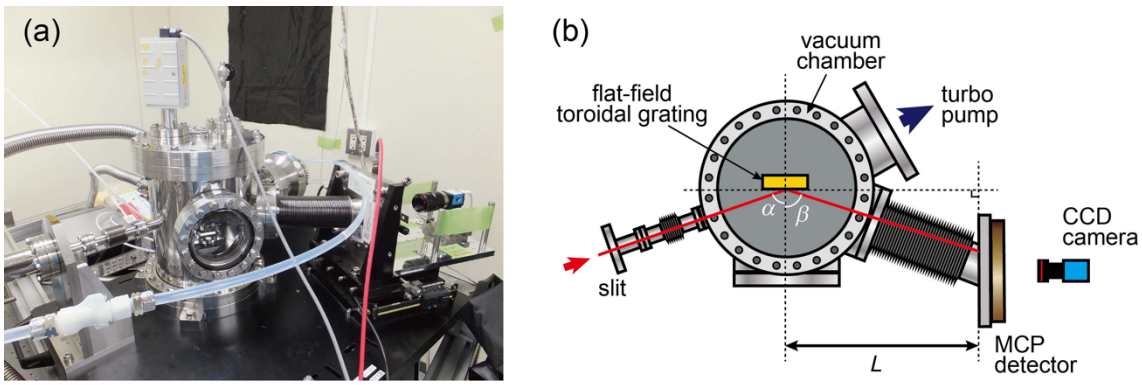

Figure 4-14 (a) Picture of the flat-field type extreme ultra-violet spectrometer and (b) the schematic of the spectrometer. The light pulses are introduced through the slit, and reflected by the flat-field toroidal grating, which shows a different reflection angle depending on the wavelength of the light pulses. The spectrum which appears on the MCP phosphor screen is captured by the CCD camera.

where N is the groove number of the grating, which is 450 gr/mm for this spectrometer, and m is the order of diffraction. The perpendicular distance between the grating and the focal point l is written as

$$l = L \times \tan(\pi/2 + \beta), \tag{4-2}$$

where L is the parallel distance between the grating and the MCP detector, which is 305.96 mm. Because β depends on λ (Eq. (4-1)), and it decides l (Eq. (4-2)), λ of each harmonic is calculated by measuring the position of the focus as follows:

$$\lambda = \frac{1}{Nm} \times \left[\sin\alpha + \sin\left(\tan^{-1}(l/L)\right) - \pi/2\right], \tag{4-3}$$

which is derived from Eqs. (4-1) and (4-2).

α and l were calibrated by using the bright light spectrum of He observed by temporarily connecting a He filled discharge tube to the spectrometer. The procedure of the calibration is as follows: Firstly, a ruler was attached to the phosphor screen as shown in Fig. 4-15(a), and the image was integrated in the blue squared region indicated in Fig. 4-15(a) in order to know the position of the tick marks on the ruler (Fig. 4-15(b)). Figure 4-16 shows the relation between the position on the phosphor screen in the unit of pixel (l_p) and the position indicated by the ruler (l_r), which is derived

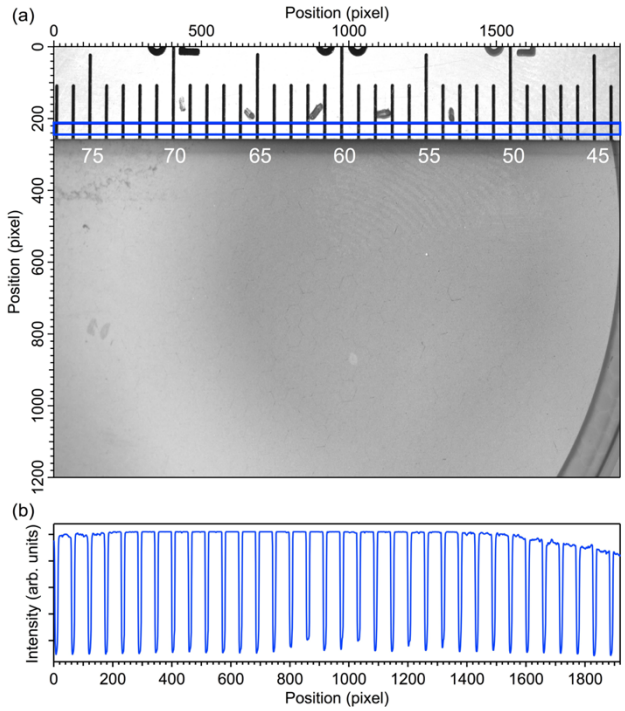

Figure 4-15 (a) Image of the phosphor screen captured by the CCD camera. A ruler is attached on the phosphor screen. The numbers in the image (a) show the positions on the ruler in the unit of mm. The image is integrated in the blue squared region, and (b) is the obtained spectrum. The peak positions correspond to the tick marks on the ruler.

from the position of the peaks in Fig. 4-15(b). From the least square fitting of Fig. 4-16, the conversion equation of the position of the image is obtained as

$$l_r(\text{mm}) = 77.104(6) - 0.017522(6) \times l_p(\text{pixel}). \tag{4-4}$$

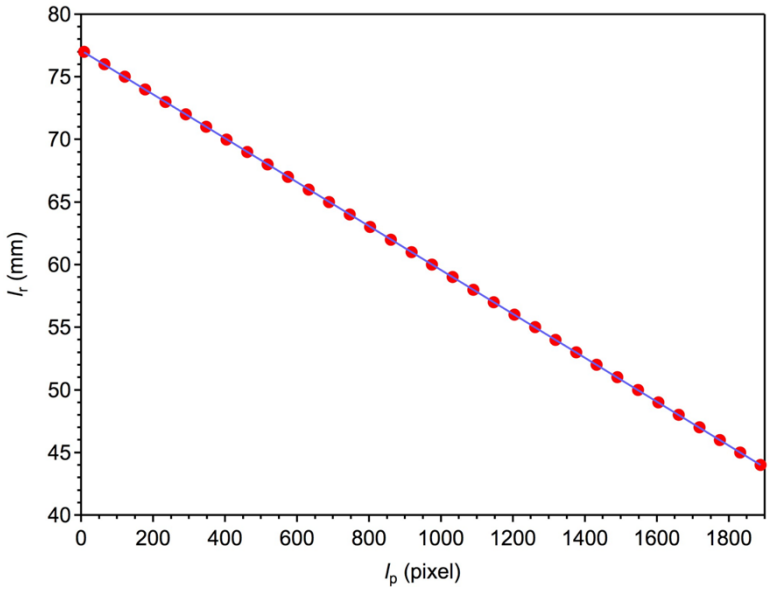

Figure 4-16 Conversion of the unit of the horizontal position from pixel to mm. The red dots correspond to the peak positions in Fig. 4-15(b). The blue line is the fitted line.

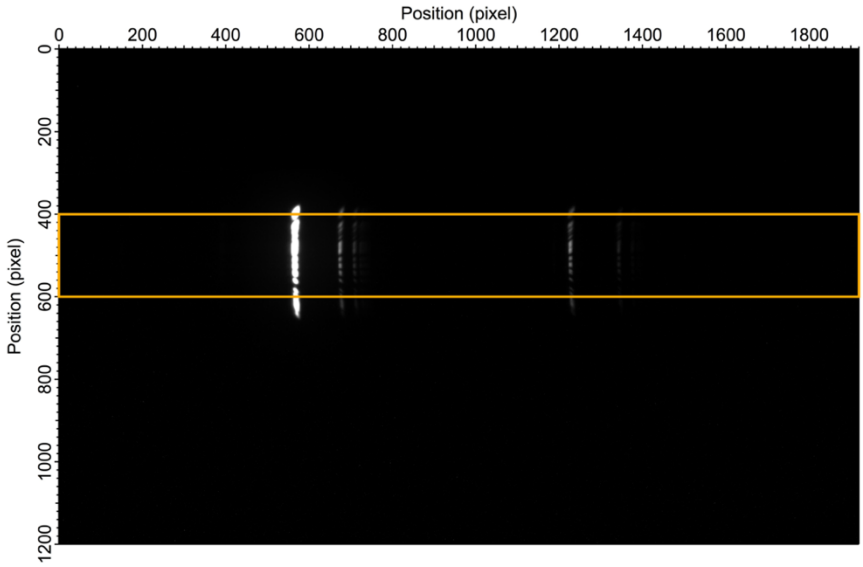

Figure 4-17 Image on the phosphor screen captured by the CCD camera. The voltages on the MCP and on the phosphor screen were 1400 V and 3400 V, respectively. Bright lines were observed when the light from the He-filled discharge tube was introduced into the flat-field type EUV spectrometer. The orange box indicates the area integrated to obtain the bright light spectrum of He.

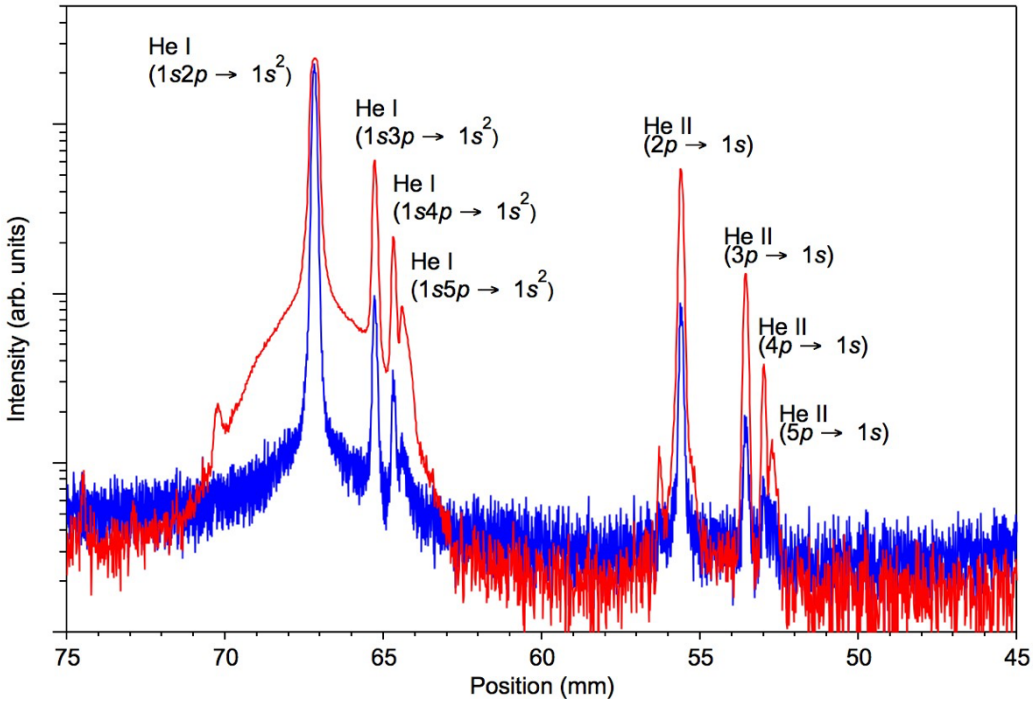

Figure 4-18 Observed bright light spectra of He. The blue line was observed when the voltages on the MCP and on the phosphor screen were 1300 V and 3400 V, respectively, and the red line was observed when they were 1400 V and 3400 V, respectively. The assignment of each peak is indicated in the figure.

Secondly, the image on the phosphor screen was obtained when the discharge of He was induced. Fig. 4-17 shows the observed image on the phosphor screen. The bright light spectrum of He was obtained by integrating the area indicated by the orange box in Fig. 4-17. Figure 4-18 shows the spectra obtained when the voltages on the MCP and on the phosphor screen were 1300 V and 3400 V, respectively (blue line), and when they were 1400 V and 3400 V, respectively (red line). As indicated in Fig. 4-18, He I and He II lines were observed.

By defining l_{offset} as

$$l_{\text{offset}} = l - l_r, \tag{4-5}$$

Eq. (4-3) is rewritten as

$$\lambda = \frac{1}{Nm} \times \left[\sin\alpha + \sin\left(\tan^{-1}\left((l_{\text{offset}} + l_r)/L \right) \right) - \pi/2 \right]. \tag{4-6}$$

By using Eq. (4-6), λ was calculated for each peak observed in Fig. 4-18, and we looked for α and l_{offset} with which the experimentally obtained value of λ matches well with the expected value of λ. From the least square fitting, we found that the experimental value of λ matches with the expected value of λ on the order of 0.1 nm when α is 69.908° and l_{offset} is 69.656 mm (Table 4-1). Because α is

not far from the original value of 70.57° and l_{offset} seems reasonable when l is roughly measured, the obtained α and l_{offset} seem to be appropriate. The spectra obtained with this spectrometer are calibrated using these α and l_{offset}.

Table 4-1 Wavelength of the bright lines of He.

Transition	λ (mm, expected)*	λ (mm, experimental)
He I ($1s2p \rightarrow 1s^2$)	58.43344	53.412
He I ($1s3p \rightarrow 1s^2$)	53.70293	53.718
He I ($1s4p \rightarrow 1s^2$)	52.22131	52.245
He I ($1s5p \rightarrow 1s^2$)	51.56168	51.565
He II ($2p \rightarrow 1s$)	30.37822	30.430
He II ($3p \rightarrow 1s$)	25.63170	25.640
He II ($4p \rightarrow 1s$)	24.30266	24.302
He II ($5p \rightarrow 1s$)	23.73308	23.700

*From ref. [20]. Weighted mean values for He II lines.

4.3. Measurements

With the current experimental setup, high-order harmonics were generated and the generated harmonic spectra were observed by the EUV spectrometer. In order to check if the harmonics and the NIR pulses are temporally and spatially overlapped, photoelectron spectra of Ar irradiated with harmonics and NIR pulses were recorded. The details are described in the following sections.

4.3.1. High-Order Harmonic Spectrum

Figure 4-19 shows the observed high-order harmonics spectra. Figure 4-19(a) was observed when the Al filter was not inserted in the beam path, and Fig. 4-19(b) shows the integrated spectrum of Fig. 4-19(a). The 13th to 29th harmonics were observed in Fig. 4-19(b), which indicates that these harmonics were focused on the photoelectron spectrometer. When the Al filter was inserted, the spectra changed as shown in Figs. 4-19(c) and 19(d), and the relative intensities of the lower-order harmonics were reduced compared to the intensities of the 23rd and 25th harmonics.

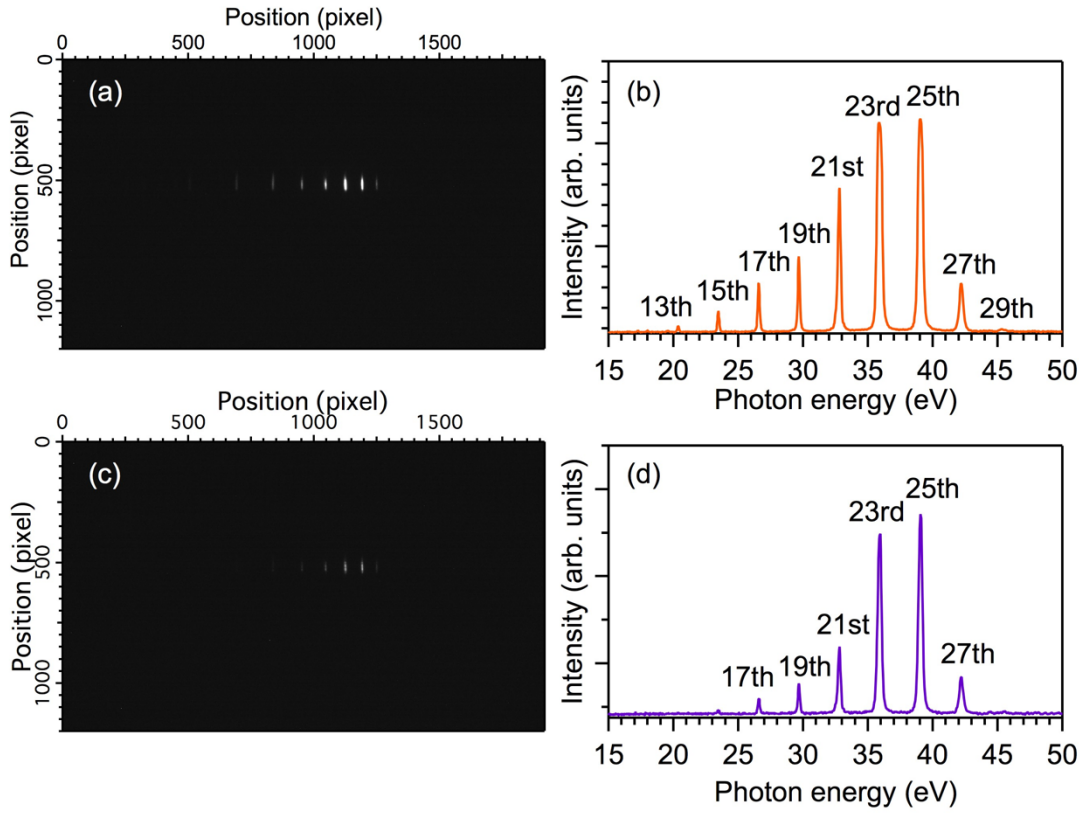

Figure 4-19 High-order harmonic spectra as the images on the phosphor screen observed (a) when the Al filter is not inserted and (c) when the Al filter is inserted. (b) and (d) were obtained by vertically integrating (a) and (c), respectively.

4.3.2. Photoelectron Spectrum

Ar gas was introduced in the interaction region of the magnetic-bottle type photoelectron spectrometer, and it was irradiated with the high-order harmonics and the delayed NIR light pulses. The energies of the emitted electrons were recorded while applying a retardation field of −8.5 V on the drift tube in order to achieve a higher energy resolution in the higher photoelectron energy range. The photoelectron spectrum observed in the photoelectron energy range of 14 to 30 eV is shown in Fig. 4-20. Photoelectron peaks assigned to the emissions of the 3*p* electrons induced by the 21st to 27th harmonics were observed. Between these peaks, side band peaks appeared at around the time delay of zero, which are assigned to the 3*p* electron emission induced by the absorptions of the *N*th harmonic (N = 21, 23, and 25) and one NIR photon and the 3*p* electron emission induced by the absorption of the (N+2)th harmonic and the emission of one NIR photon (Fig. 4-21). As shown in Fig. 4-22, the intensities of the sideband peaks reach the maximum when the time delay is zero. This means

that the high-order harmonics and the NIR pulses are spatially overlapped, and they are also temporally overlapped when the time delay is around zero.

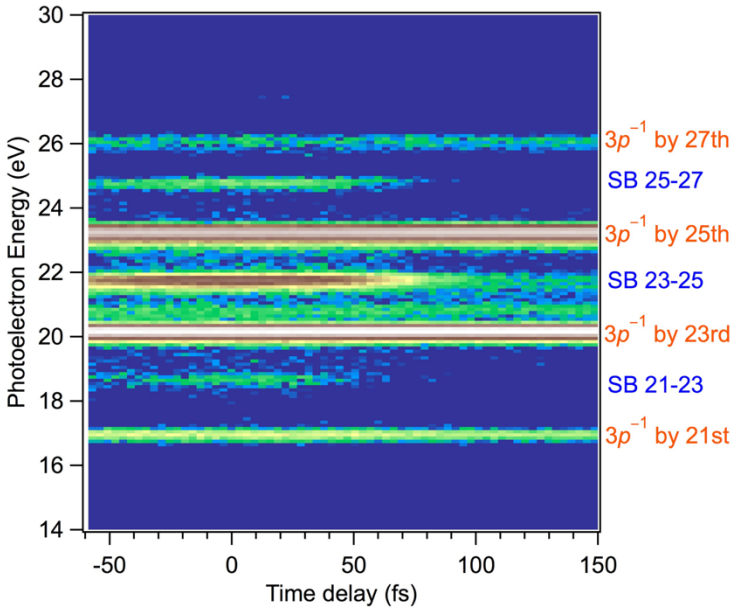

Figure 4-20 Time-delay dependence of the photoelectron spectrum of Ar irradiated with high-order harmonics and NIR pulses. 3*p* electron emissions induced by the 21st to 27th harmonics are observed. The positions of these signals induced by the *N*th harmonics are indicated with "$3p^{-1}$ by *N*th" in the figure. Between these peaks, time-delay dependent signals were observed. "SB *N*-(*N*+2)" indicates that the signal is assigned to the 3*p* electron emission induced by the absorption of *N*th harmonic and one NIR photon and the emission induced by the absorption of (*N*+2)th harmonic and the emission of one NIR photon.

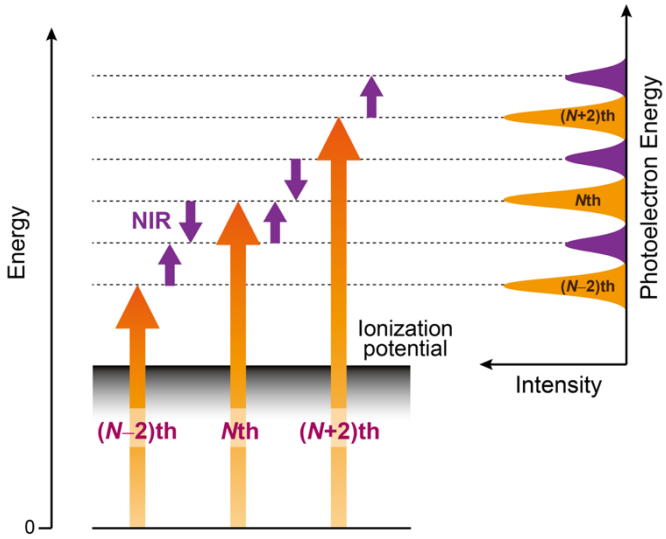

Figure 4-21 Schematic of the energy diagram when sideband peaks appear in the photoelectron spectrum. The energy of the electron emitted by the absorption of the *N*th harmonic and one NIR photon is the same as the energy of the electron emitted by the absorption of the (*N*+2)th harmonic and the emission of one NIR photon.

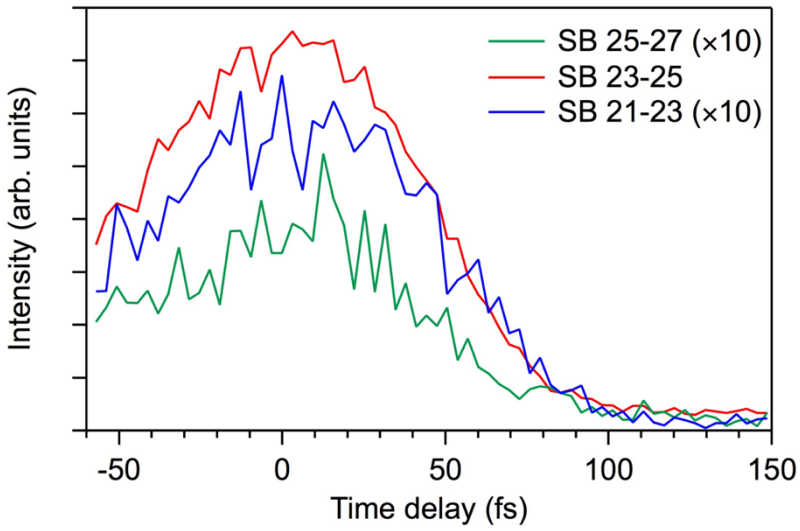

Figure 4-22 Time-delay dependence of the intensity of the sideband peaks observed in Fig. 4-20. The intensity reaches maximum when the time delay is around zero. This means that the harmonics and the NIR pulses are spatially and temporally overlapped.

4.4. Summary

The experimental setup for performing pump-probe measurements using high-order harmonics and NIR pulses were designed and constructed. With the current setup, high-order harmonics were generated as attosecond pulse trains, and the 13th to 29th harmonics were observed by the flat-field type EUV spectrometer. In the photoelectron spectrum of Ar irradiated with high-order harmonics and NIR pulses, side band peaks appeared, which suggests that the harmonics and the NIR pulses are spatially and temporally overlapped. By using this setup, the laser-enabled Auger decay (LEAD) process is expected to be observed with a shorter accumulation time compared to the setup used in Chapter 3 because the repetition rate in this setup is five times higher than in the former setup, and also the time evolution of the LEAD process can be observed with a high temporal resolution. In the near future, high-order harmonics are generated as single attosecond pulses after stabilizing the carrier envelope phase of the fundamental laser light, and the active stabilization system will be installed. After realizing these, the ultrafast electronic processes which occur on the sub-femtosecond time scale will be observed, and their effects to the following chemical reactions will be investigated.

[1] M. Dantus, M. J. Rosker, and A. H. Zewail, J. Chem. Phys. **87**, 2395 (1987).

[2] P. M. Paul, E. S. Toma, P. Breger, G. Mullot, F. Augé, P. Balcou, H. G. Muller, and P. Agostini, Science **292**, 1689 (2001).

[3] M. Hentschel, R. Kienberger, C. Spielmann, G. A. Reider, N. Milosevic, T. Brabec, P. Corkum, U. Heinzmann, M. Drescher, and F. Krausz, Nature **414**, 509 (2001).

[4] P. Ranitovic, X. M. Tong, C. W. Hogle, X. Zhou, Y. Liu, N. Toshima, M. M. Murnane, and H. C. Kapteyn, Phys. Rev. Lett. **106**, 053002 (2011).

[5] X. M. Tong, P. Ranitovic, C. W. Hogle, M. M. Murnane, H. C. Kapteyn, and N. Toshima, Phys. Rev. A **84**, 013405 (2011).

[6] A. I. Kuleff, S. Lünnemann, and L. S. Cederbaum, Chem. Phys. **414**, 100 (2013).

[7] F. Lépine, M. Y. Ivanov, and M. J. J. Vrakking, Nat. Photonics **8**, 1 (2014).

[8] F. Calegari, D. Ayuso, A. Trabattoni, L. Belshaw, S. De Camillis, S. Anumula, F. Frassetto, L. Poletto, A. Palacios, P. Decleva, J. B. Greenwood, F. Martín, and M. Nisoli, Science **346**, 336 (2014).

[9] F. Calegari, A. Trabattoni, A. Palacios, D. Ayuso, M. C. Castrovilli, J. B. Greenwood, P. Decleva, F. Martín, and M. Nisoli, J. Phys. B **49**, 142001 (2016).

[10] M. Chini, H. Mashiko, H. Wang, S. Chen, C. Yun, S. Scott, S. Gilbertson, and Z. Chang, Opt. Express **17**, 21459 (2009).

[11] G. Jotzu, T. J. Bartley, and H. B. Coldenstrodt-Ronge, Science **59**, 42 (2012).

[12] M. Fieß, M. Schultze, E. Goulielmakis, B. Dennhardt, J. Gagnon, M. Hofstetter, R. Kienberger, and F. Krausz, Rev. Sci. Instrum. **81**, 093103 (2010).

[13] R. Locher, M. Lucchini, J. Herrmann, M. Sabbar, M. Weger, A. Ludwig, L. Castiglioni, M. Greif, M. Hengsberger, L. Gallmann, and U. Keller, Rev. Sci. Instrum. **85**, 013113 (2014).

[14] S. J. Weber, B. Manschwetus, M. Billon, M. Böttcher, M. Bougeard, P. Breger, M. Géléoc, V. Gruson, A. Huetz, N. Lin, Y. J. Picard, T. Ruchon, P. Salières, and B. Carré, Rev. Sci. Instrum. **86**, 033108 (2015).

[15] M. Huppert, I. Jordan, and H. J. Wörner, Rev. Sci. Instrum. **86**, 123106 (2015).

[16] F. Frank, C. Arrell, T. Witting, and W. A. Okell, Rev. Sci. Instrum. **83**, 171101 (2012).

[17] G. Chériaux, B. Walker, L. F. DiMauro, P. Rousseau, F. Salin, and J. P. Chambaret, Opt. Lett. **21**, 414 (1996).

[18] E. B. Treacy, IEEE J. Quantum Electron. **QE-5**, 454 (1969).

[19] P. Kruit and F. H. Read, J. Phys. E **16**, 313 (1983).

[20] Kramida, A., Ralchenko, Yu., Reader, J., and NIST ASD Team (2015). *NIST Atomic Spectra Database* (ver. 5.3), [Online]. Available: http://physics.nist.gov/asd [2017, January 6]. National Institute of Standards and Technology, Gaithersburg, MD.

Chapter 5

Summary and Future Perspective

In this thesis, we irradiated rare gas atoms with ultrashort high-order harmonics generated from femtosecond laser light pulses and investigated the induced photoionization processes focusing on the behaviors of electrons by photoelectron coincidence spectroscopy. The electronic behaviors are important in various photo-induced processes, and our investigations would help us deepen the understanding of these processes.

In Chapter 2, the observation of the two-photon double ionization processes of Ar and Kr via intermediate resonance was described. It was revealed that these processes show the selective creation of doubly charged ions in the $nsnp^5\ ^1P$ state [1]. This selectivity indicated that the core electron configuration is preserved in the ionization process, and the electron pair emitted from an atom having one electron in the outermost orbital tend to form the singlet state. The preference of the singlet electron pair emission from such atoms has been theoretically reported for few-electron atoms [2-8], but none of these atoms showed selective emission of the singlet electron pair. The exclusive emission of the singlet electron pair from the excited Ar and Kr might be attributed to the electron correlations among many electrons inside the atoms, but currently, there are no theoretical explanations for the observed selectivity. Our finding is expected to stimulate the theoretical investigations of the electron correlations inside the atoms.

The observed tendency of the singlet electron pair emission can be utilized for probing the temporal evolution of the spin state. For example, Ar* ($3s3p^6np$) is firstly created in the ^1P state by the resonant excitation, but as time passes, some of them are changed to the ^3P state. When the singlet electron pair is emitted from Ar* in the ^3P state, the resultant Ar^{2+} is in the triplet state because of the conservation of the total spin angular momentum. Therefore, the spin variation process of Ar* can be followed in real time by inducing one-photon double ionization process of Ar* with various time delay and examining the spin state of the created Ar^{2+}.

I also believe that the investigation of the mechanism of the observed selective creation of only one state of Ar^{2+} and Kr^{2+} would give us important insights into the control of chemical reactions. If the mechanism of the observed selectivity is revealed by combining theoretical works, it would be possible to apply the knowledge to the more complicating systems such as molecules and to predict or control their chemical reactions.

In Chapter 3, the detection of the photoelectrons which may be emitted in the laser-enabled Auger decay (LEAD) process was described. These processes were observed when Ar was irradiated with high-order harmonics and near-infrared (NIR) light pulses [9]. It can be said that this observation is the first step towards the experimental proof of the existence of the LEAD process. In order to confirm that the observed signals are from the LEAD process, it is necessary to perform the measurements for a longer time with a high time delay stability. Because the LEAD process is very sensitive to the situation of the hole, which will be filled by another electron in the LEAD process, the LEAD process is expected to be applied as a probe of the hole migration process within a molecule. In addition, the energy of the emitted electrons varies depending on the time delay of the NIR pulses after the harmonics, that is, the energy of the emitted electrons are sensitive to the distance between the firstly emitted electron and the secondly emitted electron [10]. Therefore, the electron escaping process can be also probed by the LEAD process. The LEAD process is a very prospective process which can be applied to the probe of various processes.

In Chapter 4, a new experimental setup for pump-probe measurements and its performance were described. With the current setup, high-order harmonics are generated as attosecond pulse trains, and pump-probe measurements using the harmonics and NIR light pulses can be conducted. For example, the LEAD process can be investigated using the current setup. Because the repetition rate is five times higher than the setup used in Chapter 3 and the delay line is passively stabilized, it is expected to be easier to observe and accumulate the signals from the LEAD process with this setup than using the former setup.

The active delay stabilization system will soon be installed and the high-order harmonics will be generated as single attosecond pulses in the very near future. Then, it becomes possible to perform pump-probe measurements of sub-femtosecond processes with attosecond temporal resolution. For example, after a molecule is photoionized, the created hole is expected to migrate within the molecule on the few femtoseconds to attosecond timescales before the nuclei start to move. If we observe this ultrafast hole migration process and the chemical reactions that occur afterwards, we can investigate the effect of the ultrafast process to the following chemical reactions. This is expected to help us consider how to control the chemical reactions, and therefore it would give a major impact to a wide area of science.

[1] K. Yamada, A. Iwasaki, T. Sato, K. Midorikawa, and K. Yamanouchi, Phys. Rev. A **94**, 053414 (2016).

[2] H. W. van der Hart, K. W. Meyer, and C. H. Greene, Phys. Rev. A **57**, 3641 (1998).

[3] A. S. Kheifets, A. Ipatov, M. Arifin, and I. Bray, Phys. Rev. A **62**, 052724 (2000).

[4] J. Colgan and M. S. Pindzola, Phys. Rev. A **67**, 012711 (2003).

[5] A. Emmanouilidou, T. Schneider, and J.-M. Rost, J. Phys. B **36**, 2717 (2003).

[6] J. Colgan, D. C. Griffin, C. P. Ballance, and M. S. Pindzola, Phys. Rev. A **80**, 063414 (2009).

[7] A. S. Kheifets, D. V. Fursa, C. W. Hines, I. Bray, J. Colgan, and M. S. Pindzola, Phys. Rev. A **81**, 023418 (2010).

[8] F. L. Yip, C. W. McCurdy, and T. N. Rescigno, Phys. Rev. A **81**, 063419 (2010).

[9] K. Yamada, A. Iwasaki, T. Sato, K. Midorikawa, and K. Yamanouchi, International Conference on Ultrafast Phenomena, OSA Technical Digest (online) (Optical Society of America, 2016), paper UM2B.7.

[10] X. M. Tong, P. Ranitovic, C. W. Hogle, M. M. Murnane, H. C. Kapteyn, and N. Toshima, Phys. Rev. A **84**, 013405 (2011).

Acknowledgments

During my PhD course, I was supported by many people. First of all, I would like to express my deepest gratitude to Professor Kaoru Yamanouchi for giving me the great opportunity to conduct researches under the wonderful environment. I am also very grateful to Professor Yamanouchi for taking a lot of time for discussions and for giving me patient guidance during writing papers.

I owe my deep gratitude to Professor Katsumi Midorikawa for taking his time from his busy schedule to have a discussion with me, and also for giving me his precious advice. Especially his wealth of knowledge and experience on the high-order harmonic generation was of great help in pursuing researches.

I am deeply grateful to Dr. Atsushi Iwasaki for his generous and continuous support during my PhD course. He always gave me rational advice and helped me conducting better experiments. He also helped me and encouraged me a lot when I was writing papers and this thesis, and I really appreciate his kindness. I learned quite a lot through working with him, and it was also quite enjoyable having discussions with him whatever the topic was.

I would like to express my sincere thanks to Dr. Takahiro Sato for continuously encouraging me during my PhD course. Whenever the experiments were not going well, he always gave me useful advice and helped me a lot in the laboratory. I have a lot of respect for his uncompromising attitude towards research.

I would also like to thank all the members of Quantum Chemistry Laboratory for letting me lead a very enjoyable research life. They all have unique ideas, and I really enjoyed having discussions with them.

I appreciate the financial support from Japan Society for the Promotion of Science.

Last but not least, I would like to thank my father and my mother for their continuous supports and encouragements. I really enjoyed talking and exchanging ideas with them and also with my sister and my brother about research over dinner. I am very lucky to be a member of this family.